A NOVEL VAPOR ABSORPTION SYSTEM FOR SPACE CONDITIONING AND WATER PURIFICATION

A Dissertation
Presented to
The Academic Faculty

by

Daniel Benjamin Boman

In Partial Fulfillment
of the Requirements for the Degree
Doctor of Philosophy in the
G.W. Woodruff School of Mechanical Engineering

Georgia Institute of Technology
August 2021

A NOVEL VAPOR ABSORPTION SYSTEM FOR SPACE CONDITIONING AND WATER PURIFICATION

Approved by:

Dr. Srinivas Garimella, Chair
G.W. Woodruff School of Mechanical Engineering
Georgia Institute of Technology

Dr. Ryan P. Lively
School of Chemical and Biomolecular Engineering
Georgia Institute of Technology

Dr. Andrei G. Fedorov
G.W. Woodruff School of Mechanical Engineering
Georgia Institute of Technology

Dr. John Crittenden
School of Civil and Environmental Engineering
Georgia Institute of Technology

Dr. Seung Woo Lee
G.W. Woodruff School of Mechanical Engineering
Georgia Institute of Technology

Date Approved: May 3, 2021

In memory of my grandfather

ACKNOWLEDGEMENTS

The creation of any work of this scope, the process of which spanned the better part of a decade, is only possible through the effort and support of a large number of people. Such an endeavor requires not only technical knowledge and skill, but also persistence in the face of adversity or monotony. I cannot hope to acknowledge everyone who assisted in the creation of this thesis, but I will certainly try to address the major contributors.

I would like to begin by acknowledging my advisor, Dr. Srinivas Garimella, who has had an outsized impact on the development of this work and on my development as a person during my time in graduate school. Through both his communication with me and his actions, he has encouraged me to aspire to the highest levels of technical merit, professionalism, and courtesy. I am grateful for his advice and mentorship.

I am also thankful to the current members and alumni of the Sustainable Thermal Systems Lab who I am glad to call friends and whose technical expertise elevated the quality of this thesis, along with other work conducted during my time in graduate school. I am particularly grateful to Dr. Adrienne Little, Dr. Marcel Staedter, Dr. Darshan Pahinkar, Subhrajit Chakraborty, Mike Tambasco, Dr. Bachir El Fil, Girish Kini, Sriram Chandrasekaran, Matt Hughes, and Roland Crystal for their contributions to the thesis, both technically and in improving the quality of the writing, their advice on my career path, and their friendship.

Beyond the Sustainable Thermal Systems Lab, I would like to thank the members of my thesis committee – Drs. Andrei Fedorov, Seung Woo Lee, Ryan Lively, and John Crittenden – for their contributions to this work. I would especially like to thank Dr.

Crittenden for exposing me to the idea of EROI and for allowing me to use equipment in his lab for water quality analysis. On that note, I would like to extend my thanks to Dr. Su Liu, who worked tirelessly to ensure that the equipment was available when needed.

It is said that "all work and no play make Jack a dull boy", and if my life in graduate school has been not dull, it is largely thanks to the members of the Ballroom Dance Club at Georgia Tech, who have supported me throughout this effort and allowed me to develop my teaching, leadership, and mentorship skills through my participation in the club. I would particularly like to thank Kelsey Johnson, Walker Powell, Lana Hanlon, Chase Warner, and Erin Wrobel for their support and encouragement.

Throughout this work, I have been encouraged by the unconditional love and support of my family: my parents, who gave me valuable advice on graduate school, research, and professionalism; my brother, whose snarky quips helped keep me optimistic; my grandmother, whose constant prayers have been a source of encouragement; and my grandfather, who was always excited to hear what new area of research I was working on, even if it was something he did not fully understand.

Finally, I must acknowledge the unwavering love and support of my fiancée, Tiffany, who has been more helpful with the technical details than anyone with no background in mechanical engineering has any right to be, and whose insistence on the use of good graphic design principles is one of the main reasons the figures in this thesis are comprehensible. If any of the figures look bad, it is probably because I failed to take her advice.

TABLE OF CONTENTS

LIST OF TABLES

LIST OF FIGURES

LIST OF SYMBOLS AND ABBREVIATIONS

A	area (m^2)
a	fitting constant
b	fitting constant
C	concentration (mol m^{-3})
c_p	constant pressure specific heat capacity (J kg^{-1} K^{-1})
COP	coefficient of performance
D	diffusivity (m^2 s^{-1})
d	diameter (m)
DI	deionized
DWP	daily water production (kg day^{-1})
f	frequency (Hz)
FO	forward osmosis
FOM	figure of merit
g	gravitational acceleration (m s^{-2})
Gr	Grashof number
H	Henry's law constant (mol m^{-3} Pa^{-1})
h	enthalpy (J kg^{-1}), height (m)
HDH	humidification-dehumidifcation
HTF	heat transfer fluid
IC	inorganic carbon (mg L^{-1})
IL	ionic liquid

K	turbine meter K-factor (gal^{-1})
k	thermal conductivity ($W\ m^{-1}\ K^{-1}$)
L	length (m)
MD	membrane distillation
MED	multi-effect distillation
MSF	multi-stage flash
$\dot{m}$	mass flow rate ($kg\ s^{-1}$)
N	number of data points
N_r	number of tube rows
$\dot{n}$	molar flow rate ($mol\ s^{-1}$)
OCR	overall conversion ratio
p	pressure (kPa)
PR	performance ratio
$\dot{Q}$	heat transfer rate (W)
R	ideal gas constant ($J\ mol^{-1}\ K^{-1}$)
Re	Reynolds number
RO	reverse osmosis
Ro	Roshko number
s	center-to-center tube spacing (m), sample standard deviation
Sc	Schmidt number
SCC	specific cooling capacity ($J\ kg\text{-}ads^{-1}$)
SDWP	specific daily water production ($kg\text{-}water\ day^{-1}\ kg\text{-}ads^{-1}$)
Sh	Sherwood number

SHX	solution heat exchanger
St	Strouhal number
T	temperature
TOC	total organic carbon (mg L^{-1})
U	uncertainty
u	velocity (m s^{-1})
UA	overall thermal conductance (W K^{-1})
$\dot{V}$	volumetric flow rate (m^3 s^{-1})
V	specific volume constant
$\dot{W}$	work rate (W)
w	mass fraction
WR	water recovery
x	mole fraction

Greek Symbols

α	heat transfer coefficient (W m^{-2} K^{-1})
β	mass transfer coefficient (m s^{-1})
γ	heat capacity ratio
ε	heat exchanger effectiveness
η	efficiency
ν	kinematic viscosity (m^2 s^{-1})
ρ	density (kg m^{-3})
σ	surface tension (N m^{-1}), electrical conductivity (μS cm^{-1})

ω	humidity ratio (kg-water kg-air^{-1})

Subscripts and Superscripts

abs	absorber
conc	concentrated solution
cond	condenser
crit	critical
des	desorber
dil	dilute solution
evap	evaporator
eq	equilibrium
f	falling film
gray	graywater
HDH	humidifcation-dehumidification
hum	humidifier
HTF	heat transfer fluid
i	row index, inner
in	inlet
j	header index
K	K-factor
ℓ	liquid
lv	liquid to vapor
loop	looped
max	maximum

MD	membrane distillation
min	minimum
mix	mixture
nom	nominal
o	outer
out	outlet
p	primary
r	refrigerant
rand	random
SHX	solution heat exchanger
soln	solution
St	Strouhal number
sys	systematic
θ	reference
v	vapor
vac	vacuum pump
w	water, water vapor, wall
wa	water in air
wi	water at interface

SUMMARY

As global population and worldwide quality of life continue to increase, available freshwater resources will no longer be sufficient to meet the water needs of humanity. This necessitates the exploration of novel water sources. Many of these have been explored, with a large focus on desalination systems, including multi-stage flash, multi-effect distillation, and reverse osmosis; however, one challenge inherent in the exploitation of alternative water resources is the energy cost of producing that water. By combining water purification with cooling, investigators have sought to create systems that can produce pure water with a low energy penalty. Although these systems are a step in the right direction, they suffer from low water purification rates and in the case of adsorption heat pumps, large system footprints.

In this work, a novel water-purifying absorption heat pump cycle is developed by converting a conventional absorption heat pump from a closed-loop cycle to an open-loop cycle. By adding water purification to the cycle, the total utility of the cycle can be increased by up to a factor of two compared to a cycle that only produces cooling. LiBr is selected as the absorbent for the cycle based on thermodynamic and heat transfer studies. A heat exchanger that can serve as the absorber or desorber of a cycle with a nominal cooling capacity of 300 W and a water purification capacity of 10.5 kg day^{-1} is designed using a detailed heat and mass transfer model, and batchwise experiments are conducted using this heat exchanger to demonstrate water purification and cooling using absorption heat pump cycle components. 90% removal of contaminants from synthetic graywater and 99% removal of salt from simulated seawater are demonstrated.

CHAPTER 1. INTRODUCTION

Water is both a necessity and a luxury; while only 50 L person^{-1} day^{-1} are required for basic sanitation, washing, drinking, and cooking, people in industrialized countries can use over 200 L person^{-1} day^{-1} for the same functions and over 300 L person^{-1} day^{-1} once luxuries such as landscaping, car washes, and swimming pools are included (Gleick, 1996; Maupin et al., 2014; DeOreo et al., 2016). Projections near the beginning of the century indicated that increases in global population and improvements in quality of life in developing countries would result in higher total and per-capita water use, and global data over the past century have demonstrated the same trends, as shown in Figure 1.1 (Oki and Kanae, 2006; FAO, 2016).

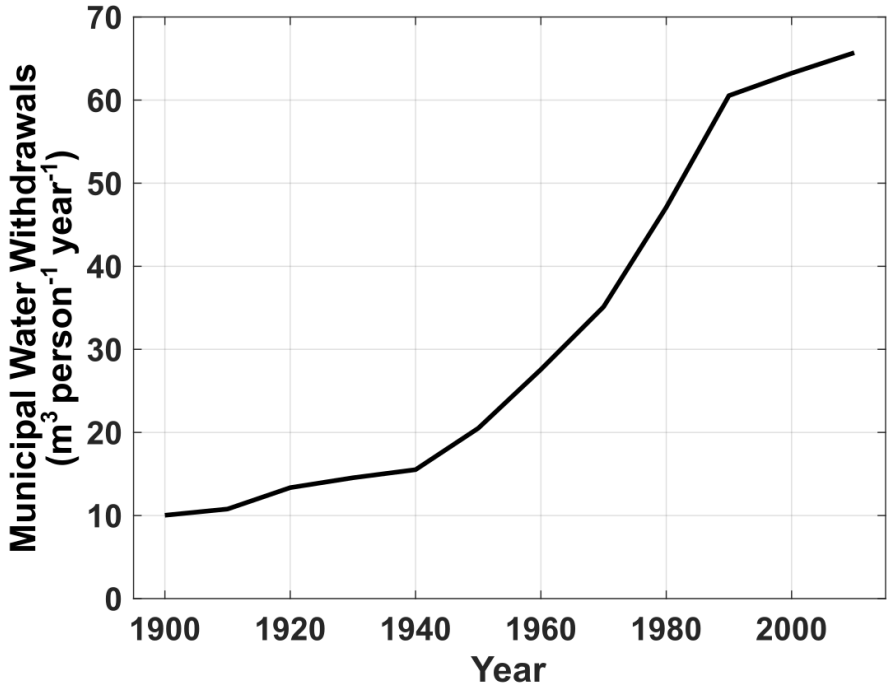

Figure 1.1: Global per-capita municipal water withdrawals since 1900. Data taken from (FAO, 2016).

With water scarcity and aquifer depletion occurring on a global scale, it is clear that conventional water sources are not enough to satisfy the increasing demand (Konikow and Kendy, 2005; Oki and Quiocho, 2020). Thus, alternative sources of water must be explored, and decentralization should be considered (Gleick, 2003). When investigating these water sources, it is important to consider the energetic cost of the water purification. In 2010, 45% of water withdrawals in the U.S. were used for electrical power generation in thermoelectric power plants, with the freshwater contribution to this accounting for 38% of the freshwater withdrawals (Maupin et al., 2014). Thus, any method of water production or purification that uses electricity may require additional water.

1.1 Alternative Water Sources

Many methods for extracting water from unconventional sources have been investigated over the past several decades. Some of these have been focused on water capture from the atmosphere, as this water requires no additional purification (Tu et al., 2018). Some investigators have explored the possibility of using nets or other apparatus to capture droplets of fog in mountainous or coastal regions (Beysens and Milimouk, 2001; Korkmaz and Kariper, 2020). Others have considered the possibility of extracting water from the ambient air, either through decreasing the temperature of the air until condensation occurs using a chiller, or through dew collection (Khalil et al., 2016), or through the use of liquid or solid desiccants from which the water is extracted by the addition of thermal energy (Su et al., 2017; Kim et al., 2018). Although innovative, atmospheric water harvesting suffers from the highly diffuse nature of the water contained in the air; even in a hot, humid climate, the humidity ratio does not exceed 0.035 kg-H_2O kg-air^{-1}.

For a more concentrated water source, water can be extracted from an impure stream, two of which are saltwater and wastewater (Grant et al., 2012; Ghaffour et al., 2013; Ghalavand et al., 2015). Although the details of some of the purification methods described below differ between saltwater and wastewater due to the composition of the source, the same overall methods can be applied.

The simplest purification method, although one of the most energetically intensive, is distillation, in which water is evaporated from an impure source and the steam is condensed. Due to the high energy cost, research in recent years has focused on solar stills, in which the distillation process is driven by a solar energy input (Sivakumar and Ganapathy Sundaram, 2013). Another approach to making distillation more sustainable is to recover the thermal energy released during the condensation. Multi-stage flash (MSF) and multi-effect distillation (MED) use this method and were the preferred methods for commercial desalination through the mid-1990s (Ghaffour et al., 2013). MSF is shown in Figure 1.2a, while MED is shown in Figure 1.2b. In MSF, the heat released during condensation is used to preheat the feedwater entering the system. This heated feedwater is then heated further by a high-temperature heat source and expands through a series of flashing chambers, each of which is at successively lower pressure. As non-condensable gases are liberated from the low-pressure feedwater, they are removed by strategically located steam-jet ejectors (El-Dessouky et al., 1999). MED is similar in that the heat rejected during condensation is recovered and used to improve the performance of the cycle. However, in MED, the condensing vapor is used to directly drive evaporation of the vapor in the next stage (Palenzuela et al., 2014). This leads to improved performance and smaller required heat transfer areas (Ghalavand et al., 2015). As with MSF, the cycle

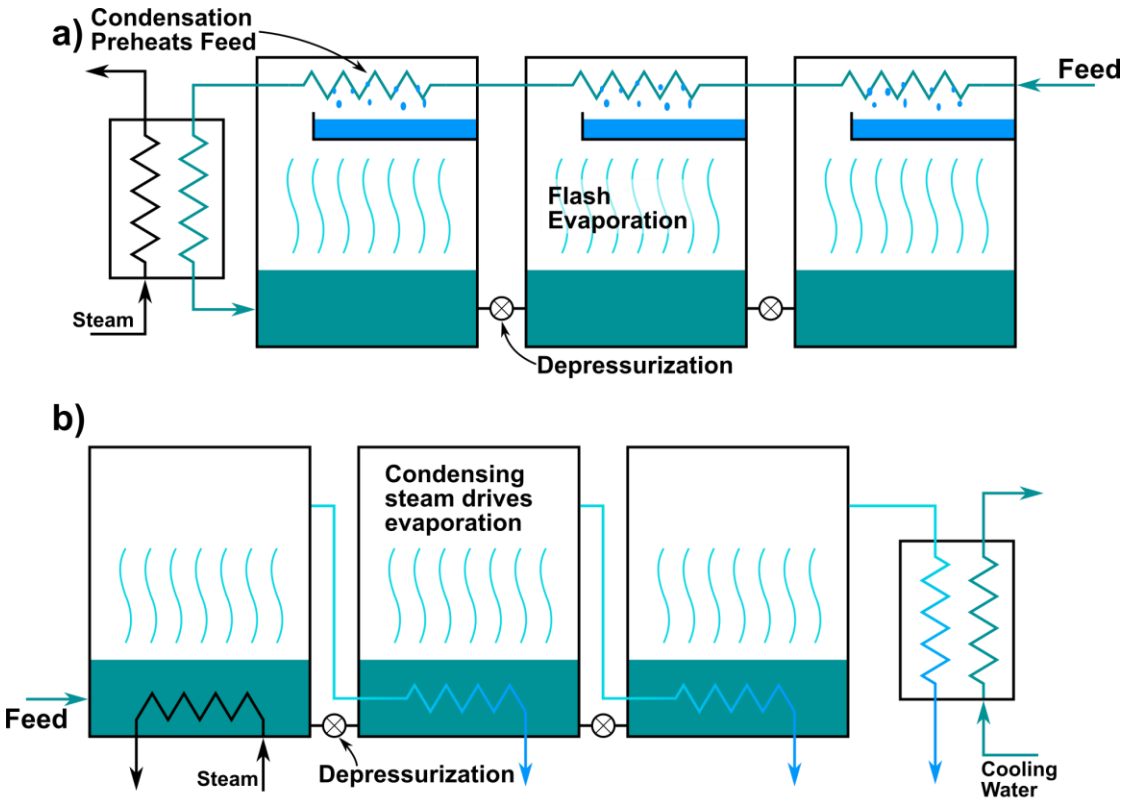

Figure 1.2: Water purification using a) MSF and b) MED

operates at subatmospheric pressure, with the top brine temperature, or the highest temperature of the feedwater in the system, limited by scaling due to precipitation of dissolved compounds in the feedwater and the last stage temperature limited by the inlet temperature of the feedwater used as the heat transfer fluid to condense the vapor generated in that stage.

The most common method of desalination today is reverse osmosis (RO), which captured the majority of the market by the turn of the 21st century due to its low energy consumption and small footprint (Ghaffour et al., 2013). Unlike MSF and MED, RO is a mechanically driven water purification process; thus, it requires high-grade electricity to operate. In RO, semipermeable membranes that are impermeable to the vast majority of dissolved solids found in the feed are used to separate the feedwater stream from the pure

permeate stream. The feedwater is pumped to high pressure, overcoming the concentration difference between the feed and permeate streams, and water flows through the membrane (Malaeb and Ayoub, 2011).

An alternative membrane-based process that seeks to address some of the challenges of RO, including membrane fouling and the resulting need for extensive pre-treatment, is forward osmosis (FO). In FO, a semipermeable membrane is used to separate the feedwater from a concentrated draw solution of known composition. The difference in concentration between the feed and draw solutions causes water to diffuse through the membrane, diluting the draw solution. Once this has occurred, the draw solution can be reconcentrated by removing the water that was extracted from the feed (Cath et al., 2006; Zhao et al., 2012). The process is shown in Figure 1.3. FO has been shown to suffer from fouling on par with that of RO, but in FO membranes, the fouling is reversible, and the responsible particulates can be removed by washing (Lee et al., 2010), which makes it a good choice for treating wastewater (Achilli et al., 2009). One of the major challenges with FO is the selection of the draw solute (Cai and Hu, 2016). Because the draw solution must be more concentrated than the feed solution, the energy requirement for removing water from the draw solution is higher than the energy requirement for removing water from the feed solution directly (McGovern and Lienhard V, 2014). Thus, in addition to monovalent

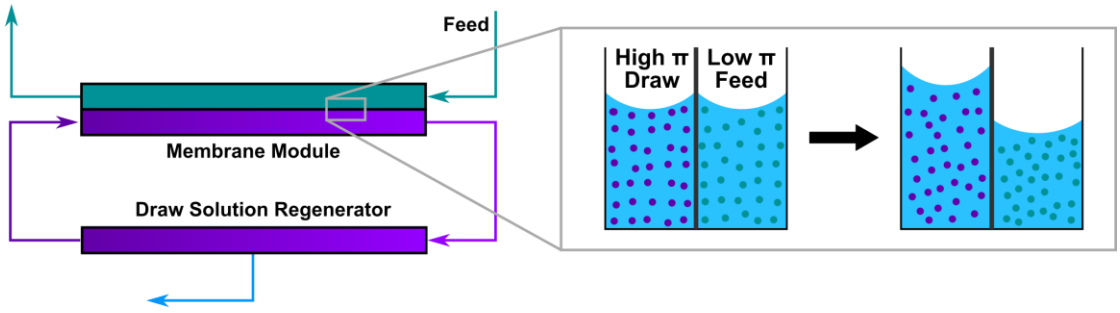

Figure 1.3: Water purification using forward osmosis

and divalent salt solutions that can be reconcentrated via RO (Achilli et al., 2010), novel draw solutes that thermally decompose (McCutcheon et al., 2005) or spontaneously separate when heated above a certain temperature (Zhong et al., 2016) have been explored.

Another membrane-based water purification method is membrane distillation (MD), which is shown in Figure 1.4. In this thermally driven method, a hydrophobic membrane is used to separate the feed from the permeate. The vapor pressure of the feed is increased above the vapor pressure of the permeate, usually by heating the feed, and water vapor flows through the pores of the membrane, where it condenses upon reaching the feed (Drioli et al., 2015). There are four major configurations in MD: direct contact, in which both the feed and the permeate are in contact with the membrane; air gap, in which condensation of the vapor occurs on a cooled plate some distance from the membrane; sweep gas, in which a carrier gas is used to transport the water vapor to a condenser; and vacuum gap, in which the permeate side of the membrane is maintained at a lower pressure through the use of a vacuum pump (Alkhudhiri et al., 2012). Each of these methods has its own advantages and disadvantages. Because there is no contact between the feed and permeate sides of the membrane, MD can be used to purify extremely concentrated feeds (Cath et al., 2005). However, there is a risk of the membrane becoming wetted by the feed

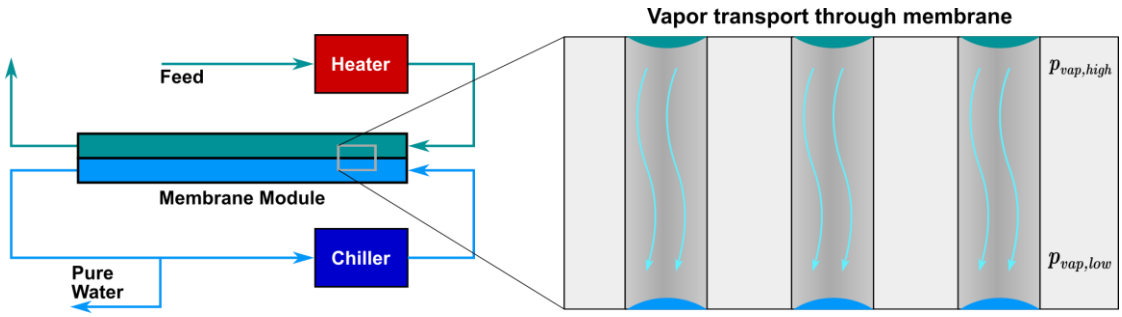

Figure 1.4: Water purification using membrane distillation

solution due to scaling or fouling with organic materials, and once this occurs, the membrane no longer effectively separates the feed and the permeate. Some investigations have been conducted to reduce these effects, but more study is needed (Rezaei et al., 2018).

A water purification method that does not require membranes or subatmospheric pressures is humidification-dehumidification (HDH). In HDH, an air stream is heated, increasing its ability to carry water, and saturated with water vapor. The warm, wet air stream is cooled, causing the water carried with it to condense (Abdelmoez et al., 2014). HDH is a simple process with relatively low energy requirements, and as such, it has received significant attention as a potential way to decentralize water production (Narayan et al., 2010). HDH systems can be classified based on the recirculation into closed-water, open-air systems or closed-air, open-water systems. Within each of these categories, heat can be transferred into the HDH process through the air or through the water.

1.2 Absorption Heat Pumps

In addition to exploring novel ways to generate potable water, investigators have considered less electrically intense ways to provide cooling. One of these that has been investigated in depth and has some commercial implementation is the absorption heat pump, which is driven primarily by thermal energy. First commercialized in the 19th century, the absorption heat pump fell out of favor with the widespread implementation of electric power during the early 20th century (Srikhirin et al., 2001). As concerns have mounted about the environmental effects of synthetic refrigerants and the high electrical consumption of vapor compression heat pumps, absorption heat pumps have received increased attention.

In any heat pump that operates with phase change, cooling is provided by evaporation of the refrigerant at a temperature below that of the conditioned space and low pressure. The resulting low-pressure, low-temperature vapor is compressed to high temperature and pressure and condensed at a temperature above that of the heat rejection space. This is shown with a mechanical compressor in Figure 1.5a. In an absorption heat pump, the mechanical compressor is replaced with a thermal compressor, which consists of two heat exchangers, a pump, and an expansion valve and is shown in Figure 1.5b. Instead of operating with a single working fluid, absorption heat pumps operate with a binary fluid called a working pair. The species that flows through the condenser and evaporator is known as the refrigerant, while the species that remains in the absorber and desorber is known as the absorbent. In all cases where working pairs are discussed in this work, the refrigerant is listed first, and the absorbent is listed second. The most common working pairs in absorption heat pumps are ammonia-water (NH_3-H_2O) and water-lithium bromide (H_2O-LiBr) (Herold et al., 1996).

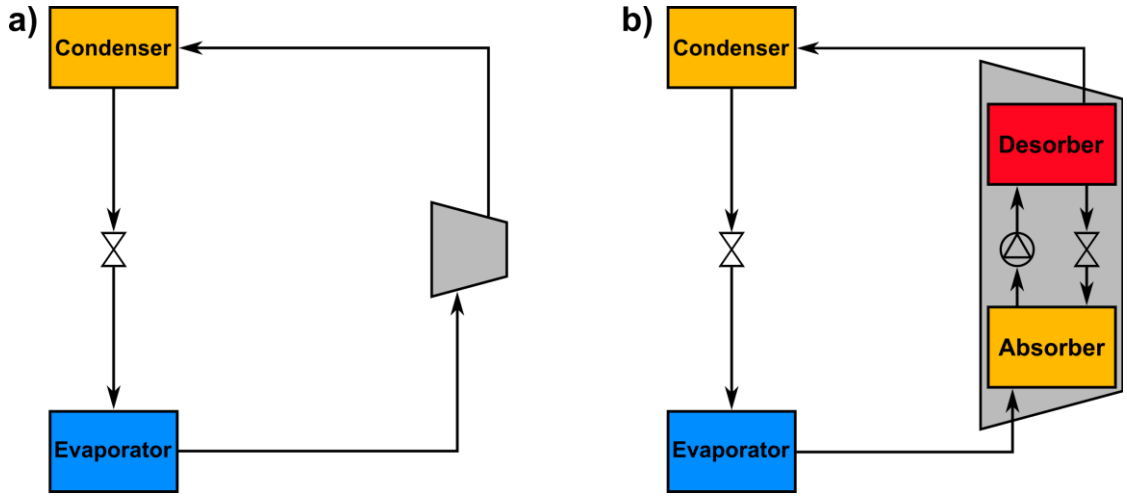

Figure 1.5: Heat pump schematics with a) mechanical compressor and b) thermal compressor

Compression of the refrigerant vapor from the outlet of the evaporator to the inlet of the condenser occurs in three steps. First, in the absorber, refrigerant vapor entering from the evaporator is absorbed into strong solution with a high concentration of absorbent entering from the desorber. Heat is rejected from the absorber during this process. Next, the resulting weak solution with a low concentration of absorbent is pumped from low pressure to high pressure, which is the only electrical power input to the thermal compressor. For systems operating with water as the refrigerant, it is typically at least two orders of magnitude less than the thermal power input due to the low specific volume of water. Finally, in the desorber, refrigerant vapor is liberated from the weak solution by heat addition. The remaining strong solution flows through the valve to the absorber to begin the compression process again.

The coefficient of performance (COP) for an absorption heat pump providing cooling is the ratio of the cooling load to the total power input to the cycle. This is the primary performance metric for an absorption heat pump.

$$COP = \frac{\dot{Q}_{evap}}{\dot{Q}_{des} + \sum_i \dot{W}_{pump,i}} \tag{1.1}$$

While technically a complete absorption heat pump, the cycle shown in Figure 1.5b is extremely inefficient because the weak solution must be heated from the absorber outlet condition to the desorption temperature by the heat input in the desorber. To improve the efficiency of the cycle, a recuperative solution heat exchanger (SHX) is incorporated in the loop containing the absorbent solution, as shown in Figure 1.6. The SHX reduces the heat input to the desorber by preheating the solution leaving the pump, which improves the COP. Additionally, it reduces the heat rejection from the absorber, which reduces the

required absorber size. In addition to the SHX, the COP can be improved by precooling the refrigerant before it enters the evaporator.

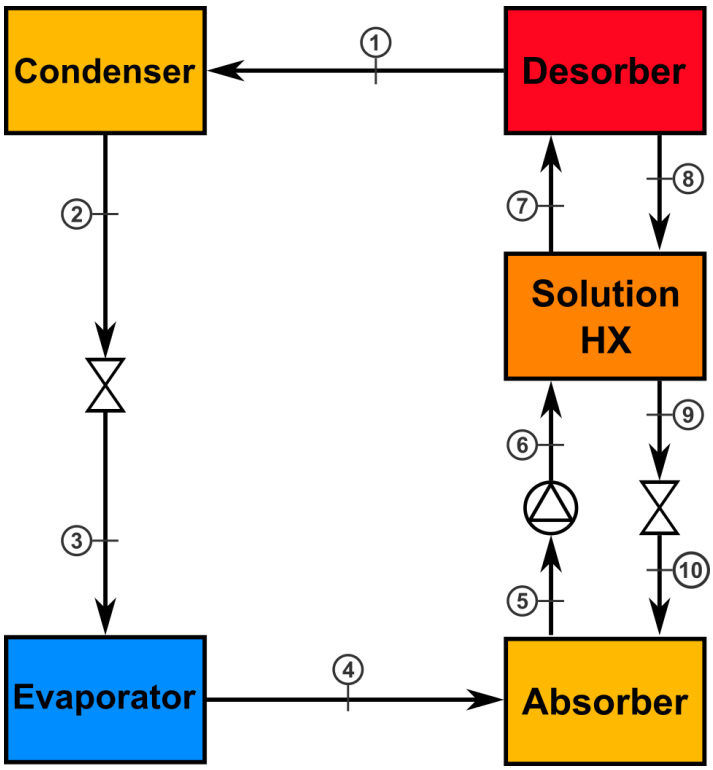

Figure 1.6: Absorption heat pump with SHX

1.3 Combined Systems

In many cases, the primary energy requirement for water purification can be reduced by combining the water purification process with another process. This is often done by using the waste heat from a power plant to drive an MSF or MED process (Wade et al., 1985; Kumar et al., 2005). Because waste heat is used, the same primary energy is used to both generate power and produce clean water. In a similar manner, investigators have demonstrated that heat pumps can be integrated with water purification systems. In some of these integrations, the heat rejected by the heat pump is used to drive a thermal water purification process (Fathalah and Aly, 1991; Gude and Nirmalakhandan, 2008;

Wang and Lior, 2011a; Nada et al., 2015a). In others, the evaporator of the heat pump operates with impure water as the working fluid, resulting in generation of pure water vapor that undergoes thermal compression to allow its collection at atmospheric pressure (Wang and Ng, 2005; Mitra et al., 2015). Although the combined systems tend to be more complex than heat pumps, the production of additional utility for nearly the same primary energy cost makes them attractive in many circumstances. An extensive review of systems that provide water purification and cooling is undertaken in Section 2.1.

1.4 Research Objectives

The primary research objective of this work is to develop and demonstrate a lab-scale proof of concept of a thermodynamic cycle based on an absorption heat pump that is simultaneously capable of space conditioning and graywater purification. To accomplish this objective, the following tasks are conducted:

- Develop a thermodynamic model of a novel, water-purifying absorption heat pump cycle.
- Simulate the performance of different absorbents to select one for demonstration.
- Construct a test stand that enables the testing of heat and mass exchangers under vacuum conditions.
- Design and fabricate heat and mass exchangers that avoid droplet entrainment and test these heat and mass exchangers under representative conditions.

- Demonstrate the water purification processes that will take place in a complete absorption cycle at conditions representative of residential space cooling.

1.5 Dissertation Outline

This dissertation is organized as follows:

- In **Chapter 2**, a cycle that allows for water purification and cooling using the components found in an absorption heat pump is conceptualized. A thermodynamic model is developed for this cycle, and its performance is determined at baseline operating conditions. Extensions to the model are considered for operating conditions where more water purification is needed than can be achieved by the default configuration and to compare the cost of the novel cycle to existing alternatives.
- In **Chapter 3**, the conditions that lead to droplet generation and entrainment are considered, and designs for the desorber and absorber of the cycle that minimize the possibility of entrainment are developed. Design models are developed to predict the performance of the desorber and absorber.
- In **Chapter 4**, a test stand for evaluation of the heat exchangers designed in Chapter 3 and the performance of the cycle developed in Chapter 2 is constructed. The water purification performance of the cycle and the thermal performance of the heat exchangers are tested at representative conditions.

- In **Chapter 5**, important conclusions from this study are summarized and future research directions are suggested.

CHAPTER 2. CYCLE DESIGN AND MODELING

Over the past few decades, numerous investigators have conducted studies on cycles or processes that combine water purification with space conditioning or that could, with minor modifications, be used for space conditioning. After detailed review of these cycles and a discussion of their advantages and disadvantages, a cycle for water purification and space conditioning is designed for multi-family housing. A thermodynamic model of this cycle is developed, and it is simulated at representative operating conditions using different working fluids. The results of this model are then used to select those working fluids that are most suitable for experimental evaluation.

2.1 Previously Studied Cycles

2.1.1 Absorption Heat Pump Cycles

The earliest cycles proposed for production of both cooling and water purification were studied in 1991 and were based on absorption heat pumps. Fathalah and Aly (1991) modeled an absorption heat pump using the H_2O-LiBr working pair with the driving heat provided by solar energy. The steam leaving the desorber of the absorption heat pump was used to drive a multi-effect distillation (MED) system with up to eight effects, and the condensate from the first three effects of the MED system was sent to the evaporator of the absorption chiller to provide cooling. They determined that the cooling coefficient of performance of the cycle could reach 0.743, and the performance ratio could reach 4.39.

Elshamarka (1991) also proposed using a solar-driven absorption heat pump with the LiBr-H_2O working pair to provide cooling, but he achieved water purification through

the use of a humidification-dehumidification (HDH) process, with the heat rejected from the absorber and condenser being used to provide warm water to the humidification column. His paper focused on the water production, treating the absorption heat pump as a known quantity, and he determined that during the summer, up to 9 L day^{-1} of water could be produced per square meter of solar collector, which doubles the water production capacity of a typical solar still.

A third configuration of a system using an absorption heat pump to provide cooling and drive water purification was studied theoretically by Gude and Nirmalakhandan (2008). As with the systems studied by Fathalah and Aly (1991) and Elshamarka (1991), the motive heat for the desalination process is provided by the heat rejected by an absorption heat pump. However, unlike the aforementioned systems, water purification was achieved through the use of a vacuum-enhanced distillation process. The authors determined that their system could satisfy cooling load of 3.25 kW and attain a water production rate of 4.5 kg h^{-1}. They assumed an absorption heat pump using the H_2O-LiBr working pair with a COP of 0.72 and determined that with that heat pump providing 3.25 kW of cooling, 4.5 kg h^{-1} of pure water could be produced, resulting in a performance ratio of 0.625.

Wang and Lior developed their own cycle at the end of the 00's that used an architecture similar to the one developed by Fathalah and Aly (1991); the steam generated by the desorber of an absorption chiller was used to drive an MED system with six effects (Wang and Lior, 2008, 2011b, a). However, in their cycle, the first effect of the MED system was used as a condenser for the absorption chiller, with this condensate being provided to the evaporator of the absorption chiller. This cycle had a COP of 0.756 and a

performance ratio of 4.016, which is comparable to the results of Fathalah and Aly (1991). In addition, they studied a modified configuration in which a second absorber was used to absorb vapor generated in the last effect of the MED system, and the heat released by that process generated additional steam to drive the MED system (Wang and Lior, 2008, 2011b). The performance of this modified cycle was not determined, but the authors noted that the modified cycle allowed a large degree of flexibility in the ratio between the cooling load and water load that was not present in the previous design. Abdulrahim and Darwish (2015) extended this work with the addition of a solar field to provide the motive heat and the inclusion of two additional effects in their MED system. For one set of operating conditions, they reported a COP of 0.744 and a performance ratio of 5.72.

A few investigators have studied cycles similar to the above, but using the NH_3-H_2O working pair in the absorption heat pump, which precludes the possibility of directly coupling the desalination process with the cooling process. Ratlamwala et al. (2013) analyzed a quadruple-effect absorption chiller in which the heat rejected from the condenser and absorber was used to drive a distillation process for seawater. For their baseline case, they reported a COP of 0.753 and a performance ratio of 0.71. It should be noted, however, that no one has experimentally demonstrated a quadruple-effect cycle. Chiranjeevi and Srinivas (2014) proposed a system that coupled an NH_3-H_2O absorption heat pump to a three-stage HDH system. The heat to drive the absorption heat pump and to heat the air for the HDH process was provided by solar collectors. At their baseline conditions, the cycle had a cooling COP of 0.375 and a performance ratio of 0.764. The authors continued their studies of this cycle with further modeling work and experimental

evaluation of the cycle (Chiranjeevi and Srinivas, 2016, 2017). They demonstrated a maximum water purification load of 60 kg day^{-1} with 150 W of cooling.

Another experimental study was reported by Ibrahim and Dincer (2015). They used an intermittent absorption heat pump coupled to a solar still to achieve cooling and water purification and demonstrated this cycle experimentally. Their absorption heat pump used the H_2O-LiBr working pair. In this case, the coupling between the water purification system and the cooling system was extremely weak, with sea water being used as the coupling fluid for the condenser, evaporator, and absorber. Because the absorption heat pump operated intermittently, the intent was to provide chilled water to a storage tank, which could then be used to provide cooling to a conditioned space throughout the day. The maximum COP demonstrated was 0.125, and the maximum performance ratio was 0.40.

A modeling study of an open-loop configuration of an absorption chiller combined with water production was conducted by Su et al. (2017). Their cycle combined an absorption chiller using the H_2O-LiBr working pair with a liquid desiccant system for air drying. While they did not explicitly address water purification in their study, it would be trivial to route the air entering the dehumidifier through a humidification column containing impure water, thus changing the cycle into an HDH-based water purification cycle. The absorbent solution leaving the liquid-desiccant dehumidifier passes into the desorber of the absorption heat pump, and some of the condensed water is removed from the system to make up for the water added in the dehumidifier. The COP of the cycle was 0.305, while the performance ratio was 0.50. In addition to the energy analysis, the authors performed an economic analysis on the cycle and determined that the payback period for such a system would be 10.2 years.

Some researchers have combined absorption heat pumps with other technologies in water purification systems to enhance the performance of the system (Janghorban Esfahani et al., 2014; Janghorban Esfahani and Yoo, 2014). In this work, a model was developed for a cycle that used a hybrid compression strategy to generate motive steam for a six-effect MED system after water was evaporated at low pressure to produce cooling. Part of the compression was accomplished by a mechanical vapor compressor, while the remainder was accomplished by a thermal compressor using the H_2O-LiBr working pair, as in an absorption heat pump. The COP of the cycle based on the total energy input was 0.684, while the performance ratio based on the total energy input was 8.94.

Mohammadi and McGowan (2018) combined a vapor compression refrigeration cycle using CO_2 as the working fluid with an MED system driven by the steam generated by the desorber in an absorption heat pump with the H_2O-LiBr working pair like the cycle studied by Wang and Lior (2011a). In this cycle, part of the evaporating water in the absorption heat pump is used as the heat sink for the vapor compression cycle. They compared the performance of the cycle with vapor compression and without vapor compression to the performance of separate cycles. When integrating the absorption heat pump with the rest of the cycle, its COP decreased; however, the integration with the additional components resulted in higher freshwater production and decreased cost for cooling and water.

2.1.2 Adsorption Heat Pump Cycles

Although research into adsorption heat pumps that provide water purification as well as cooling started later than investigations into dual-function absorption heat pumps, there has been steady progress in this area with numerous experimental demonstrations

over the past couple of decades. Reviews of this topic have been written by Ng et al. (2013), Saha et al. (2016), and Alsaman et al. (2017).

The first dual-function adsorption heat pump was demonstrated by Wang and Ng (2005). Their system used the silica gel-water working pair and had four adsorption beds. Water purification was accomplished by introducing feedwater into the evaporator and collecting the condensate. Under rating conditions of 85°C hot water, 29.4°C cooling water, and 12.2°C chilled water, a COP of 0.30 was demonstrated, although this increased to 0.40 with the implementation of heat recovery. Under the same conditions, a specific daily water production of 4.8 kg kg-adsorbent^{-1} day^{-1} was achieved. While lower than the projected numbers for the absorption heat pump cycles for water purification, it is important to note that this is an experimental demonstration, which is uncommon with the absorption systems discussed above. Another experimental study of the same adsorption desalination system was conducted by Ng et al. (2009). In this case, two adsorption beds were used, but silica gel was still used as the adsorbent. The cycle performed best at higher evaporator temperatures, although these temperatures precluded the use for air conditioning applications. Under evaporator conditions suitable for air conditioning, the experimental COP and PR were 0.51 and 0.49, respectively. A different two-bed system using silica gel as the adsorbent and solar energy for the motive heat was evaluated numerically and experimentally by Alsaman et al. (2017). They determined that their cycle had a COP of 0.46 and a specific cooling power of 112 W kg-adsorbent^{-1}.

A four-bed adsorption heat pump where adsorption and desorption were desynchronized for all four beds was used to enable continuous water production and reduce fluctuations in the chilled water temperature (Ng et al., 2012). When operated with

a desorption coupling fluid inlet temperature of 70°C and a chilled water inlet temperature of 10°C, the authors reported an overall conversion ratio of 1.0. The overall conversion ratio is a metric that combines the COP and performance ratio, and in this work, the latter metrics were not reported. Under the same conditions, the cycle achieved a specific daily water production of 2.5 kg kg-adsorbent^{-1} day^{-1}, along with a specific cooling capacity of 63 J kg-adsorbent^{-1}.

A different four-bed system using the same desynchronized schedule for the beds was studied by Mitra et al. (2014). They developed a model for a system using silica gel as the adsorbent and simulated the performance with a hot water inlet temperature of 85°C, a cooling water temperature of 30°C, and an evaporator pressure of 0.9 kPa. With a condenser temperature of 40°C and a half cycle time of 1200 s, the COP of the cycle was 0.383, the specific daily water production was 1.25 kg kg-adsorbent^{-1} day^{-1}, and the specific cooling capacity was 34 J kg-adsorbent^{-1}.

In cases where a higher temperature lift is desired, a multi-stage adsorption system, in which each bed is replaced by multiple beds in series, can be used. Mitra et al. (2014) simulated a two-stage adsorption desalination system with four beds in each stage that used silica gel as the adsorbent. The addition of the second stage allowed the condenser to operate at a pressure of 20 kPa, as opposed to a pressure of 12.5 kPa in a single-stage mode (Mitra et al., 2014). Adding the second stage made the cycle capable of operation at extreme ambient temperatures, but led to a drop in performance, with the COP of this cycle achieving a maximum of 0.228. An experimental version of the two-stage system was constructed and tested, although with two beds in each stage instead of four (Mitra et al., 2015). The authors demonstrated that backflow occurred preventing operation under

tropical conditions in a single-stage mode. When operating in two-stage mode, the cycle achieved 280 W of cooling at a COP of 0.15 and a water production rate of 11 kg day^{-1}. A similar system was developed and operated in a three-bed mode and compared to the results of the two-bed mode (Mitra et al., 2016). The COP for the three-bed mode is essentially identical to that of the two-bed mode, while the cooling duty and the water production rate increase with the number of beds in a nearly linear fashion. A two-bed, single-stage dual-function adsorption heat pump was investigated numerically and experimentally by Youssef et al. (2015a). Their simulations showed good agreement with their experiments, although the temperatures selected for evaporator and condenser coupling fluid inlet temperatures were highly optimistic. Under the more realistic operating conditions, the cycle achieved a COP of 0.35 and a performance ratio of 0.38.

Several modifications to the architecture of dual-function adsorption heat pumps have been explored. Thu et al. (2017) investigated a four-bed adsorption cycle with heat and mass recovery to improve the performance of the cycle. The performance of the cycle was simulated and compared to experimental data. With a hot water temperature of 70°C, a performance ratio of 0.63 was attained. In a different study, Thu et al. (2016) modified the cycle by incorporating two evaporators: a low-temperature evaporator for the production of air conditioning, and a high-temperature evaporator for increasing uptake in the adsorption beds and providing cooling for electronics. The performance of the cycle was simulated as a function of cooling water temperatures, hot water temperatures, and cycle times. The COP for space conditioning was as high as 0.26, while the COP for electronics cooling was as high as 0.56. In addition, the performance ratio reached 0.66 and remained near this figure for a wide range of operating conditions.

In addition to the above cycles, which used simple distillation to purify water, a cycle that coupled the adsorption cycle using the silica gel-water working pair to a MED system was studied (Shahzad et al., 2014). Unlike the absorption heat pumps coupled to MED systems, the heat source for the MED system was completely decoupled from the adsorption heat pump. However, the adsorption heat pump was used to extend the range of the MED system, with the temperature in the last effect of the system reaching as low as 2.5°C. It is unclear from the paper whether the authors intended their system to be used for cooling in addition to water purification; however, it would be straightforward to couple the MED stages that operate at sub-ambient temperatures to a conditioned space.

All the dual-function adsorption heat pumps discussed above used silica gel as the adsorbent, but other adsorbents are viable in these systems. Youssef et al. (2015b) compared the performance of AQSOA-Z02 (a zeolite) and silica gel in a four-bed, single-stage system. At the evaporator temperatures required for space conditioning, they determined that AQSOA-Z02 had better performance than silica gel, with the former achieving an overall conversion ratio of 0.77 at a desorption temperature of 85°C, while the latter only achieved an overall conversion ratio of 0.57. However, silica gel demonstrated a higher specific daily water production than AQSOA-Z02 for low desorption temperatures, suggesting that there is a tradeoff between water and cooling for these two adsorbents.

In a follow-up study, a double-effect cycle with a shared condenser-evaporator between the lower effect and higher effect was studied with AQSOA-Z02 as the adsorbent (Youssef et al., 2016). Three configurations were explored, two of which produced both water and cooling. It was found that there was no overall performance increase of the cycle

despite the added complexity, although there was a substantial increase in performance ratio in one of the modes.

Although numerous studies have been conducted into dual-function adsorption heat pumps for water purification and cooling, they continue to suffer from the problems inherent in adsorption systems. The processes are batchwise, resulting in lost energy, and high masses of adsorbent are required to satisfy even reasonable capacities for cooling and water purification. Alternative adsorbents are being explored in the adsorption heat pump literature, but these have not yet been investigated for dual-function cycles (Henninger et al., 2012; de Lange et al., 2015; Pinheiro et al., 2015; Aprea et al., 2016).

2.1.3 Mechanical Vapor Compression Cycles

Although mechanical vapor compression systems for air conditioning operate using refrigerants other than water, which precludes their configuration into open-loop systems like those studied for adsorption-based water purification, several investigators have studied the possibility of incorporating water purification schemes, chiefly HDH, with mechanical vapor compression heat pumps. The first such study was conducted by Yuan et al. (2005), in which they incorporated a vapor compression air conditioner using R22 as the working fluid with an HDH system. The condenser of the mechanical vapor compression was used to heat the air entering the humidifier of the HDH system, and the evaporator of the mechanical vapor compression system was used to condense the water vapor from the air. The water production rate was determined as a function of the feedwater flow rate and temperature, and the maximum water production rate was found to be 2.5 L h^{-1} with an evaporator temperature of 15°C. The authors did not report the power consumption of the cycle. A similar system was studied a few years later by Kalaiselvam

et al. (2010), although their system lacked the integration between the condenser and the inlet air, using an electric heater to provide the heat instead. Their system had a COP above 5 and a water production rate of nearly 3 kg h^{-1}, although it is unclear from the paper what temperature lift was achieved.

A mechanical vapor compression system that is combined with both an HDH system and a vacuum distillation system was described and modeled by Hou et al. (2008). In this system, the working fluid is an air-water mixture, with humid air at 100% relative humidity entering the compressor. The humid air is cooled by the seawater entering the vacuum distillation process, allowing distillation to proceed at a higher pressure and producing freshwater. Finally, the humid air is expanded through a turbine to provide cooling. The model indicated that electrical COPs as high as 3.5 could be obtained in hot, humid climates, and water production rates as high as 75 g kg-dry air^{-1} could be achieved with a power consumption of 20 kJ kg-dry air^{-1}.

A more recent modeling study by Nada et al. (2015b) considered a mechanical vapor compression chiller coupled to an HDH system with and without heat recovery to pre-cool the air entering the system before passing over the cooling coil. The study focused on the analysis of the water production system, treating the air conditioning system as a black box. The performance of the system was determined as a function of the air recirculation rate and environmental conditions. In addition to producing freshwater, these systems demonstrated power savings, with one system exhibiting 1000 kW of power saving for a 3500-kW refrigeration load. Following this study, a prototype system was constructed for one of the modeled configurations, and the experimental performance of the system was tested (Nada et al., 2015a). The experimental system demonstrated over 5 kW of

cooling and 6 kg h^{-1} of water production with an ambient temperature of 30°C and high relative humidity. The electrical COP for the system was around 3.5 for a wide range of operating conditions.

Further studies numerically explored the enhancement of the HDH system by incorporating solar heating to heat the water and air entering the humidifier. One of these studies incorporated an auxiliary heater to allow operation during periods of low solar insolation (Elattar et al., 2016), while the other relied solely on the solar energy (Fouda et al., 2016). In both cases, adding the HDH system with solar heating resulted in operational cost savings, along with increases in freshwater production, cooling capacity, and COP if the climate is sufficiently humid.

No studies to date have investigated the possibility of using the heat rejected from a mechanical vapor compression air conditioner to drive a thermal desalination system as has been done for absorption heat pumps. Furthermore, no economically feasible compressor has been demonstrated with sufficient capacity to use water as a refrigerant under conditions for space conditioning, precluding the use of the adsorption desalination architecture with a mechanical vapor compression heat pump (Lachner et al., 2007).

The studies reviewed above are summarized in Table 2.1. In the following sections, a dual-function absorption heat pump cycle that uses knowledge gained from these previously studied cycles is developed and modeled thermodynamically, allowing the performance of the cycle to be studied for various working pairs and operating conditions.

Table 2.1: Previous studies on cooling and water purification systems

References	Type	Technologies	Performance	Notes
Fathalah and Aly (1991)	Modeling	Absorption (H_2O-LiBr) MED	COP: 0.743 PR: 4.39	Solar energy input
Elshamarka (1991)	Modeling	Absorption (H_2O-LiBr) HDH	9 L day $^{-1}$ m^{-2} collector	Solar energy input
Gude and Nirmalakhandan (2008)	Modeling	Absorption Vacuum-enhanced distillation	COP: 0.72 PR: 0.625	Solar, electrical, and auxiliary heat input
Wang and Lior (2008, 2011b, 2011a)	Modeling	Absorption (H_2O-LiBr) MED	COP: 0.756 PR: 4.016	Alternate configuration to decouple water and thermal loads proposed
Abdulrahim and Darwish (2015)	Modeling	Absorption (H_2O-LiBr) MED	COP: 0.744 PR: 5.72	Solar energy input
Ratlamwala et al. (2013)	Modeling	Absorption (NH_3-H_2O) Distillation	COP: 0.753 PR: 0.71	Quadruple-effect system
Chiranjeevi and Srinivas (2014)	Modeling	Absorption (NH_3-H_2O) HDH	COP: 0.02 PR: 0.40	Three-stage HDH Solar energy input
Chiranjeevi and Srinivas (2016, 2017)	Experimental	Absorption (NH_3-H_2O) HDH	150 W cooling load DWP: 60 kg day^{-1}	
Ibrahim and Dincer (2015)	Experimental	Absorption (H_2O-LiBr)	COP (max): 0.125 PR (max): 0.40	Intermittent absorption heat pump
Su et al. (2017)	Modeling	Absorption (H_2O-LiBr) HDH	COP: 0.305 PR: 0.50	Liquid desiccant system Does not discuss water purification directly
Janghorban Esfahani et al. (2014); Janghorban Esfahani and Yoo (2014)	Modeling	Vapor compression & absorption (H_2O-LiBr) MED	COP: 0.684 PR: 8.94	Hybrid vapor compression strategy
Mohammadi and McGowan (2018)	Modeling	Vapor compression & absorption (H_2O-LiBr) MED	COP (VC): 4.214 COP (abs): 0.513 PR: 6.897	Combination of separate cycles

Table 2.1 continued

References	Type	Technologies	Performance	Notes
Wang and Ng (2005)	Experimental	Adsorption (H_2O + Silica gel) Distillation	COP: 0.40 (with heat recovery) SDWP: 4.8 kg kg-ads^{-1} day^{-1}	Water progresses from evaporator to condenser Four-bed system
Ng et al. (2009)	Experimental	Adsorption (H_2O + Silica gel) Distillation	COP: 0.51 PR: 0.49	Two-bed system
Alsaman et al. (2017)	Experimental	Adsorption (H_2O + Silica gel) Distillation	COP: 0.46 SCP: 112 W kg-ads^{-1} SDWP: 3.8 kg kg-ads^{-1} day^{-1}	Two-bed system Solar energy input
Ng et al. (2012)	Experimental	Adsorption (H_2O + Silica gel) Distillation	OCR: 1.0 SCC: 63 J kg-ads^{-1} SDWP: 2.5 kg kg-ads^{-1} day^{-1}	Four-bed design
Mitra et al. (2014)	Modeling	Adsorption (H_2O + Silica gel) Distillation	COP: 0.383 SDWP: 1.25 kg kg-ads^{-1} day^{-1} SCC: 34 J kg-ads^{-1}	Four-bed design
Mitra et al. (2014)	Modeling	Adsorption (H_2O + Silica gel) Distillation	COP: 0.228	Two-stage design, four beds per stage
Mitra et al. (2015)	Experimental	Adsorption (H_2O + Silica gel) Distillation	COP: 0.15 DWP: 11 kg day^{-1}	Two-stage design, two beds per stage
Mitra et al. (2016)	Experimental	Adsorption (H_2O + Silica gel) Distillation	COP: 0.15 DWP: 17 kg day^{-1}	Two-stage design, three beds per stage
Youssef et al. (2015a)	Experimental	Adsorption (H_2O + Silica gel) Distillation	COP: 0.35 PR: 0.38	Two-bed design
Thu et al. (2017)	Modeling	Adsorption (H_2O + Silica gel) Distillation	PR: 0.63	Four-bed design Heat and mass recovery
Thu et al. (2016)	Modeling	Adsorption (H_2O + Silica gel) Distillation	COP (AC): 0.26 COP (electronics): 0.56 PR: 0.66	Two evaporators Four-bed design
Shahzad et al. (2014)	Modeling	Adsorption (H_2O + Silica gel) MED	PR (average): 7.3	Cooling not reported
Youssef et al. (2015b)	Modeling	Adsorption (H_2O + AQSOA-Z02) Distillation	OCR: 0.77	Comparison to H_2O + Silica gel

Table 2.1 continued

References	Type	Technologies	Performance	Notes
Youssef et al. (2016)	Modeling	Adsorption (H_2O + AQSOA-Z02) Distillation	OCR: 0.69 COP: 0.32 PR: 0.37	Cascaded cycle
Yuan et al. (2005)	Experimental	Vapor compression (R22) HDH	COP: 3.0 DWP: 60 kg day^{-1}	Condenser heats incoming air
Kalaiselvam et al. (2010)	Experimental	Vapor compression HDH	COP > 5 DWP: 72 kg day^{-1}	Temperature lift not reported Electric heater for incoming air
Hou et al. (2008)	Modeling	Vapor compression (air-water) HDH & Vacuum distillation	COP: 3.5 SWP: 0.075 kg kg-air^{-1}	
Nada et al. (2015b)	Modeling	Vapor compression HDH	COP: 3.5	Heat recovery
Nada et al. (2015a)	Experimental	Vapor compression HDH	Cooling load: 5 kW DWP: 144 kg day^{-1} COP: 3.5	
Elattar et al. (2016); Fouda et al. (2016)	Modeling	Vapor compression HDH		Added solar heating and auxiliary heater

2.2 Cycle Design

The cycle considered in this work is a modified absorption heat pump cycle that takes cues from the research into dual-function adsorption heat pump cycles to achieve improved performance. A schematic of the cycle under study is shown in Figure 2.1. Because the cycle is based on an absorption chiller, it contains the primary heat exchangers (absorber, desorber, condenser, and evaporator), solution pump, expansion valves, and recuperative SHX common to absorption systems. However, unlike a conventional absorption chiller, an open-loop configuration is used like that studied in dual-function adsorption heat pumps, in which feedwater is introduced into the evaporator and is pumped from the condenser to atmospheric pressure (Mandani et al., 2000; Ng et al., 2013). An

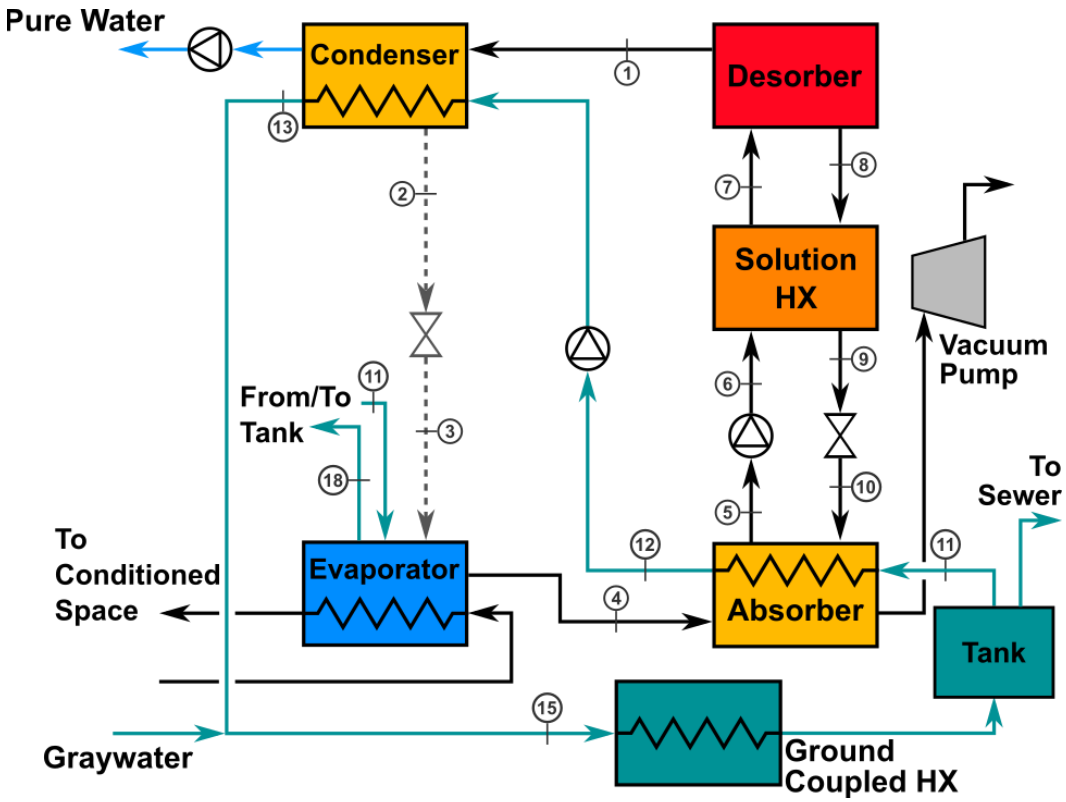

Figure 2.1: Schematic of modified absorption heat pump for water purification and cooling

expansion valve is maintained between the condenser and evaporator to allow the water load to be decoupled from the cooling load of the system. As graywater enters the evaporator, it carries dissolved gases with it, which can accumulate in the system and detrimentally affect the performance of the heat and mass exchangers. A vacuum pump connected to the absorber is used to remove these gases and avoid this drop in performance (Xie et al., 2018). In addition to being purified in the cycle, the graywater is used as the heat transfer fluid in the absorber and condenser. This allows these components to be liquid coupled, decreasing the required size. The hot graywater leaving the condenser is passed through a ground-coupled heat exchanger to maintain its inlet temperature to the absorber at an acceptable level; in an alternate configuration of the system, the ground-coupled heat exchanger could be replaced with a cooling tower.

Because feedwater enters the cycle and pure water exits the cycle, water is used as the refrigerant. Thus, the system operates at subatmospheric pressure. Numerous absorbents are compatible with water as the refrigerant; these are explored below.

2.2.1 Figures of Merit

Three figures of merit are used to assess the performance of the cycle studied in this work. The coefficient of performance (COP) is the ratio of the cooling load to the power input, both thermal and electrical, to the cycle. It should be noted that because of the high density of liquid water and aqueous solutions, the pumping power can be neglected.

$$COP = \frac{\dot{Q}_{evap}}{\dot{Q}_{des} + \sum_i \dot{W}_{pump,i}} \tag{2.1}$$

The performance ratio (PR) of the cycle is defined as the ratio of the water production rate to the steam consumption rate. Because the cycle may not be driven using steam and the enthalpy of vaporization of steam varies with temperature, a constant factor of 2257 kJ kg^{-1} is used to convert the power input to the cycle to an equivalent mass flow rate of steam.

$$PR = \frac{\dot{m}_w \times 2257 \text{ kJ kg}^{-1}}{\dot{Q}_{des} + \sum_i \dot{W}_{pump,i}} \tag{2.2}$$

Because the cycle is capable of producing multiple useful outputs for the same input, a figure of merit that accounts for both the water and cooling produced is defined. The energy ratio (ER) of the cycle is the ratio of the useful output of the cycle to the power input.

$$ER = COP + PR \tag{2.3}$$

2.3 Cycle Model

A thermodynamic model that encompasses the open-loop absorption heat pump and the graywater loop is developed to predict the performance of the system. In the development of the model, subscripted numbers refer to state points indicated in Figure 2.1. For all components in the system, heat transfer and work are both taken as positive into the component. The following assumptions are applied in the thermodynamic model:

1. The dilute solution leaving the absorber, concentrated solution leaving the desorber, refrigerant leaving the condenser, and refrigerant leaving the evaporator are in saturated states at their respective component outlet temperatures.
2. There is no pressure drop between components.

3. Pure water vapor exits the desorber at the desorber pressure and solution outlet temperature, which is a conservative estimate.
4. The fluid flowing through the condenser is pure refrigerant.
5. The expansion valves operate isenthalpically.
6. Fluid flowing through the pumps is incompressible.

The mass balance on the desorber is

$$\dot{m}_{dil} = \dot{m}_{conc} + \dot{m}_r \tag{2.4}$$

where $\dot{m}_{dil}$ is the mass flow rate of dilute solution (i.e., the solution has a high refrigerant and low absorbent concentration), $\dot{m}_{conc}$ is the mass flow rate of concentrated solution, and $\dot{m}_r$ is the mass flow rate of refrigerant. It should be noted that $\dot{m}_r$ may not be the same as $\dot{m}_w$. For low water loads and high cooling loads, some of the water generated in the desorber may be returned to the evaporator instead of being extracted in the condenser.

The species balance on the desorber is

$$\dot{m}_{dil} w_{dil} = \dot{m}_{conc} w_{conc} \tag{2.5}$$

where *w* is the mass fraction of absorbent in the solution.

Because there is a partial evaporation of graywater in the evaporator, there will be a change in concentration of the graywater, and to account for the possibility of precipitation of dissolved solids, this concentration must be known. The mass balance on the evaporator is

$$\dot{m}_{r,loop} + \dot{m}_{gray,evap,in} = \dot{m}_r + \dot{m}_{gray,evap,out} \tag{2.6}$$

where $\dot{m}_{r,loop}$ is the mass flow rate of water passing from the condenser to the evaporator, and $\dot{m}_{gray,evap,in}$ and $\dot{m}_{gray,evap,out}$ are the mass flow rates of graywater into and out of

the evaporator respectively. A species balance can be written on the evaporator for each of the species dissolved in the graywater.

$$\dot{m}_{gray,evap,in} w_{i,gray,tank} = \dot{m}_{gray,evap,out} w_{i,gray,evap,out} \tag{2.7}$$

The variable $w_{i,gray,tank}$ is the mass fraction of a particular species within the graywater tank, which depends on the recovery. The recovery of the cycle, which is the mass of pure water produced divided by the mass of the feed, relates the concentration of species in the inlet graywater to the concentration of species in the graywater tank as shown below.

$$WR = 1 - \frac{w_{gray,in}}{w_{gray,tank}} \tag{2.8}$$

Within the absorption heat pump, energy balances are conducted on each component to determine the thermal loads and assist in detailed component modeling. The energy balance on the desorber is

$$\dot{Q}_{des} = \dot{m}_{conc} h_8 + \dot{m}_r h_1 - \dot{m}_{dil} h_7 \tag{2.9}$$

The energy balance on the condenser is

$$\dot{Q}_{cond} = \dot{m}_r (h_2 - h_1) \tag{2.10}$$

This is expected to be negative because heat is rejected from the absorption heat pump in the condenser.

The energy balance on the evaporator is

$$\dot{Q}_{evap} = \dot{m}_r h_4 + \dot{m}_{gray,evap,out} h_{18} - \dot{m}_{r,loop} h_3 - \dot{m}_{gray,evap,in} h_{11} \tag{2.11}$$

The enthalpy of the graywater entering the evaporator is the same as the graywater exiting the tank at state 11.

The energy balance on the absorber is

$$\dot{Q}_{abs} = \dot{m}_{dil} h_5 - \dot{m}_{conc} h_{10} - \dot{m}_r h_4 \tag{2.12}$$

The solution heat exchanger (SHX) between the absorber and desorber improves the performance of the cycle by reducing the required heat input to the desorber by raising the inlet temperature of the dilute solution and by reducing the heat rejection from the absorber by lowering the inlet temperature of the concentrated solution. The heat transfer rate in the SHX is

$$\dot{Q}_{SHX} = \varepsilon_{SHX} \dot{Q}_{SHX,max} \tag{2.13}$$

In this model, enthalpy-based effectiveness is used.

$$\dot{Q}_{SHX,max} = \min\{\dot{m}_{dil}(h_{7,max} - h_6), \dot{m}_{conc}(h_8 - h_{9,min})\} \tag{2.14}$$

where

$$\begin{aligned} h_{7,max} &= h(T_8, w_{dil}) \\ h_{9,min} &= h(T_6, w_{conc}) \end{aligned} \tag{2.15}$$

Energy balances on each of the fluids in the SHX allow the determination of the solution state at the desorber and absorber inlets.

$$\begin{aligned} \dot{Q}_{SHX} &= \dot{m}_{dil}(h_7 - h_6) \\ \dot{Q}_{SHX} &= \dot{m}_{conc}(h_8 - h_9) \end{aligned} \tag{2.16}$$

As graywater flows into the evaporator, it carries dissolved air with it, which can substantially reduce the performance of the condenser and absorber. To prevent this, a vacuum pump is used to remove non-condensable species from the absorber during operation of the cycle. To determine the power requirement of the vacuum pump, the flow rate of gases into the system must be determined. The molar flow rate of a single species of gas into the system can be calculated through application of Henry's law for the primary

component gases in atmospheric air. The concentration of a species dissolved in water at a given temperature is given by

$$C_i = p_i H_i^{\theta} \exp\left(-\frac{\Delta H_i}{R}\left(\frac{1}{T} - \frac{1}{T^{\theta}}\right)\right) \tag{2.17}$$

where the subscript i refers to the species and H_i^{θ} and $-\frac{\Delta H_i}{R}$ are taken from the work of Sander (2015). The molar flow rate of that species into the cycle can be calculated as

$$\dot{n}_i = C_i \frac{\dot{m}_{gray,evap,in}}{\rho_{gray}} \tag{2.18}$$

With the flow rate known, the power requirement of the vacuum pump can be calculated, assuming that the air behaves as an ideal gas and that all of the water vapor is absorbed in the absorber (Xie et al., 2018).

$$\dot{W}_{vac} = \frac{\sum_i \dot{n}_i R T_{in}}{\eta_{vac}} \frac{\gamma}{\gamma - 1}\left[\left(\frac{p_{out}}{p_{in}}\right)^{\frac{\gamma-1}{\gamma}} - 1\right] \tag{2.19}$$

In the above equation, R is the ideal gas constant, T_{in} is the temperature at which air enters the vacuum pump, assumed to be the absorber outlet temperature, η_{vac} is the vacuum pump efficiency, set at 60%, p_{in} and p_{out} are the inlet and outlet pressures of the vacuum pump, and γ is the heat capacity ratio of the gas.

Energy balances on the graywater that serves as the heat transfer fluid in the absorber and condenser are used to determine the required heat transfer fluid flow rate and the outlet temperature of the graywater. The energy balance on the graywater side of the absorber is

$$-\dot{Q}_{abs} = \dot{m}_{gray,HTF}(h_{12} - h_{11}) \tag{2.20}$$

The energy balance on the graywater side of the condenser is

$$-\dot{Q}_{cond} = \dot{m}_{gray,HTF}(h_{13} - h_{12}) \tag{2.21}$$

Closest approach temperature differences (CATs), which are the minimum temperature difference between the coupling fluid and the working fluid in a heat exchanger, are specified in the condenser and absorber. Because graywater flows through them serially, either the graywater outlet temperature in the condenser or the graywater outlet temperature in the absorber is limiting. The mass flow rate of the graywater used as a heat transfer fluid is the maximum of two possible mass flow rates. The first is the mass flow rate required to remove the heat rejected by the absorber when the temperature increases from the inlet value to a temperature lower than the equilibrium absorber outlet temperature by the specified CAT. The second is the mass flow rate required to remove the heat rejected by the absorber and condenser when the temperature increases from the inlet value to a temperature lower than the condenser saturation temperature by the specified CAT. This is shown in the following equation.

$$\dot{m}_{gray,HTF} = \max\left\{-\frac{\dot{Q}_{abs}}{h_{12,max} - h_{11}}, -\frac{\left(\dot{Q}_{abs} + \dot{Q}_{cond}\right)}{h_{13,max} - h_{11}}\right\} \tag{2.22}$$

For the purposes of the model, the composition of the graywater is assumed to be identical to the synthetic graywater formulation developed by Hourlier et al. (2010). Vapor pressures are calculated using Raoult's law, and the thermophysical properties are assumed to be identical to those for pure water due to the low concentration of dissolved solids. It is assumed that the graywater stream undergoes a pre-treatment step that removes suspended particles before entering the graywater tank. Due to the presence of dissolved solids in the graywater, evaporation of the water can lead to precipitation. To avoid this,

the graywater concentration at the evaporator outlet is restricted such that the least soluble compound only reaches 30% of its solubility limit.

The baseline operating parameters for the cycle are shown in Table 2.2. The ground temperature is based on the temperature in the middle latitudes of the United States (Kusuda and Achenbach, 1965), while the evaporator temperature is set sufficiently low to provide air conditioning. Absorbents are selected from those identified in the work of Boman et al. (2017) but are restricted to those without a volatile component. Engineering Equation Solver is used to solve the model equations (Klein, 2018).

2.4 Model Results

For the cycle developed in Section 2.2, there are inherent limits on the water production rate as the function of the cooling load. To facilitate this discussion, the water output ratio is introduced as a metric. The water output ratio is defined as the ratio of the water production rate to the cooling load in kg day^{-1} kW^{-1} and can range between 0 and 35.2 kg day^{-1} kW^{-1}.

Table 2.2: Cycle baseline operating parameters

Parameter	**Value**
Absorber Temperature (T_{abs})	35°C
Desorber Temperature (T_{des})	100°C
Condenser Temperature (T_{cond})	50°C
Evaporator Temperature (T_{evao})	5°C
Ground Temperature (T_g)	11°C
Closest Approach Temperature (CAT)	2 K
Pump Efficiency (η_{pump})	0.85
SHX Effectiveness (ε_{SHX})	0.85
Water Recovery (WR)	0.95

As the water output ratio changes, the performance of the cycle varies. When considering the ratio of each of the figures of merit defined in Section 2.2.1 to its maximum value, the performance of the cycle is independent of the absorbent selected. It is therefore useful to consider the effect of the water output ratio on cycle performance prior to considering the effect of the absorbent. Figure 2.2 shows the ratios of the COP, the PR, and the ER to their respective maxima as a function of the water output ratio. It can be clearly seen that all three figures of merit increase monotonically with increasing water output ratio. As the water output ratio increases, the water production rate increases. Because the cooling load remains constant, there is minimal change in the input power requirement; thus, the numerator of the PR increases while the denominator remains nearly constant, leading to an overall increase. The COP increases with increasing water output ratio

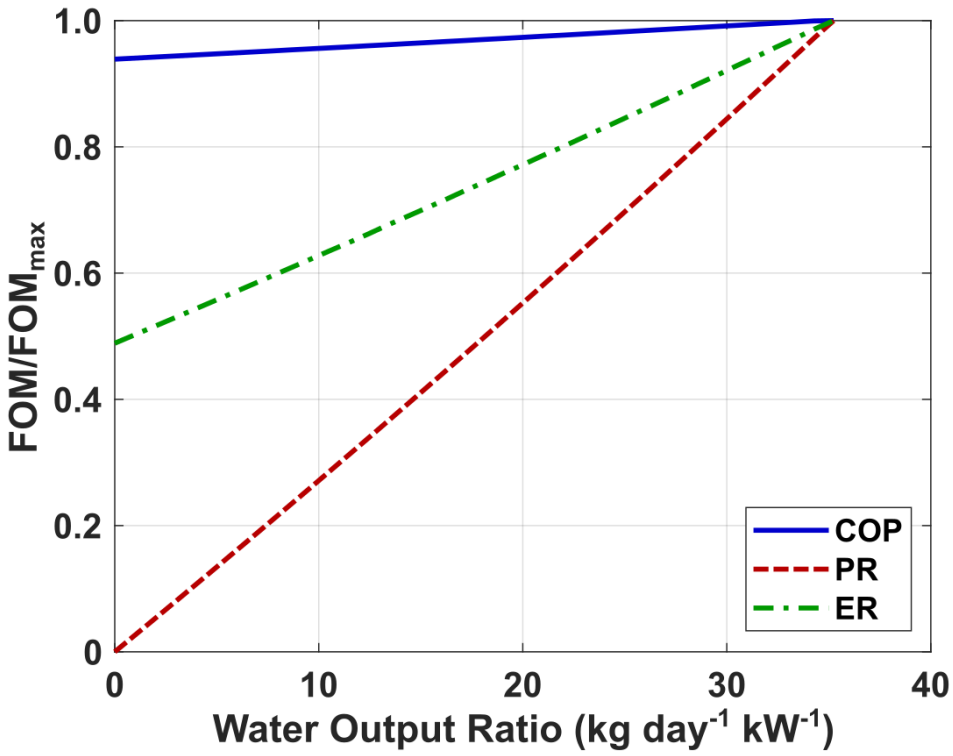

Figure 2.2: Ratios of figures of merit to their maxima as a function of water output ratio

because the average enthalpy of the fluid entering the evaporator decreases. The evaporator has two inlets: one from the condenser, and one from the graywater tank. The temperature of the graywater entering from the tank is lower than the temperature of the water leaving the condenser. Thus, as more water is extracted at the condenser, the fluid entering the evaporator contains a higher proportion of graywater tank, and the enthalpy difference between the inlet and exit increases. This leads to a smaller required refrigerant flow rate and a lower desorber heat input.

With these trends established, it becomes instructive to compare the performance of the nonvolatile absorbents identified in the work of Boman et al. (2017). These absorbents include salts and ionic liquids (ILs), which are salts with melting points near room temperature (Khamooshi et al., 2013). The absorbents studied are shown in Table 2.3, and the references used to calculate their properties are given in Appendix A. The experimental data of Dong et al. (2012) are used with a new set of parameters for the non-

Table 2.3: Investigated absorbents

Absorbent	**Type**
LiBr	Salt
LiBr + $ZnBr_2$ + LiCl (33:59:8)	Salt mixture
LiBr + $ZnCl_2$ + $CaBr_2$ (47:47:6)	Salt mixture
NaOH	Salt
NaOH + KOH + CsOH (10:9:6)	Salt mixture
1,3-dimethylimidazolium dimethyl phosphate ([mmim][DMP])	IL
1-ethyl-3-methylimidazolium dimethyl phosphate ([emim][DMP])	IL
1-ethyl-3-methylimidazolium diethyl phosphate ([emim][DEP])	IL
1-ethyl-3-methylimidzolium tetrafluoroborate ([emim][BF_4])	IL
1-butyl-3-methylimidazolium tetrafluoroborate ([bmim][BF_4])	IL
1-ethyl-3-methylimidzaolium acetate ([emim][Ac])	IL
1-ethyl-3-methylimidazolium bis(trifluoromethylsulfonyl)imide ([emim][Tf_2N])	IL
1-ethyl-3-methylimidazolium thiocyanate ([emim][SCN])	IL
1-butyl-1-methylpyrroldinium dicyanamide ([bmpyr][DCA])	IL

random two-liquid model to calculate the vapor-liquid equilibrium of [mmim][DMP] rather than the data from the work of He et al. (2010) because of the wider range of experimental data available and the better agreement with the literature. Performance is compared at the maximum performance point, which is at a water output ratio of 35.2 kg day^{-1} kW^{-1}. The ER of each of the absorbents, divided into the COP and PR, is shown in Figure 2.3. When compared to the performance ratio of existing large-scale water purification systems, such as MED or RO, the hybrid absorption heat pump cycle has much lower performance. However, it is important to note that the additional energy requirement for water purification in the water-purifying absorption heat pump cycle is the energy needed to run the pump pressurizing the condensate from the condenser pressure to the ambient and the pump circulating the feedwater. When only this energy is considered, the energy cost to add water purification is less than 0.5 kWh m^3.

The variation in performance between absorbents is driven by their thermodynamic properties, with the difference in absorbent concentration between the concentrated and dilute solutions being a major factor in determining the absorbents that will perform well. All of the absorbents in the top four have concentration differences greater than 0.04, while all of the absorbents in the bottom four have concentration differences of less than 0.01. In general, salts and salt mixtures outperform ILs; the exception is LiBr + $ZnCl_2$ + $CaBr_2$, which performs significantly worse than the other salts and salt mixtures. There is a performance gap between the top four absorbents and those performing worse; thus, further consideration is given to the advantages and disadvantages of the top four absorbents. The absorbents demonstrating the best combination of low cost, low complexity, and high performance are NaOH and LiBr. It should be noted, however, that if CO_2 enters the cycle

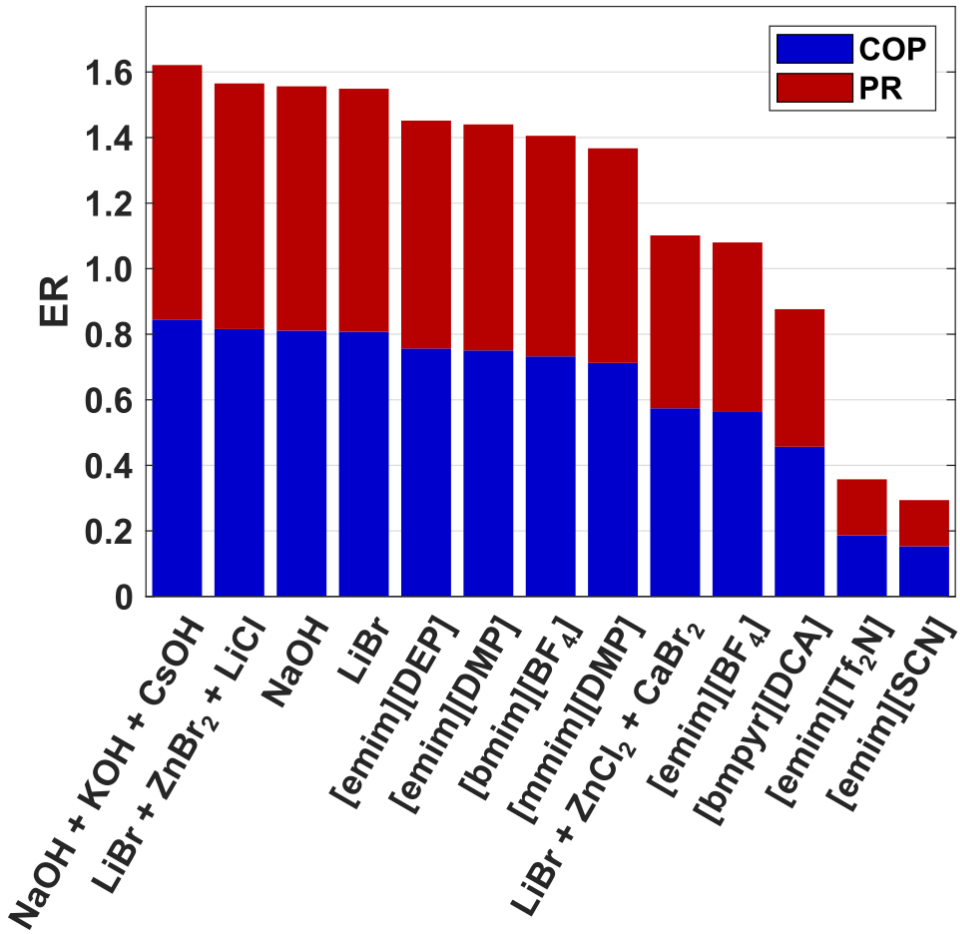

Figure 2.3: Energy ratio of studied absorbents at baseline conditions with water output ratio of 35.2 kg day^{-1} kW^{-1}

with the air dissolved in the feedwater, it can react with the NaOH, eventually converting it to $NaHCO_3$ and reducing the cycle performance.

The temperature of the desorber in the dual-function absorption heat pump cycle determines the heat sources that can be used to drive the cycle. Lower driving temperatures create the possibility of operating the cycle using flat-plate solar collectors or waste heat from low-temperature thermal processes, while higher driving temperatures may improve cycle performance. Figure 2.4 shows the ER of the two absorbents selected above as a function of desorber temperature along with [emim][DEP], which as an IL has no potential

to crystallize. The ER vs desorber temperature curves for all three absorbents follow the typical pattern for such a curve. At low desorber temperatures, the change in concentration of the absorbent between the concentrated solution and dilute solution is very low; therefore, large quantities of solution must be pumped from the absorber to the desorber

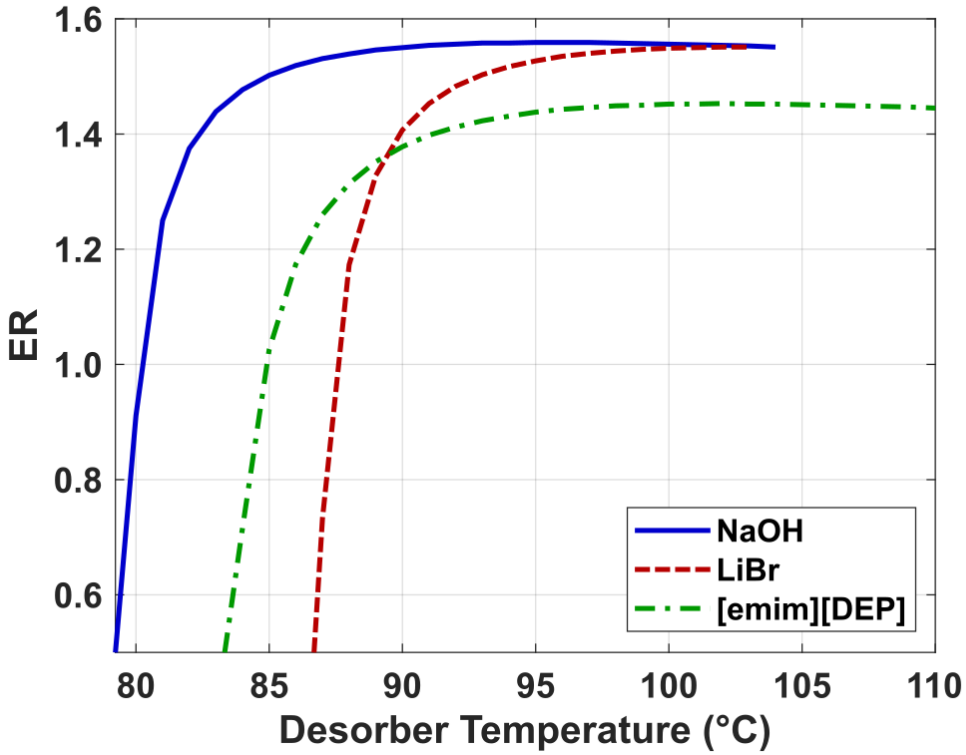

Figure 2.4: ER of selected absorbents as a function of desorber temperature

and heated from the absorber temperature to the desorber temperature (the addition of the SHX reduces the impact of the latter factor, but it does not eliminate it entirely). Therefore, the COP, and thus the ER, is low at low desorber temperatures. As the desorber temperature increases, the change in absorbent concentration between the concentrated and dilute solutions increases rapidly, leading to a rapid increase in the COP. At some point, the additional specific vapor generation in the desorber is offset by the additional heat input required to achieve the higher desorber temperature, and the COP begins to decrease. The

maximum ER for NaOH occurs at 96°C, while the maximum ER for [emim][DEP] occurs at 108°C. LiBr does not reach its maximum ER due to the potential for crystallization.

The limitations on the pure salts are clearly visible in Figure 2.4, as both NaOH and LiBr have strong potential to crystallize at desorber temperatures above 104°C. As the concentrated solution leaves the desorber and enters the SHX, it begins to cool. At the concentrations required to generate sufficient refrigerant vapor for steady-state operation, the concentrated solution drops below its crystallization temperature while still in the SHX, resulting in a strong potential for crystallization.

2.4.1 Further Considerations for Absorbent Selection

In addition to the thermodynamic considerations explored above, there are two additional factors that must be considered when selecting an absorbent for the dual-function absorption heat pump. The first is the thermophysical properties that can affect the heat and mass transfer behavior. These are explored in Section 3.4. The second is related to the production of purified water. If some of the absorbent makes it way into the purified water stream, it should be easily neutralized. Of the two salts considered above, NaOH is substantially better because it is easily neutralized by addition of acid.

2.5 Secondary Water Purification

The cycle developed in Section 2.3 has the potential to provide freshwater and cooling in a variety of applications; however, the water output is limited by the cooling load. For a four-person household in the U.S. with a graywater generation rate of 570 kg day^{-1} and a peak cooling load of 10.5 kW, the water output ratio is 54.3 kg day^{-1} kW^{-1}, which substantially exceeds the water output ratio that can be provided by the previously

developed cycle (Maupin et al., 2014; DeOreo et al., 2016). While these secondary water purification methods will not be demonstrated experimentally in this work, it is worth exploring their integration into the cycle and the impact on performance.

Three methods are considered for secondary water purification in the cycle: forward osmosis (FO), membrane distillation (MD), and HDH. These are shown schematically in Figure 2.5. The FO process is integrated into the absorber, where the flow of low-temperature graywater into the absorbent solution helps to reduce the heat released during absorption. This cycle schematic is shown in Figure 2.5a. The mass balance on the absorber thus becomes

$$\dot{m}_r + \dot{m}_{conc} + \dot{m}_{gray,abs} = \dot{m}_{dil} \tag{2.23}$$

where $\dot{m}_{gray,abs}$ is the mass flow rate of water from the graywater stream into the absorber. Because this stream carries enthalpy with it, Equation 2.12 becomes

$$\dot{Q}_{abs} = \dot{m}_{dil}h_5 - \dot{m}_{conc}h_{10} - \dot{m}_r h_4 - \dot{m}_{gray,abs}\frac{h_{11} + h_{12}}{2} \tag{2.24}$$

Here, the enthalpy of the water entering the absorber from the graywater stream has been set as the average enthalpy between the inlet and outlet. Using alternate graywater inlet conditions to the absorber would reduce the impact of graywater addition of the absorber heat duty.

In the desorber, both the water that enters the absorber from the evaporator and the water that enters the absorber from the graywater stream must be desorbed. Therefore, the mass balance on the desorber is the same as the mass balance on the absorber.

MD is integrated into the desorber, as seen in Figure 2.5b. In MD, enthalpy is carried through the membrane with the vapor, and heat is transferred through the membrane from the hot feed to the cooler distillate (Lin et al., 2014). By incorporating MD at the

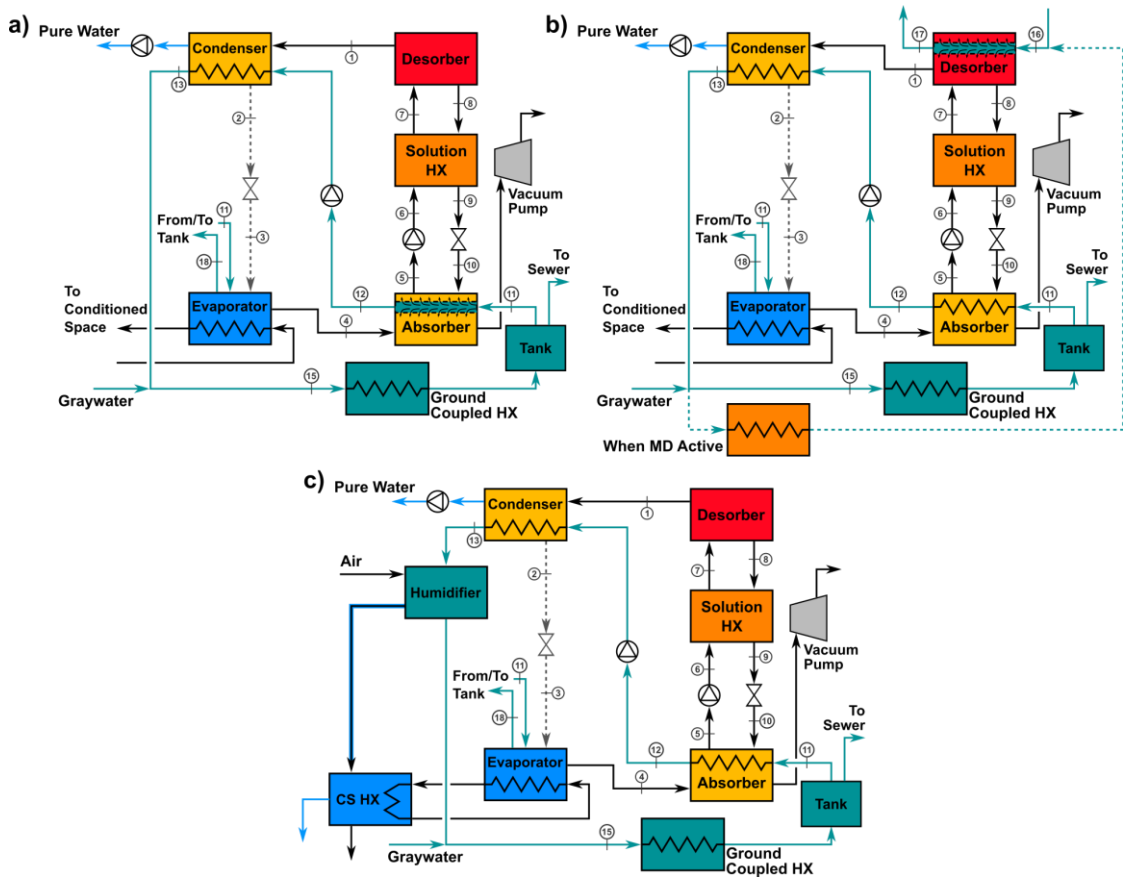

Figure 2.5: Cycle schematics with (a) FO, (b) MD, and (c) HDH for secondary water purification

hottest point in the system, it is ensured that the heat flow through the membrane due to conduction and convection is in the same direction as the heat flow for the component. The addition of MD to the desorber does not cause any change in the mass or species balance – pure water is both added to and removed from the desorber – but the energy balance must be modified to account for the flow of water through the membrane and its subsequent heating.

$$\dot{Q}_{des} = \dot{m}_{conc} h_8 + \left(\dot{m}_r + \dot{m}_{gray,des}\right) h_1 - \dot{m}_{dil} h_7 - \dot{m}_{gray,des} \frac{h_{16} + h_{17}}{2} \quad (2.25)$$

The heat transfer fluid for the desorber that flows through the membrane during the MD process is replenished from the heat transfer fluid stream leaving the condenser. A

fraction of this flow is routed to a heater prior to entering the ground-coupled heat exchanger and is heated to the desorber heat transfer fluid inlet conditions.

$$\dot{Q}_{reheat,MD} = \dot{m}_{gray,des}(h_{16} - h_{13}) \tag{2.26}$$

Therefore, when MD is used as the secondary water purification method, the denominator in the figures of merit is modified to account for the thermal load associated with replenishing the desorber heat transfer fluid as well as the heat duty of the desorber.

$$ER_{MD} = \frac{\dot{Q}_{evap} + \dot{m}_w \times 2257 \text{ kJ kg}^{-1}}{\dot{Q}_{des} + \dot{Q}_{reheat,MD} + \sum_i \dot{W}_{pump,i}} \tag{2.27}$$

Figure 2.5c shows the incorporation of HDH into the cycle. Return air at AHRI rating conditions is split, with a sufficient fraction to provide the additional water load routed to a humidifier along with the graywater leaving the condenser (AHRI, 2017). The warm, humid air is then passed over a heat exchanger that brings chilled water from the evaporator to the conditioned space. Liquid coupling in the evaporator is assumed due to the low pressure drop requirement and the geometries that allow such to occur.

Before adding HDH to the cycle, the state of the air leaving the conditioned space heat exchanger is calculated. An air flow rate of 0.0607 $m^3\ s^{-1}$ kW-cooling^{-1} is assumed based on common air conditioning practice. The air-side flow rate is often limited to this value or lower to reduce noise. The energy balance on the conditioned space heat exchanger is

$$\begin{aligned}\dot{Q}_{evap} = \dot{m}_{air}\big[&h_{air,in} + \omega_{in}h_{wa,in} - h_{air,out} - \omega_{out}h_{wa,out} \\ &- (\omega_{in} - \omega_{out})h_{w,out}\big]\end{aligned} \tag{2.28}$$

where the subscript *wa* refers to water in the air, $h_{w,out}$ is the enthalpy of liquid water that condenses out of the air as the air cools, and ω is the humidity ratio of the air.

The species balance for water on the conditioned space heat exchanger is

$$\dot{m}_{air}(\omega_{in} - \omega_{out}) = \dot{m}_{w,out} \tag{2.29}$$

This flow of water is not counted in the water production rate from HDH, as it is produced by all configurations of the cycle.

When HDH is needed to satisfy the water load, additional species and energy balances must be used. The evaporator heat duty of the cycle will increase with additional water load because air enters the conditioned space heat exchanger at higher temperature and humidity. However, the increase in evaporator duty does not produce any additional cooling. Therefore, the COP is modified to consider only the heat transfer associated with cooling and not that associated with water production.

$$COP_{HDH} = \frac{\dot{Q}_{evap,nom}}{\dot{Q}_{des} + \sum_i \dot{W}_{pump,i}} \tag{2.30}$$

The nominal evaporator heat duty, $\dot{Q}_{evap,nom}$, is calculated using Equation 2.28.

As discussed above, only a portion of the air entering the system flows through the humidifier. The remainder bypasses it and mixes with the humidified air such that

$$\dot{m}_{HDH} = \dot{m}_{air}(\omega_{mix} - \omega_{in}) \tag{2.31}$$

The inlet humidity ratio is used instead of the outlet humidity ratio because the water condensed from the air during normal operation is neglected. With the mixture humidity ratio determined, and assuming the air leaving the humidifier is saturated, it becomes possible to determine the air flow rate through the humidifier.

$$\dot{m}_{air}\omega_{mix} = \left(\dot{m}_{air} - \dot{m}_{air,hum}\right)\omega_{in} + \dot{m}_{air,hum}\omega_{hum} \tag{2.32}$$

In the humidifier, the graywater leaving the condenser is used to saturate the air entering the system. A species balance for water on the humidifier gives

$$\dot{m}_{gray,HTF} + \dot{m}_{air,hum}\omega_{in} = \dot{m}_{gray,hum,out} + \dot{m}_{air,hum}\omega_{hum} \tag{2.33}$$

An energy balance on the humidifier, assuming it is well-insulated, gives

$$\begin{aligned} \dot{m}_{gray,HTF}h_{13} + \dot{m}_{air,hum}\left(h_{air,in} + \omega_{in}h_{wa,in}\right) \\ = \dot{m}_{gray,hum,out}h_{gray,hum,out} \\ + \dot{m}_{air,hum}\left(h_{air,hum} + \omega_{hum}h_{wa,hum}\right) \end{aligned} \tag{2.34}$$

After being humidified, the air is cooled and dehumidified in the conditioned space heat exchanger. The energy balance for this heat exchanger is

$$\begin{aligned} \dot{Q}_{evap} = \dot{m}_{air}\big[h_{air,hum} + \omega_{hum}h_{wa,hum} - h_{air,out} - \omega_{out}h_{wa,out} \\ - (\omega_{hum} - \omega_{out})h_{w,out}\big] \end{aligned} \tag{2.35}$$

As the evaporator heat duty increases, the rate of vapor generation in the evaporator increases, leading to a higher water output ratio in the evaporator.

2.5.1 Cycle Performance with Secondary Water Purification

The ER for all three methods of secondary water purification at high water output ratios with NaOH as the absorbent are shown in Figure 2.6. For all three methods of secondary water purification, the ER decreases with increasing water output ratio. In all cases, the cooling load provided to the conditioned space remains constant, but the power input to the cycle increases. For FO, more solution has to be heated and desorbed; for MD, graywater has to be heated from the condenser outlet conditions to the desorber inlet conditions; for HDH, the evaporator must provide additional cooling.

Of the three methods explored, HDH performs the best, showing only a 4% decrease in ER over the range studied, compared with a 19% decrease for MD and a 26% decrease for FO. The cycle with MD outperforms the one with FO because both of the

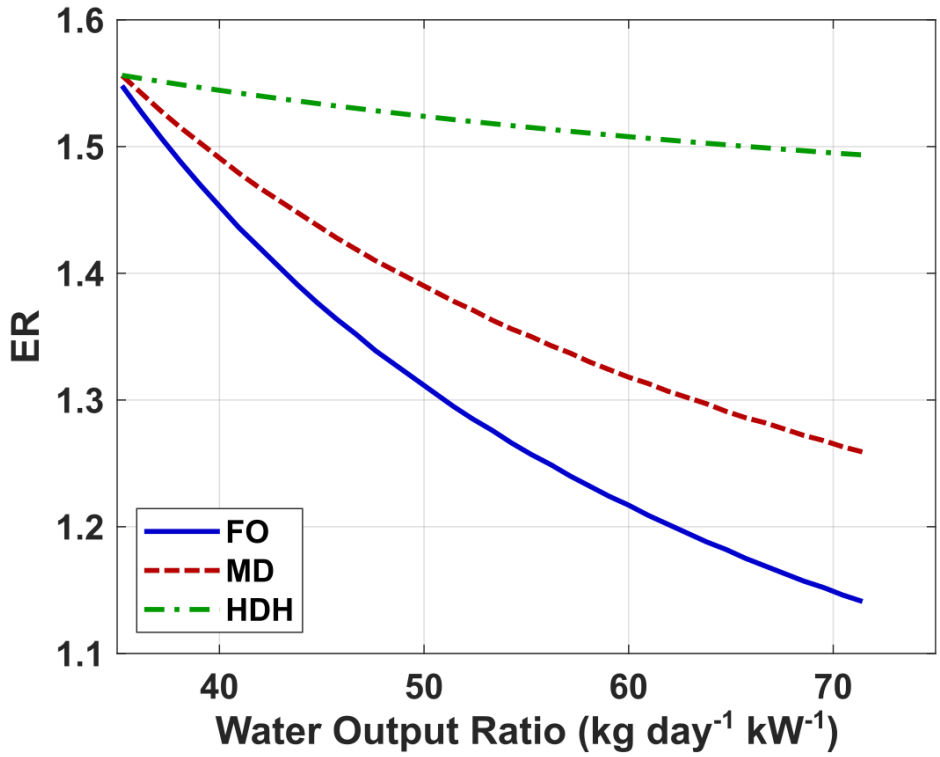

Figure 2.6: Performance of cycles with secondary water purification at baseline conditions using NaOH as the absorbent

heating requirements are smaller – the sensible heating in the cycle with MD starts at a higher temperature because the heat rejection of the absorber and condenser is used to preheat the feed, and the latent heat of vaporization in MD does not include the heat of mixing of the absorbent solution. The cycle using HDH for secondary water purification outperforms both because it increases its primary water production rate every time it increases its secondary water production rate. As the HDH water production rate increases, the evaporator heat duty increases, and as the evaporator heat duty increases, the rate at which pure water can be recovered from the condenser increases. Taken together, these factors mean that for every increment in desorber heat load, the water production rate is

being incremented twice: once from the additional water condensed from the humidified air, and once from the additional vapor being generated in the evaporator.

2.6 Conclusion

A dual-function absorption heat pump capable of providing air conditioning and graywater purification is designed. The features incorporated in the design are guided by previous studies of multi-function absorption heat pumps, along with multi-function adsorption heat pumps and enhanced vapor compression refrigeration systems. A thermodynamic model of the cycle is developed and simulated under representative operating conditions for air conditioning with 14 different absorbents. Based on the results of these simulations, NaOH and LiBr are selected as the most suitable.

The production of pure water from the vapor generated in the evaporator places an upper limit on the amount of water that can be produced for a given cooling load. To address this challenge, cycle designs that incorporate methods for additional water purification are studied. FO, MD, and HDH are suggested as secondary water purification methods. Comparison of these cycles with NaOH as the absorbent indicates that HDH is the best performing secondary water purification method. Although these high-water production configurations are not examined experimentally in this work, the analysis suggests future directions for research.

CHAPTER 3. HEAT EXCHANGER DESIGN AND MODELING

To realize the dual-function absorption heat pump designed in Section 2.2, the primary heat exchangers required for operation (i.e., absorber, desorber, condenser, and evaporator) must be designed. The pure water output of the cycle requires that droplets of feedwater not be carried over from the evaporator to the absorber and that droplets of absorbent solution not be advected from the desorber to the condenser. Thus, heat exchanger designs that address this design constraint are developed. Design models are developed to determine the heat exchanger geometry required to satisfy the state points of the cycle model, and the thermodynamic states of the working and coupling fluids in these heat exchangers are reported.

3.1 Horizontal-Tube, Falling-Film Heat Exchangers

Heat transfer with phase change on horizontal tubes has been studied for over a century, with one of the first investigations being that by Nusselt (1916) on condensation. Since then, this architecture has been utilized for evaporation (Thome, 1999; Ribatski and Jacobi, 2005; Bustamante and Garimella, 2014; Fernández-Seara and Pardiñas, 2014; Bustamante et al., 2020), condensation (Browne and Bansal, 1999; Bonneau et al., 2019), absorption (Killion and Garimella, 2001; Killion and Garimella, 2003b; Narváez-Romo et al., 2017), and desorption (Fujita, 1993; Narváez-Romo et al., 2017), among other applications. The horizontal tube architecture gained popularity in the late 1970s when it was investigated for evaporation in ocean thermal energy systems (Thomas et al., 1979; Yung et al., 1980; Lorenz and Yung, 1982). Over the course of these investigations and the

subsequent decades, several advantages of horizontal-tube, falling-film heat exchangers have been discovered. Because the entirety of the falling film is exposed to the vapor, the pressure drop within the heat exchanger is negligible. When compared to pool boiling evaporators and desorbers, falling-film designs require reduced charge and exhibit increased heat transfer coefficients due to the typically thin falling films, which reduces the required size of the system (Thome, 1999; Roques and Thome, 2007). In absorbers and desorbers, the formation of droplets or columns between the tubes leads to an increase in surface area for mass transfer, and the time required for droplets to develop substantially increases the mass transfer rate during absorption (Jeong and Garimella, 2002; Subramaniam and Garimella, 2014). While an extensive review of heat and mass transfer in falling films over horizontal tubes is beyond the scope of this work, the major phenomena associated with heat exchangers of this type are discussed below.

The three major patterns that occur in gravity-driven flow over horizontal tubes – droplets, columns (or jets), and sheets – are shown in Figure 3.1. The transitions between these modes are governed by several factors, although the most important are the liquid flow rate, which is represented non-dimensionally by the Reynolds number, and the interaction between inertia and surface tension, which is represented by the Kapitza number

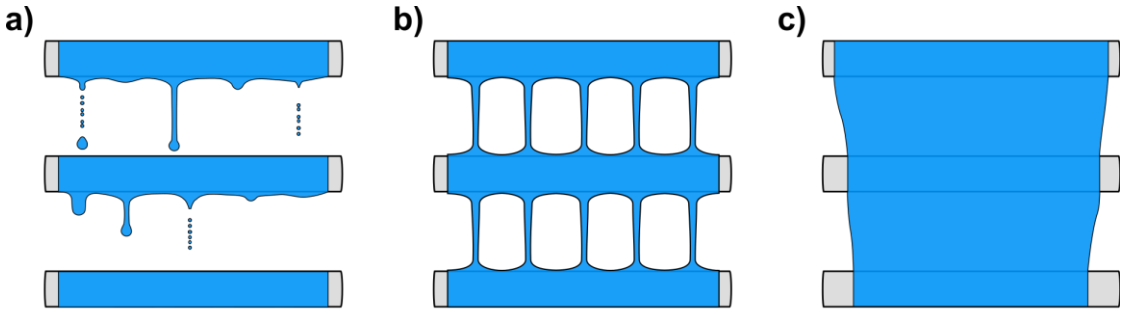

Figure 3.1: Gravity-driven falling-film flow over horizontal tubes in the a) droplet, b) column, and c) sheet regimes

(Hu and Jacobi, 1996a; Mitrovic, 2005; Wang and Jacobi, 2014). The spacing between the tubes can influence the flow pattern as well. As the spacing increases for flows in droplet mode, there is a higher probability of the formation of instabilities in the filament left behind after droplet impact occurs, which leads to the formation of secondary droplets (Yung et al., 1980; Killion and Garimella, 2003a; Liu et al., 2019). On the other hand, when the spacing between the tubes is small, the liquid reaches the next row of the tube bank without droplet formation in the intervening space, which can reduce heat and mass transfer by reducing droplet residence time and surface area and suppressing droplet mixing (Subramaniam and Garimella, 2014).

The flow pattern influences heat transfer through two major factors: film thickness and tube wetting. For all phase change phenomena, a thinner film leads to a higher heat transfer coefficient because the conduction length through the film decreases. Thus, at lower flow rates with a uniform film on the tube, the heat transfer rate is substantially higher (Nicol et al., 1988; Belghazi et al., 2001; Zheng et al., 2017). However, at low flow rates, dry patches tend to form on the tubes, reducing the average heat transfer coefficient for evaporation, absorption, and desorption (Fujita and Tsutsui, 1998). The flow regimes associated with each Reynolds number and their associated heat transfer coefficients for sensible heat transfer were studied by Hu and Jacobi (1996b), and they clearly show that the heat transfer coefficient increases with increasing flow rate until sheet mode is achieved. Similar studies exist for heat transfer with phase change, with investigations into falling-film evaporation (Ribatski and Thome, 2007; He et al., 2011; Bustamante and Garimella, 2014; Bock et al., 2019; Bustamante et al., 2020), absorption (Fujita, 1993;

Kyung et al., 2007; Nagavarapu and Garimella, 2019a, b), and desorption (Olbricht and Luke, 2018) demonstrating similar trends.

Beyond film thickness and wetting, heat transfer is affected by the size of the tubes used. Multiple investigators have reported that smaller diameter tubes exhibit higher heat transfer coefficients (Gogonin and Dorokhov, 1976; Parken et al., 1990; Meacham and Garimella, 2004; Determan, 2005; Ribatski and Jacobi, 2005; Nagavarapu and Garimella, 2019a, b). Jeong and Garimella (2005) discuss the reasons for this during absorption. During droplet formation, additional absorption or desorption occurs, and with more tubes in the same space, more droplets are formed. In addition, the residence time for a given fluid particle is higher because its velocity decreases during droplet formation.

3.2 Droplet Entrainment

Whenever liquids and gases are in contact, there is the potential for droplets of the liquid to be carried along by the gas. In thermal water purification processes, such as MSF, this results in a decrease in water quality (Ettouney, 2005). Two phenomena must occur for entrainment: the first is that droplets must be generated, and the second is that those droplets must be carried by a gas stream. In systems that use pool or nucleate boiling, flashing, or bubbling processes, shattering of the interface between the gas bubble and the surrounding liquid can result in the formation of small droplets. If the vapor velocity is sufficiently high, these droplets can be carried with the vapor (Thomas et al., 1979; Isao and Mamoru, 1984; Xiong et al., 2005). It should be noted that nucleate boiling can be avoided in falling films by using a sufficiently low wall superheat (Kim and Kim, 1999) and that high surface tension and low vapor density increase the heat flux required for the

onset of nucleate boiling (Steiner and Taborek, 1992; Olbricht and Luke, 2018). In addition to nucleate boiling, liquid can be entrained in falling films through vapor shear. Differences in the liquid and vapor velocity lead to perturbations in the liquid-vapor interface. When these perturbations grow sufficiently large, they lead to the formation of droplets. At that point, the high vapor velocity entrains the droplets (Ishii and Grolmes, 1975; Honda et al., 1991). Investigators have shown experimentally that the rate of generation of liquid droplets increases with the heat flux and increases slightly with film thickness for falling-film evaporation on vertical tubes (Ueda et al., 1981). A theoretical investigation of falling films on horizontal tubes by Yung et al. (1980) determined the vapor velocity required to strip droplets from falling liquid films on horizontal tubes as well as the velocity required to deflect droplets such that they would miss the next tube row. The velocity required to strip droplets from the tubes is substantially higher than the velocity required for deflection. To determine if the designs for the heat and mass exchangers in this work need to account for stripping and deflection of droplets, their analysis is applied to some preliminary geometries.

Due to the increase in heat transfer coefficient with decreasing tube size, tubes with an outer diameter of 3.175 mm are selected. A center-to-center spacing of 12.7 mm is considered as an upper bound on the design. Based on the results of the cycle model presented in Section 2.4, three fluids – water, LiBr, and NaOH – are investigated. The temperatures and pressures of the fluids in the heat exchangers are determined from these results.

The diameter of the droplets that form as the fluid film falls from tube to tube can be calculated by

$$d_p = C_1 \sqrt{\frac{\sigma}{\rho_\ell g}} \tag{3.1}$$

where C_1 is a constant that has a value of 3 for water and ethanol (Yung et al., 1980). For these calculations, it is taken as that value for all fluids. When these primary droplets break off, the filament that remains can shatter into smaller droplets known as secondary droplets (Yung et al., 1980; Killion and Garimella, 2003a; Liu et al., 2019). The diameter of these droplets can be expressed as a fraction of the diameter of the primary droplet, and it is the smallest of these droplets that has the highest potential to be deflected or entrained (Yung et al., 1980).

$$d_{min} = 0.24 d_p \tag{3.2}$$

The crossflow vapor velocity required to deflect a droplet such that it fails to impinge on the next tube in the row is

$$u_{g,min} = \left(\frac{3}{2}\frac{\rho_\ell}{\rho_v} dg\right)^{\frac{1}{2}} \left[\frac{s}{D}\left(\frac{s}{D} - 1\right)\right]^{-\frac{1}{4}} \tag{3.3}$$

where *s* is the center-to-center tube spacing and *D* is the tube diameter (Yung et al., 1980). The surface tension of LiBr solution is taken from work by Yao et al. (1991). The surface tension of NaOH solution is extrapolated from a review by Kurt and Bittner (2006). The density of sodium hydroxide is taken from Perry's Handbook (Green and Perry, 2008). The remaining properties are calculated using Engineering Equation Solver (EES) (Klein, 2018).

Because the density of the vapor differs between components, it is useful to compare the required vapor flow area for each of the components to determine if it is

reasonable. In each of the heat exchangers, the mass flow rate of vapor is the required refrigerant flow rate, which is 4.3 g s^{-1}. Thus,

$$A_{min} = \frac{\dot{m}_r}{\rho_v u_{g,min}} \tag{3.4}$$

For each of the fluids considered, the minimum vapor flow area to avoid droplet deflection for an absorption heat pump with a cooling load of 10.5 kW is given in Table 3.1. The largest area requirement occurs in the low-pressure heat exchangers due to the low density of the vapor at those pressures. For LiBr and NaOH, this is the absorber, while for water, this is the evaporator. The required flow area is small compared to the flow areas demonstrated in the literature for similar heat exchangers, suggesting that deflection or

Table 3.1: Minimum vapor flow areas to avoid droplet deflection

Fluid	**Area (m^2)**
LiBr	0.016
NaOH	0.016
Water	0.018

entrainment of droplets due to vapor crossflow is unlikely to be a concern (Goel and Goswami, 2007).

3.3 Heat Exchanger Design Model

The same horizontal-tube, falling-film heat exchanger design, shown in Figure 3.2, is used for both the desorber and absorber. Therefore, a design model is developed to predict the performance of the heat exchanger as a function of the geometry and fluid properties. The heat exchanger design studied uses two columns of horizontal tubes with an outer diameter of 3.175 mm and a wall thickness of 0.51 mm. Absorbent solution enters the heat exchanger through a tube with an outer diameter of 6.35 mm and a wall thickness

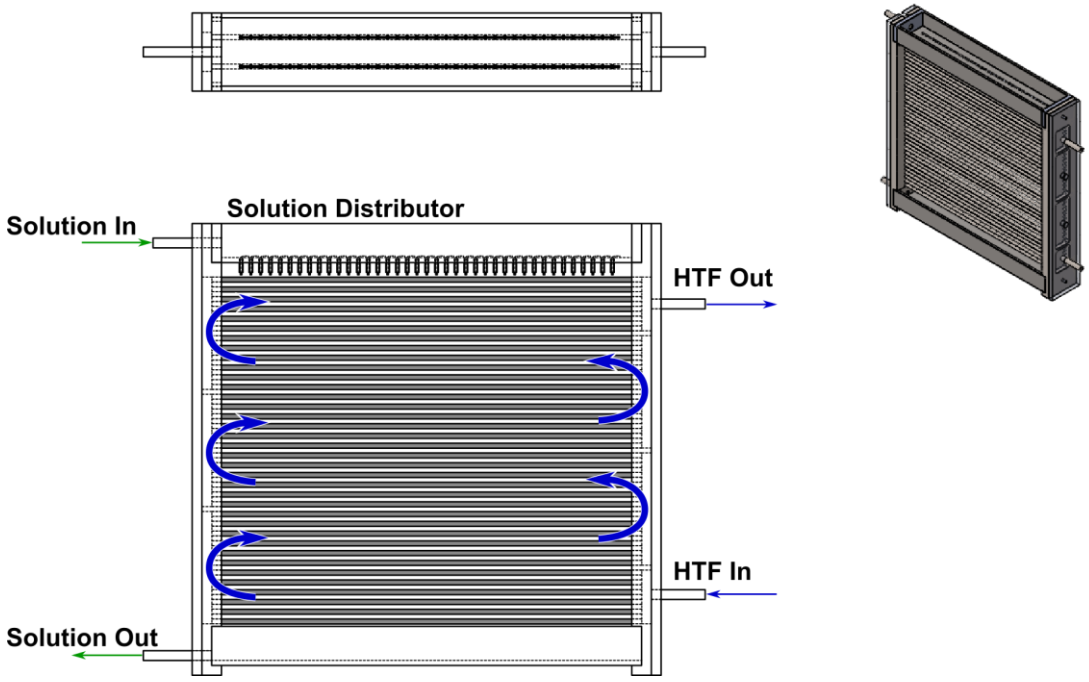

Figure 3.2: Horizontal-tube, falling-film heat exchanger design

of 0.89 mm and flows into a distributor, the design of which is discussed in section 3.5. The solution then flows down over the 36 rows of tubes to an outlet header, where it exits the heat exchanger through another 6.35-mm diameter tube. The center-to-center spacing between tube rows is 6.35 mm. This allows for a more compact heat exchanger than the spacing analyzed for droplet entrainment (12.7 mm). Heat transfer fluid (HTF) enters the heat exchanger through a 6.35-mm tube connected to a header, which distributes the flow into the lowest six tubes in each column (12 tubes in total). At the end of the tube pass, the HTF enters another header, which redistributes the flow from the first 12 tubes to the next 12 tubes. The 36 rows of the heat exchanger are divided into six passes, with six rows in each pass. Stainless steel is used for all solid surfaces due to its high corrosion resistance. The demonstration system is designed for a cooling capacity of 300 W and a maximum expected primary water purification capacity of 10.55 kg day^{-1}.

Within a row, two control volumes – the heat transfer fluid within the tubes and the falling liquid film on the outside of the tubes – are considered. Operation is simulated in steady state.

On each row of tubes, a mass balance is written for the solution.

$$\dot{m}_{\ell,i} - \dot{m}_{\ell,i+1} = \dot{m}_{lv,i} \tag{3.5}$$

The subscript ℓ refers to the liquid solution on the tubes, the subscript *lv* refers to phase change between liquid and vapor, and *i* is the row index. The uppermost row is defined as the first row. The rate of vapor generation is defined as positive when vapor is being generated.

A species balance is written for each row of tubes.

$$\dot{m}_{\ell,i} w_i = \dot{m}_{\ell,i+1} w_{i+1} \tag{3.6}$$

In the above equation, *w* represents the mass fraction of absorbent.

The species balance can be closed in two ways. In the first, the solution is assumed to be saturated at the exit of each tube row. This fixes w_{i+1}, which allows the desorption rate to be calculated. (In the case of absorption, the desorption rate is negative.) In the second, the rate of desorption, $\dot{m}_{lv,i}$, is calculated using a convective mass transfer equation

$$\dot{m}_{lv,i} = \beta_{\ell,i} A_o \rho_i \left(w_{eq,i} - w_i\right) \tag{3.7}$$

where w_{eq} is the absorbent equilibrium concentration at the solution temperature and pressure

$$w_{eq,i} = w\left(T_{\ell,i}, p\right) \tag{3.8}$$

and ρ_i is the density of the solution on the tube row. The correlation of Babadi and Farhanieh (2005) is used to calculate the mass transfer coefficient during absorption. In

their work, two mass transfer coefficients are developed where the transition between them occurs at a critical Reynolds number

$$Re_{crit} = \left(\frac{Sc}{5367}\right)^{-3.61} \tag{3.9}$$

where the Schmidt number, *Sc*, is

$$Sc = \frac{\nu}{D} \tag{3.10}$$

The diffusivity of LiBr is taken from the work of Miller (1998). For LiBr under absorber conditions, the Schmidt number is ~2500; therefore, the critical Reynolds number given by Equation 3.9 is ~15. Due to the small tube diameter, high viscosity, and low flow rates associated with the prototype absorber, typical Reynolds numbers are an order of magnitude lower. Therefore, the Sherwood number correlation for absorption from the work of Babadi and Farhanieh (2005) is given by:

$$Sh = 1.03Re^{-0.146}\left(\frac{Sc}{1000}\right)^{1.42} \tag{3.11}$$

For desorption, the work of Olbricht and Luke (2018) suggests that with the selection of the appropriate heat transfer correlation, the heat transfer of a falling-film, horizontal-tube desorber can be predicted without explicitly modeling the mass transfer. However, the mass transfer correlation of Jani (2012) is also explored. It should be noted that the mass transfer correlation of Jani (2012) is valid for Reynolds numbers between 100 and 500. The typical Reynolds number during desorption for the heat exchanger studied here is two orders of magnitude lower, suggesting that this correlation may not be applicable. This is discussed further in Section 3.4.

Energy balances are written for the solution on the tubes and the heat transfer fluid within the tubes. To reduce the computational load when solving the model, each row of

tubes is treated as a single control volume; thus, the average temperature of the heat transfer fluid within a given tube row is used when calculating heat transfer rates for that tube row. The energy balance on the solution is

$$\dot{Q}_i = \dot{m}_{\ell,i+1} h_{\ell,i+1} - \dot{m}_{\ell,i} h_{\ell,i} + \dot{m}_{lv,i} h_{v,i} \tag{3.12}$$

where $h_{\ell,i}$ is the specific enthalpy of the solution. In a desorber or evaporator, $h_{v,i}$ is the enthalpy of the vapor generated through the desorption process. It is assumed that the vapor is generated at the same temperature as the solution. In an absorber or condenser, $h_{v,i}$ is the enthalpy of the vapor entering the component.

The energy balance on the heat transfer fluid within the tubes is

$$\dot{Q}_i = \dot{m}_{HTF,row}\left(h_{HTF,i,out} - h_{HTF,i,in}\right) \tag{3.13}$$

where the subscript HTF refers to the heat transfer fluid. For this model, liquid water is used as the heat transfer fluid. To reduce pressure drop for the heat transfer fluid, headers distribute heat transfer fluid into multiple rows simultaneously. At the end of each row, the heat transfer fluid enters another header, where it mixes and redistributes, as shown in Figure 3.2. Thus, the enthalpy of the heat transfer fluid in each header is given by

$$h_{header,j} = \frac{1}{N_{rp}} \sum_{i=(j-1)N_{rp}+1}^{jN_{rp}} h_{HTF,i,out} \tag{3.14}$$

where N_{rp} is the number of rows in each pass of the heat transfer fluid and j is the number of the header. The enthalpy of the heat transfer fluid entering the tubes is the same as the enthalpy of the header at that inlet.

The heat transfer rate on the tubes is related to the solution and wall temperatures by

$$\dot{Q}_i = \alpha_{\ell,i} A_o \left(T_{w,i} - \frac{T_{\ell,i} + T_{\ell,i+1}}{2} \right) \tag{3.15}$$

where $\alpha_{\ell,i}$ is the convective heat transfer coefficient for the solution in that row, A_o is the outer surface area of all tubes in the row, and $T_{w,i}$ is the temperature of the outer surface of the tubes in that row. For desorption, the solution heat transfer coefficient is determined using the correlation of Hu and Jacobi (1996b) in the droplet mode, as suggested by the low flow rate and the experiments of Olbricht and Luke (2018). For absorption, the convective heat transfer correlation developed by Park et al. (2003) is used.

The heat transfer rate is related to the heat transfer fluid and wall temperatures by

$$\dot{Q}_i = \left(\frac{1}{\alpha_{HTF,i} A_{in}} + \frac{\ln \frac{d_o}{d_{in}}}{2\pi L k_w} \right)^{-1} \left(\frac{T_{HTF,d,in} + T_{HTF,d,out}}{2} - T_{w,i} \right) \tag{3.16}$$

where D is the tube diameter, $\alpha_{HTF,i}$ is the convective heat transfer coefficient for the heat transfer fluid, which is assumed to be for fully developed laminar flow (under baseline conditions, the Reynolds number of the heat transfer fluid is less than 1000) with constant surface heat flux, A_{in} is the inner surface area of the tube row, L is the length of a row, and k_w is the tube wall thermal conductivity, taken here to be that of stainless steel.

Based on the performance of the cycle presented in Section 2.4, designs for the desorber and absorber are developed with LiBr and NaOH as absorbents. The solution inlet and outlet conditions, and the flow rates of heat transfer fluid are specified in the thermodynamic model. These are shown for the desorber and absorber at the cycle baseline operating conditions in Table 3.2. The inlet and outlet temperatures of the heat transfer fluid are determined by its flow rate and the heat duty required to change the temperature and concentration of solution to the outlet conditions.

Table 3.2: Desorber and absorber operating conditions at cycle baseline conditions

	LiBr	**NaOH**
Desorber Heat Duty (W)	371	370
Desorber HTF Flow Rate (g s^{-1})	4.65	4.65
Desorber Solution Inlet Temperature (°C)	80.9	74.1
Desorber Solution Outlet Temperature (°C)	100	100
Absorber Heat Duty (W)	350	348
Absorber HTF Flow Rate (g s^{-1})	4.46	4.45
Absorber Solution Inlet Temperature (°C)	44.9	44.7
Absorber Solution Outlet Temperature (°C)	35	35
Dilute Solution Flow Rate (g s^{-1})	1.24	0.528
Concentrated Solution Flow Rate (g s^{-1})	1.12	0.406
Dilute Solution Absorbent Concentration (wt%)	55.7	40.4
Concentrated Solution Absorbent Concentration (wt%)	61.7	52.6
Desorber Operating Pressure (kPa)	12.35	
Absorber Operating Pressure (kPa)	0.858	

3.4 Model Results

A simple heat transfer analysis can be conducted to ensure that both NaOH and LiBr are suitable absorbents for use in the desorber and absorber. For this analysis, the baseline operating conditions are used with a tube length of 0.21 m. The heat duty of the components can be related to the temperature difference between the heat transfer fluid and the solution by

$$\dot{Q} = UA\Delta T_{LM} \tag{3.17}$$

where the log-mean temperature difference is

$$\Delta T_{LM} = \frac{\left(T_{HTF,in} - T_{soln,out}\right) - \left(T_{HTF,out} - T_{soln,in}\right)}{\ln\left(\frac{T_{HTF,in} - T_{soln,out}}{T_{HTF,out} - T_{soln,in}}\right)} \tag{3.18}$$

To calculate the overall heat transfer conductance, the following equation is used.

$$\frac{1}{UA} = \frac{1}{\alpha_{HTF} A_{in}} + \frac{\ln \frac{d_o}{d_{in}}}{2\pi L k_w} + \frac{1}{\alpha_\ell A_o} \tag{3.19}$$

The convective heat transfer coefficients are calculated using properties evaluated at the average temperature and concentration. The heat duty can also be related to the heat transfer fluid properties.

$$\dot{Q} = \dot{m}_{HTF} c_{p,HTF} \left(T_{HTF,in} - T_{HTF,out} \right) \tag{3.20}$$

Solving Equations 3.17 and 3.20 allows a preliminary calculation of the heat transfer fluid inlet and outlet temperatures. Table 3.3 shows the solution-side heat transfer coefficient, the overall conductance, and the inlet and outlet heat transfer fluid temperatures for each of the absorbent solutions on the absorber and desorber. From these results, several conclusions can be drawn. The first and most important is that NaOH is not a viable absorbent because of its poor heat transfer performance. While the performance of the desorber is similar for both absorbents, the required LMTD in the absorber is so high for NaOH that no conventional heat transfer fluid could be used. For this reason, NaOH is discarded as a viable absorbent. The high LMTD for NaOH in the absorber is due to two factors. First, as shown in Table 3.2, the flow rate of NaOH is ~60% lower than the flow

Table 3.3: Results of preliminary absorber and desorber calculations

	LiBr	**NaOH**
Desorber Solution Heat Transfer Coefficient (W m^{-2} K^{-1})	535	265
Desorber Log-Mean Temperature Difference (K)	7.2	11.9
Desorber Overall Conductance (W K^{-1})	51.2	31.1
Desorber HTF Inlet Temperature (°C)	107.2	108.7
Desorber HTF Outlet Temperature (°C)	88.2	89.8
Absorber Solution Heat Transfer Coefficient (W m^{-2} K^{-1})	122	16.5
Absorber Log-Mean Temperature Difference (K)	21.7	142.6
Absorber Overall Conductance (W K^{-1})	16.1	2.4
Absorber HTF Inlet Temperature (°C)	9.0	-111.8
Absorber HTF Outlet Temperature (°C)	27.0	-93.9

rate of LiBr. Second, the viscosity of NaOH is substantially higher than LiBr under absorber conditions (15 mPa s vs 5 mPa s). These two factors combine to reduce the Reynolds number by nearly an order of magnitude. The solution-side heat transfer coefficient is proportional to $Re^{0.688}$; therefore, a reduction in the Reynolds number by an order of magnitude leads to a reduction in the solution-side heat transfer coefficient by a factor of 5. The further reduction is caused by differences in the film thickness and thermal conductivity.

Furthermore, it can be seen from the table that the overall conductance is higher for the heat exchanger when operating as a desorber than when operating as an absorber. This is due to primarily to the lower viscosity at higher temperature. Coupled with the fact that the absorber heat transfer fluid needs to enter at low temperature, this suggests that absorber operation is the controlling factor when selecting operating conditions and geometry for the heat exchanger.

Before addressing the operating conditions and the tube length of the heat exchanger, the results of the inclusion of mass transfer effects are discussed. The data used by Babadi and Farhanieh (2005) to develop their correlations extend to a Reynolds number of 7.5, which is close to the Reynolds number range of 1-2 projected for the absorber designed in this work. Therefore, it is expected that the correlation will work well. Figure 3.3 shows the solution temperature on each tube row for the absorber with 0.21-m long tubes with and without the mass transfer correction. For the absorber, the inclusion of a mass transfer coefficient has the expected effect. The solution must be slightly subcooled to achieve the desired mass transfer. Throughout the heat exchanger, the solution temperature is 2-4 K cooler when mass transfer is accounted for. To achieve the same

change in solution concentration while overcoming the additional mass transfer resistance, additional sensible cooling of the solution is required. Thus, including mass transfer results in a lower solution outlet temperature (32.7°C vs. 35.0°C) and a larger heat duty (355 W vs. 349 W).

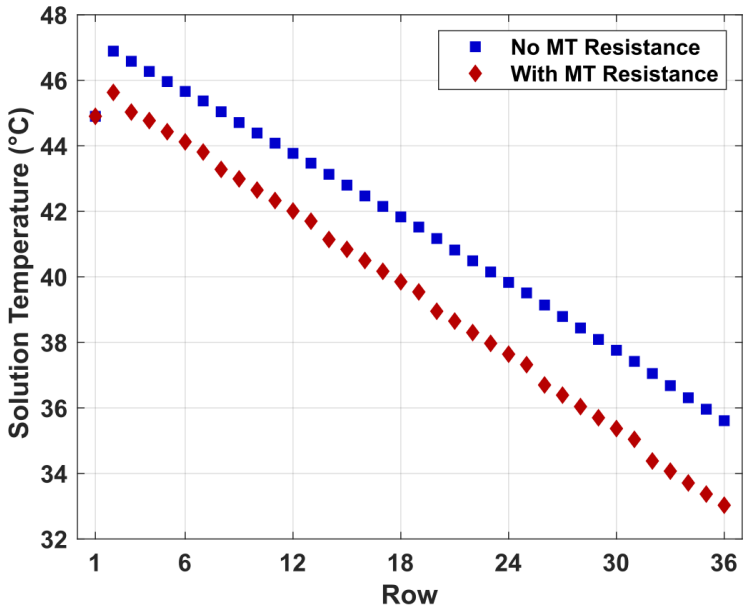

Figure 3.3: Absorber solution temperatures with and without mass transfer resistance

In contrast, the minimum Reynolds number considered by Jani (2012) was 100, which is nearly two orders of magnitude higher than the typical Reynolds number on the desorber (~3). Thus, the mass transfer correlation is substantially extrapolated to account for the operating conditions in the desorber for this work. Figure 3.4 shows the solution temperature on each tube row for the desorber with 0.21-m long tubes with and without the mass transfer correction. This correlation suggests that the solution needs to be superheated by nearly 50 K to achieve the required vapor generation rate, which is physically unlikely. With this large a superheat, the solution would transition to a nucleate boiling regime,

which would generate bubbles near the wall independent of the mass transfer resistance in the film. For this reason, mass transfer resistance is neglected in the desorber model.

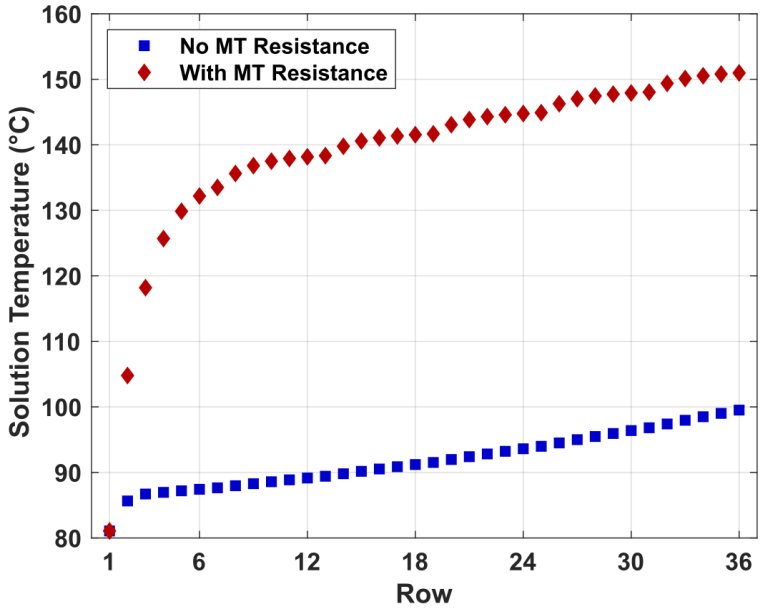

Figure 3.4: Desorber solution temperatures with and without mass transfer resistance

The length of the tubes in the heat exchanger is determined by a series of parametric studies on the desorber and absorber. The length of the tubes is varied from 0.12 m to 0.30 m, and the equilibrium absorber solution outlet temperature is varied between 35°C and 45°C. The heat transfer fluid flow rates are maintained at baseline operating conditions during these parametric studies to ensure that they remain within the capabilities of the test stand.

The required heat transfer fluid inlet temperature for the desorber and absorber with LiBr as the absorbent as a function of the active length and absorber temperature is shown in Figure 3.5. As the length of the tubes increases, the difference between the heat transfer fluid inlet temperature and the solution outlet temperature decreases. The reason for this can be seen by examining the factors influencing heat transfer in the falling film.

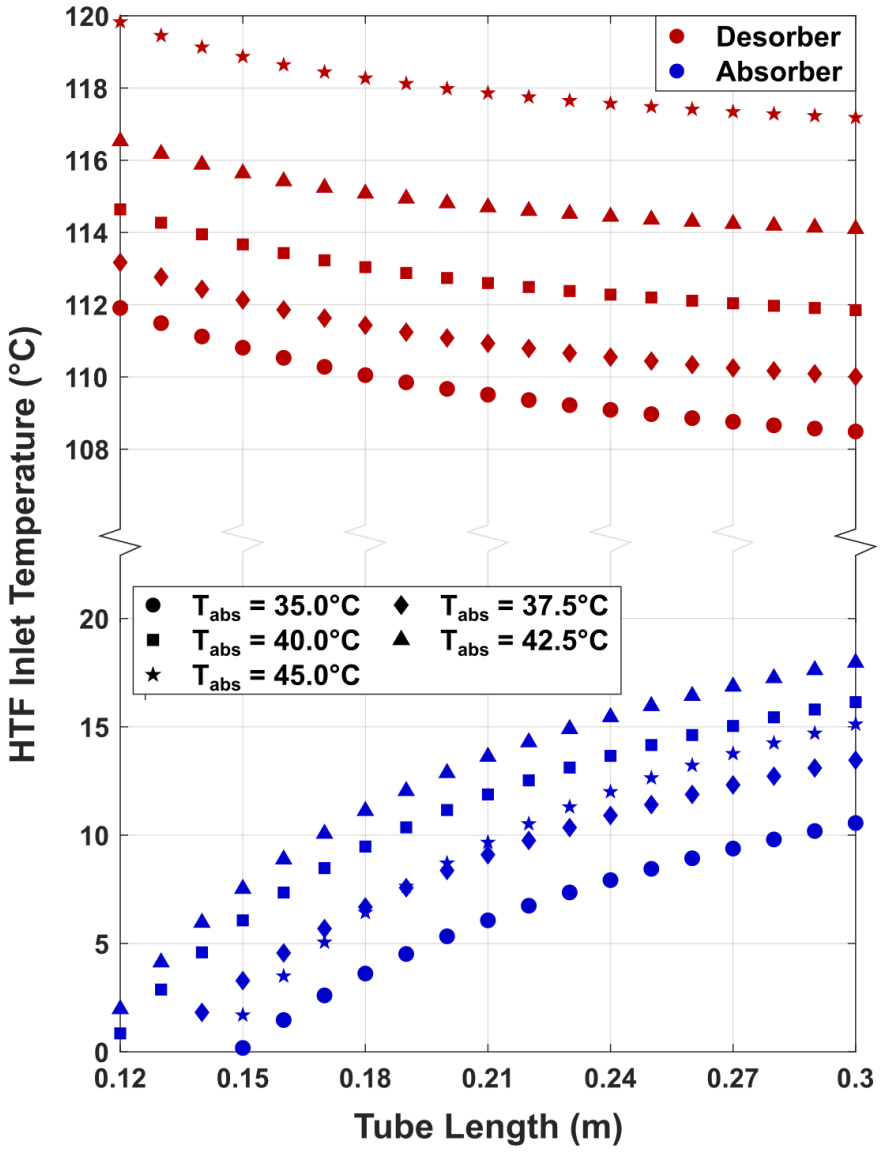

Figure 3.5: Heat transfer fluid inlet temperature as a function of tube length and absorber temperature

The heat transfer rate between the wall and the solution is given by Equation 3.15.

The heat transfer coefficient in the desorber depends on the Reynolds number as

$$\alpha_{\ell,i} \propto Re_{\ell,i}^{0.85} \tag{3.21}$$

where the Reynolds number is directly proportional to Γ, the mass flow rate per unit length of tube (Hu and Jacobi, 1996b). Thus, as the tube length increases,

$$\alpha_{\ell,i} A_o \propto \left(\frac{1}{L}\right)^{0.85} L = L^{0.15} \tag{3.22}$$

The results for the absorber follow the same pattern, but with an exponent of 0.688 on the Reynolds number (Park et al., 2003). Therefore, for a longer tube, the temperature difference between the wall and the solution must be smaller to achieve the same amount of heat transfer, and the heat transfer fluid inlet temperature approaches the solution inlet temperature. Although the heat transfer fluid flow rate is held constant in these simulations, if the flow rate were to be increased, the heat transfer fluid inlet temperature would be higher for the absorber and lower for the desorber because the same heat transfer could be achieved with a lower temperature difference.

As the absorber solution outlet temperature increases, the absorbent concentration difference between the strong and weak solutions decreases. Thus, to generate the same amount of vapor, the solution mass flow rate must increase. The increase in mass flow rate increases the Reynolds number and consequently the solution heat transfer coefficient. If the heat transfer resistance due to convection from the tube wall to the solution is dominant, increasing the solution heat transfer coefficient causes a substantial increase in the overall heat transfer coefficient and thus, a decrease in the temperature difference between the heat transfer fluid and solution. This is the controlling factor in the absorber. In contrast, a higher solution flow rate requires a higher heat duty for sensible heat transfer, which requires a larger temperature difference for a given geometry. This factor is more important for the desorber, which is why the desorber heat transfer fluid inlet temperature increases with increasing absorber temperature. For the absorber, at the highest absorber solution

equilibrium outlet temperature tested, a lower heat transfer fluid inlet temperature is required. As the solution flow rate increases and the concentration swing decreases, the absorber inlet temperature increases. When the absorber solution inlet temperature increases sufficiently, it enters the absorber in a superheated state. It then cools to saturation conditions by both rejecting heat to the heat transfer fluid and by desorbing a small amount of vapor. However, this desorbed vapor must be absorbed later in the absorber once the solution cools sufficiently, resulting in a higher heat transfer rate overall. This results in the lower heat transfer fluid inlet temperature seen in the model.

Based on the results of the parametric studies, a tube length of 0.24 m is selected. With an absorber outlet temperature of 37.5°C, this allows the absorber to operate with a heat transfer fluid inlet temperature of 10.9°C and the desorber to operate with a heat transfer fluid inlet temperature of 110.6°C, both of which are readily achievable under the cycle model conditions. If a higher absorber heat transfer fluid inlet temperature is desired, it can be operated at 40°C with an absorber heat transfer fluid inlet temperature of 13.7°C and a desorber heat transfer fluid inlet temperature of 112.3°C.

With the tube length determined, the design model for the desorber is simulated with an absorber temperature of 37.5°C to determine the thermodynamic properties of the solution and heat transfer fluid during the desorption process. The average temperatures of the solution, tube wall, and heat transfer fluid for each tube row are presented in Figure 3.6. As expected from the design of the heat exchanger, the temperature of the solution increases monotonically as its absorbent concentration increases as it drips from tube to tube. When the solution enters, it is subcooled; thus, it increases in temperature rapidly until it reaches saturation. The heat transfer fluid enters at the bottom of the heat exchanger

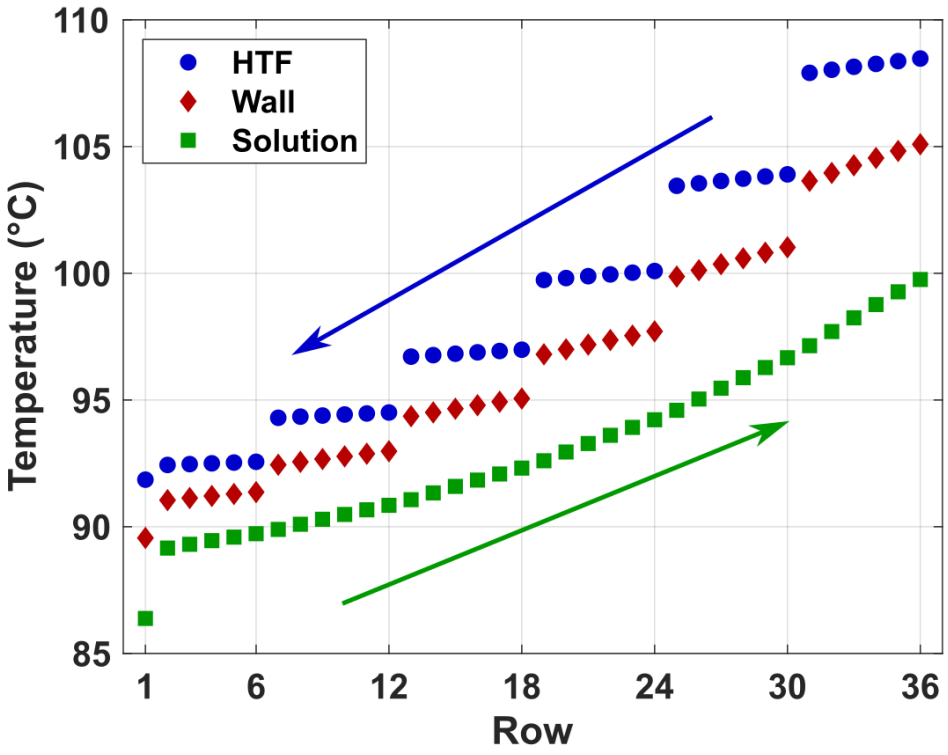

Figure 3.6: Temperatures within desorber at each row (arrows show flow direction)

and decreases in temperature as it flows upwards. The six passes for the heat transfer fluid are clearly seen from the jumps in the heat transfer fluid temperature and the wall temperature at rows 6, 12, 18, 24, and 30.

The temperature difference between the solution and the tube wall increases as the solution flows through the heat exchanger. However, it is expected that this is not a problem, as an investigation by Kim and Kim (1999) showed no nucleate boiling at a temperature difference between the wall and the solution of less than 10 K.

The absorber is simulated using the same geometry as the desorber and an absorber solution outlet temperature of 37.5°C. The averages temperatures of the heat transfer fluid, tube wall, and LiBr solution for each row of tubes are shown in Figure 3.7. As with the desorber, the solution and heat transfer fluid are in counter flow.

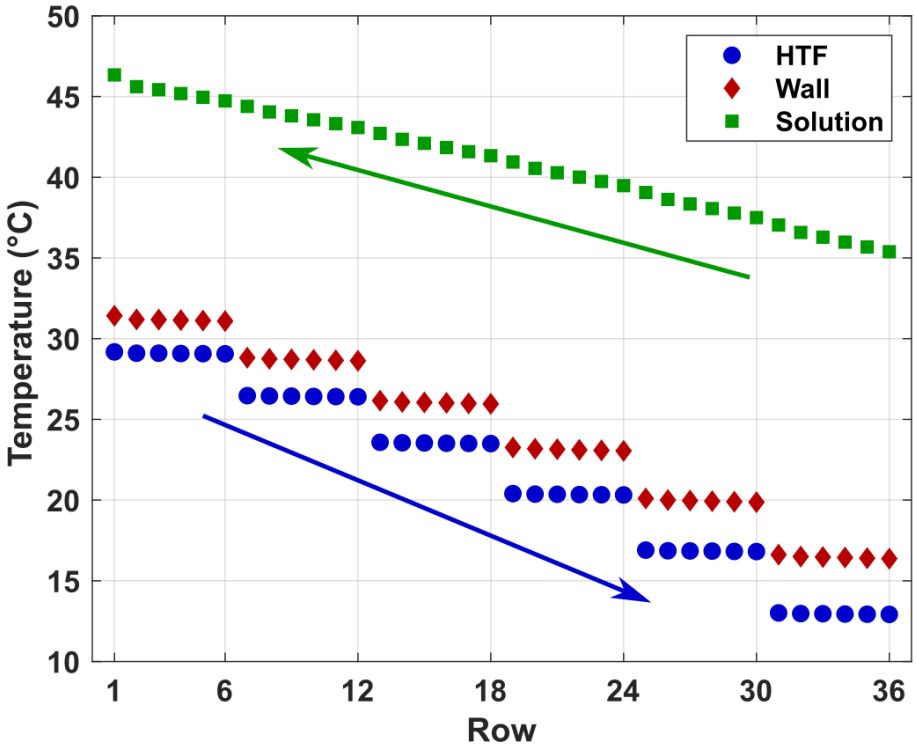

Figure 3.7: Temperatures within absorber at each row (arrows show flow direction)

When the solution enters the absorber, it is subcooled by 0.1°C; thus, absorption can begin immediately. The temperature difference between the solution and the wall is much larger for the absorber than it is for the desorber. This is because the convective heat transfer coefficient in the absorber is a factor of 5 lower than that in the desorber as shown in Table 3.3. As the LiBr solution cools, its viscosity increases, which reduces the Reynolds number. In addition, the exponent on the Reynolds number for absorption is 0.688 (Park et al., 2003; Olbricht and Luke, 2019), indicating that even if the same Reynolds number is used, the absorption heat transfer rate is lower.

3.5 Solution Distributor Design

To establish the falling film on the first row of the falling-film heat exchanger, a solution distributor was designed. A drip-tube design was selected based on the low flow rate required and on work by Bustamante and Garimella (2019) that showed minimal maldistribution for a drip-tube design over a large Reynolds number range. In such a design, liquid solution pools in a header with small-diameter tubes mounted at the bottom of the header. Flow through the tubes is driven by gravity. The minimum depth of liquid in the header required to initiate flow through the tubes can be determined by a hydrostatic analysis.

Consider the hemispherical droplet suspended from the inner diameter of a tube with a liquid pool above it as shown in Figure 3.8. When the situation is in hydrostatic

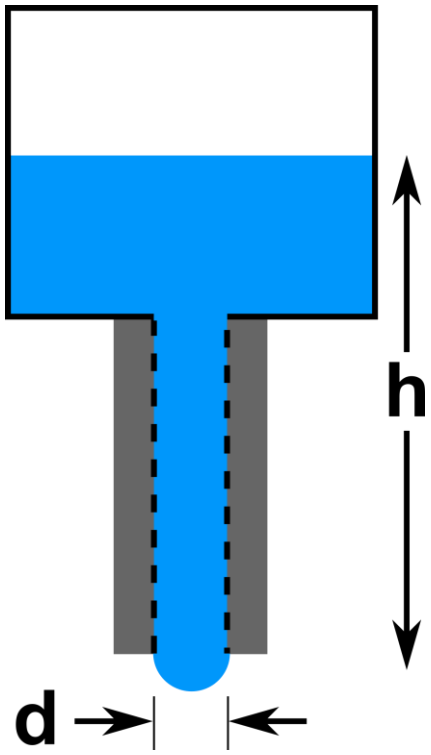

Figure 3.8: Hydrostatic analysis of drip tube

Table 3.4: Hydrostatic head required to initiate flow for various tube IDs

Tube ID (mm)	Hydrostatic Head (mm)
0.56	37.0
1.37	15.1
1.75	11.8
2.16	9.6

equilibrium, the force exerted by the water above the droplet is equal to the surface tension force holding the droplet to the wall of the tube. Solving this force balance for the height of the liquid column indicates the pool height at which flow will begin.

$$h = \frac{4\sigma}{\rho g d} \tag{3.23}$$

where σ is the surface tension of the liquid and h is the liquid column height. Using a surface tension of 0.085 N m^{-1} and a density of 1675 kg m^{-3}, which are representative values for LiBr, the pool height for different commercially available tube inner diameters can be determined. These are given in Table 3.4. The results of this calculation suggest that a tube inner diameter greater than 1.37 mm will begin dripping for a sufficiently small hydrostatic head.

To verify that the 1.37-mm ID tubes would work in the heat exchanger, a series of tests were conducted using a mock header with five tubes. A 50 vol% solution of ethylene glycol in water was used for the test to match the ratio of surface tension to density of LiBr at test conditions. The results of these initial tests showed that once flow started through some of the tubes in the header, the flow rate through them was sufficiently high to prevent flow from starting in other tubes in the header. To mitigate this, stainless steel wire with a diameter of 1.02 mm was inserted into the tubes. These wires reduced the flow area, which decreased the velocity of the liquid flowing through the tubes and allowed all tubes in the

header to demonstrate flow. Consequently, 1.02-mm diameter wires were inserted into the drip tubes of the solution distributor for the absorber and desorber used for the proof-of-concept of the water-purifying absorption heat pump to improve the hydrodynamic performance.

3.6 Conclusion

Design models for horizontal-tube, falling-film heat and mass exchangers are developed to enable their fabrication and the demonstration of the hybrid absorption heat pump cycle discussed in Chapter 2. Consideration is given to the possibility of droplet entrainment, and it is concluded that for typical geometries, it is unlikely that droplets will be entrained. Furthermore, simulation of the desorber indicates that nucleate boiling is unlikely, removing one of the two major paths by which droplet entrainment can occur.

Table 3.5: Final heat exchanger geometry and operating conditions

Parameter	**Absorber**	**Desorber**
Solution Flow Rate	88.9 g min^{-1}	96.1 g min^{-1}
Solution Inlet Temperature	47.0°C	83.7°C
Solution Inlet Concentration	57.0 wt% LiBr	61.7 wt% LiBr
HTF Flow Rate	270 g min^{-1}	279 g min^{-1}
HTF Inlet Temperature	14.4°C	110.7°C
System Pressure	0.87 kPa	12.3 kPa
Tube Columns	2	
Tube Rows	36	
HTF Passes	6	
Rows per Pass	6	
Tube Diameter	3.175 mm	
Tube Wall Thickness	0.51 mm	
Tube Length	0.24 m	
Row Spacing	6.35 mm	
Drip Tubes per Column	39	
Drip Tube Spacing	6.35 mm	
Drip Tube Inner Diameter	13.37 mm	
Solution Inlet Header Height	25.4 mm	

The design models are simulated for the absorber and desorber, and a tube length that allows operation of a heat exchanger in either mode is selected. A drip-tube solution distributor is designed to initiate the falling film on the first row of tubes. Simple experiments were conducted to ensure adequate performance of the distributor. The final geometry and operating conditions of the absorber and desorber are given in Table 3.5.

CHAPTER 4. EXPERIMENTAL DEMONSTRATION

In the previous chapters of this work, a novel, water-purifying absorption heat pump cycle was developed and its potential to provide more utility with the same energy was shown thermodynamically. A falling-film, liquid-coupled heat exchanger that can serve as either the absorber or the desorber for the cycle was designed and modeled. In this chapter, the experiments conducted to determine the water purification capabilities of the cycle and to validate the performance of the falling-film heat exchanger are discussed.

The experiments conducted in this study demonstrate the water purification and cooling capabilities of the cycle in a batchwise manner. The water-purifying absorption heat pump cycle can be thought of as two processes that occur sequentially. In the first process, which occurs at low pressure, water vapor is evaporated from the feed solution at a temperature lower than the ambient and is subsequently absorbed into LiBr solution. In the second process, which occurs at high pressure, water vapor is desorbed from LiBr solution and condensed. The condensate resulting from the second process is the purified water produced by the cycle. By performing a series of experiments in which the low-pressure process and the high-pressure process are executed serially, it can be shown that water purification and cooling can both be achieved in the cycle.

Different components are used for the batchwise experiments than are used for the complete cycle, as shown in Figure 4.1. In the batchwise experiments, there are only two heat exchangers, one that acts as the evaporator or condenser and one that acts as the absorber or desorber. A pump is used to drive solution flow from a supply reservoir, through the absorber or desorber, and to a receiving reservoir. In contrast, there are five

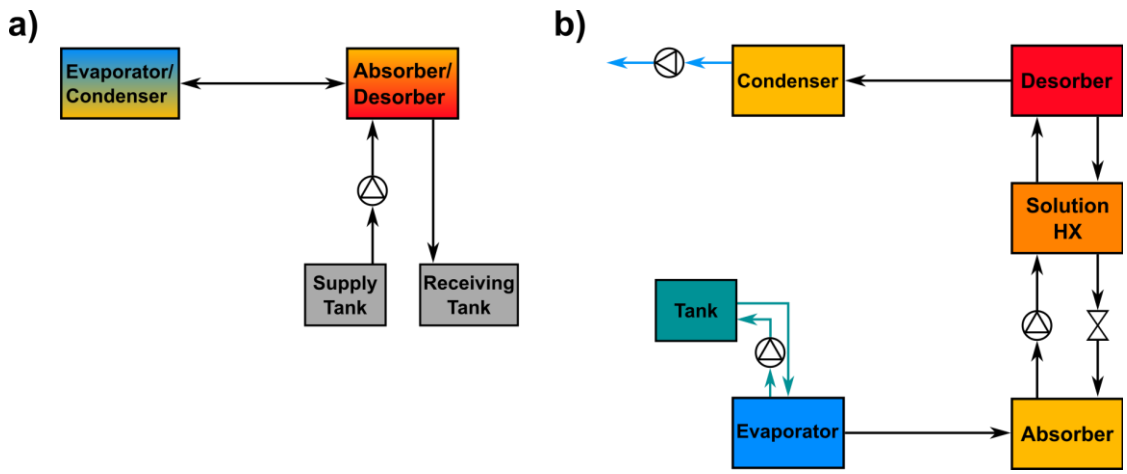

Figure 4.1: Test stand components for a) batchwise experiments and b) cycle experiments. Pumps and flow conditioning equipment for heat transfer fluid are not shown

heat exchangers in the complete cycle, including a recuperative solution heat exchanger that recovers energy from the concentrated solution leaving the desorber. Because of these differences, it is not possible to characterize the batchwise experiments using the figures

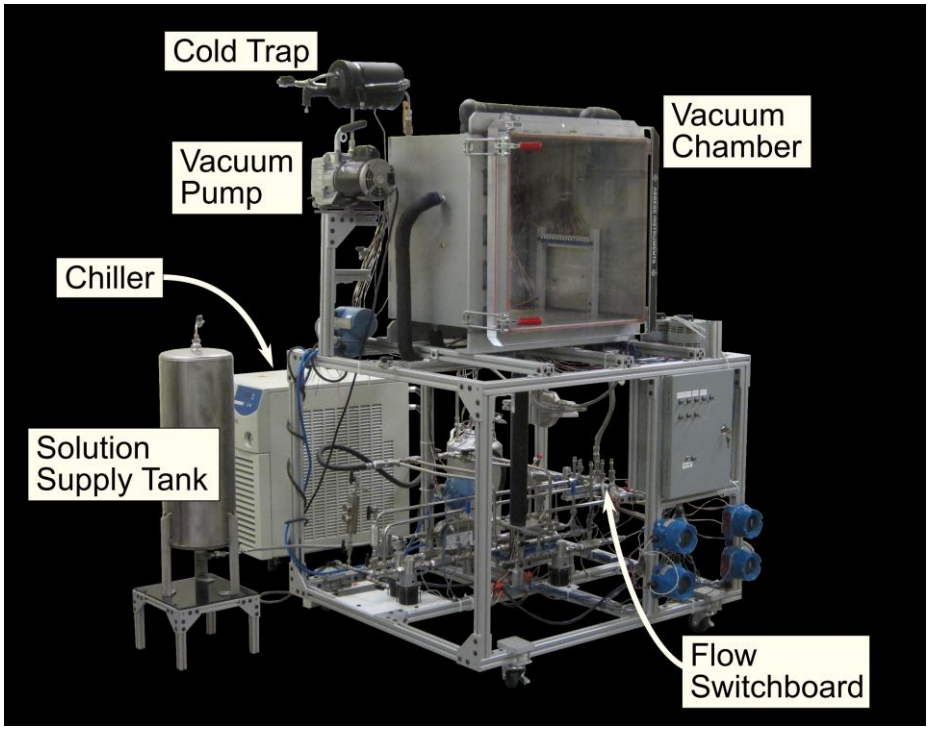

Figure 4.2: Vacuum chamber test stand

of merit defined in Chapter 2. Nevertheless, one can consider the low-pressure and high-pressure processes as the two halves of the cycle. By performing a series of experiments in which the low-pressure process and the high-pressure process are executed serially, it can be shown that water purification and cooling can be achieved using absorption heat pump components.

4.1 Test Stand Description

The vacuum chamber test stand used for the batchwise experiments conducted in this work is shown in Figure 4.2. A schematic of the test stand is shown in Figure 4.3. The test stand is built around an aluminum (6061-T6) vacuum chamber (Abbess Systems, S/N 50332) with an internal volume of 0.227 m^3. The vacuum chamber has 21 ports (shown schematically in Figure 4.4), six of which can be used as passthroughs for wires (B1-B6),

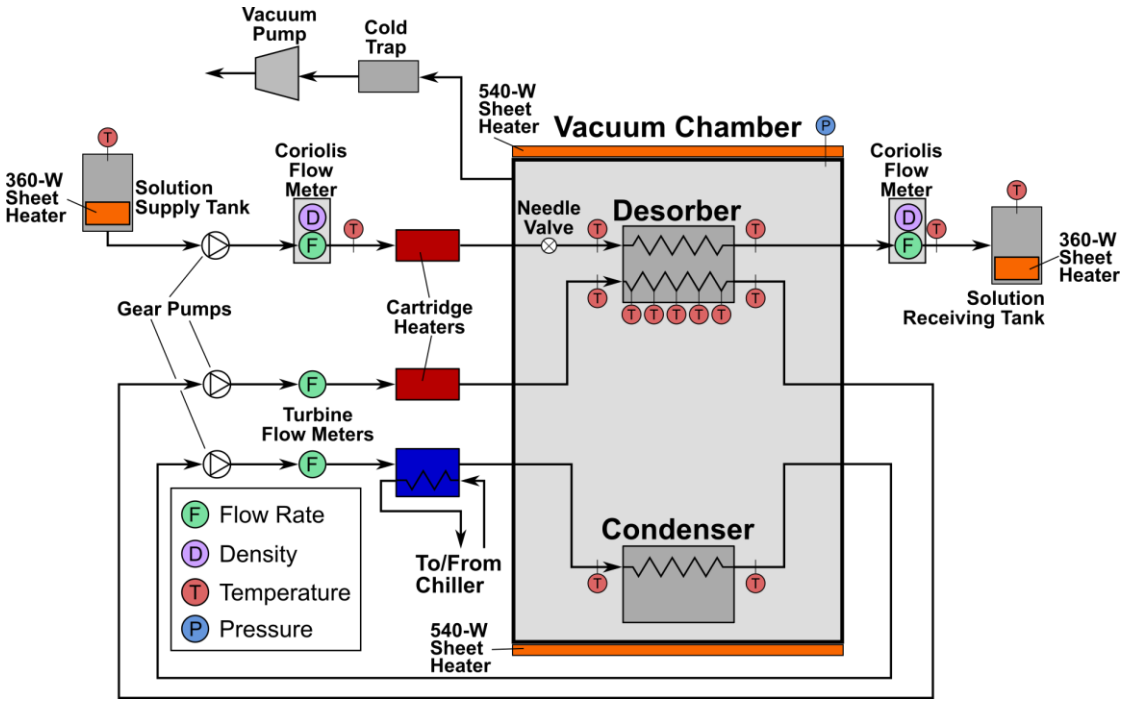

Figure 4.3: Vacuum chamber test stand schematic

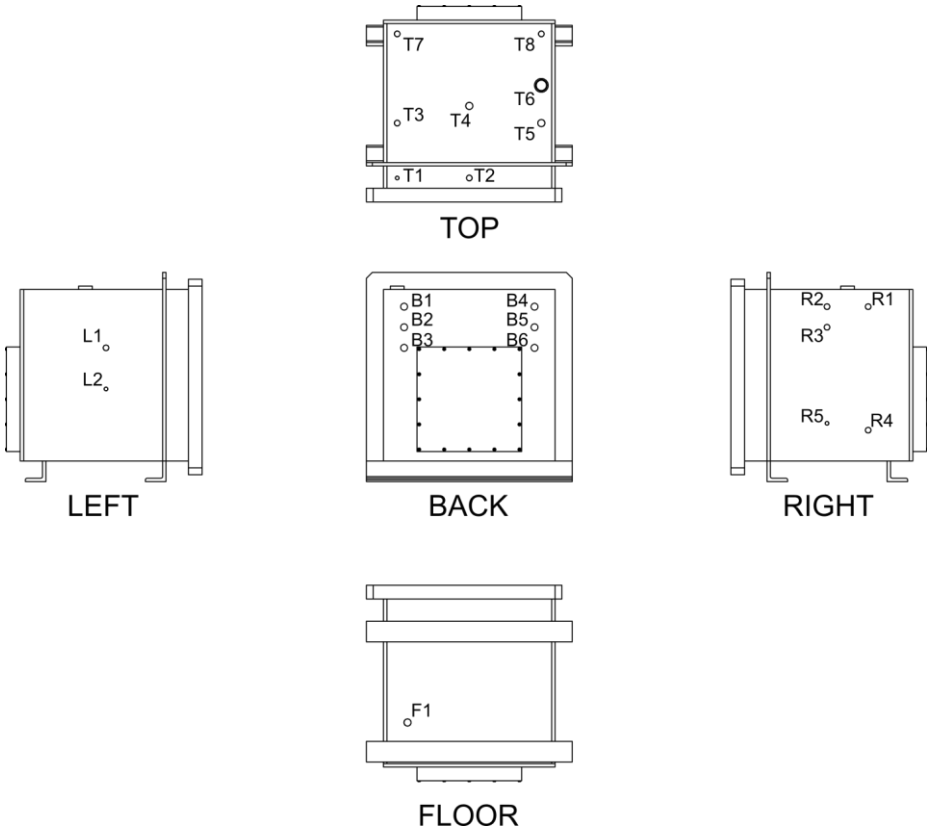

Figure 4.4: Vacuum chamber ports

and 15 of which can be used for fluid connections. Of the wire passthrough ports, five are in use: three of them admit nine strands of type-T thermocouple extension wire apiece (PAVE Technology P/N 1650), while two admit 12 strands of 18-gauge wire apiece (PAVE Technology P/N 1649).

Eleven of the fluid connection ports are in use on the chamber. Port T7 is connected to a cold trap, which is further connected to a vacuum pump (JB, Model DV-142N). Port T8 is connected to a digital pressure gauge (OMEGA Model PX409; Range: 0-34.5 kPa; Uncertainty: ±0.08% of reading). Port T1 is connected to an analog vacuum gauge (Range: 0-760 mmHg vacuum). Ports R1-R4, L1, F1, T3, and T5 have custom fittings installed that allow compression fittings to be connected inside and outside the chamber. On the outside

of the chamber, tubing from these eight ports is routed to the chamber side of the flow switchboard.

The flow switchboard is used to connect components for flow conditioning (e.g., pumps and heat exchangers) to the chamber in an easily reconfigurable manner. It consists of two sets of eight female compression fittings arranged in a square parallel to the floor and separated by ~40 cm. The flow-conditioning side of the flow switchboard is located directly below the chamber side. Flexible hose (12.7 mm inner diameter, 45 cm long) can be used to make connections between the flow-conditioning side and the chamber side of the switchboard. Three fluid lines are used for the experiments in this work. The first is a once-through fluid line that is used for the LiBr solution. The solution supply tank is connected to a gear pump (Fluid-O-Tech MG304XD0PE00000 with a 4322 016 58013H motor) such that the pump is flooded by gravity. The pump drives flow through a Coriolis flow meter (MicroMotion CMFS010M; Range: 0-110 kg h^{-1}, 0-5000 kg m^{-3}; Uncertainty: ±0.1% of reading, ±2 kg m^{-3}) for flow and density measurement. A 1-kW Watlow cartridge heater is used to preheat the solution before it reaches the flow switchboard, and a needle valve is installed just upstream of the solution header of the falling-film heat exchanger to prevent flashing in the solution line. Solution flow exits the chamber and is routed through another Coriolis flow meter (MicroMotion CMFS010M) and to a receiving tank. To prevent crystallization of the LiBr solution during testing, both tanks are maintained at elevated temperature using 360-W silicone sheet heaters, and the Coriolis flow meter closest to the solution supply tank is wrapped with a tape heater and maintained at a temperature of 37°C. The solution receiving tank with the installed silicone sheet heater is shown in Figure 4.5.

Figure 4.5: Solution receiving tank (insulation pulled back to show heater)

A second fluid line is used in a closed-loop configuration to chill the heat transfer fluid routed to the absorber or evaporator. This loop uses a gear pump (Fluid-O-Tech MG304XD0PE00000 with a 4322 016 58013H motor) to drive flow of water pressurized to 3 bar gauge through a turbine flow meter (FTI FTO-1-NIXW-LHC-1; Range: 3.8-303 mL min^{-1} water; Uncertainty: ±0.1% of reading). The flow then passes through a shell-and-tube heat exchanger (Exergy 00540-05), where it exchanges heat with a stream of 50 vol% propylene glycol-water solution maintained at a specified temperature by a portable chiller (Thermo Fisher Scientific Merlin M150) before entering the flow switchboard to be routed to the vacuum chamber.

The third fluid line is used in a closed-loop configuration to heat the heat transfer fluid routed to the evaporator or desorber. A gear pump (Fluid-O-Tech MG304XD0PE00000 with a 4322 016 58013H motor) drives flow of water pressurized to 3 bar gauge through a turbine flow meter (FTI FTO-1-NIXW-LHC-1) and a section heated by a 1-kW Watlow cartridge heater before entering the flow switchboard to be routed to the vacuum chamber.

Silicone sheet heaters (540 W) are applied to the chamber at the back 15 cm of the top and the front 15 cm of the bottom to raise the temperature of the chamber walls above the saturation temperature of water vapor at the chamber pressure during experiments. Fiberglass insulation (50.8 mm thick, k = 0.03 W m^{-1} K^{-1}) is applied to the outside of the

Figure 4.6: Falling-film heat exchanger installed in vacuum chamber

chamber to reduce heat losses. All fluid lines are covered with polyurethane insulation (12.7 mm ID, 19.0 mm thick, $k = 0.02$ W m^{-1} K^{-1}) outside the chamber and ceramic insulation (12.7 mm thick, $k = 0.03$ W m^{-1} K^{-1}) inside the chamber. A vapor generator consisting of a tank and a tape heater (HTS/Amptek AWH-051-040D, 312 W) is connected to the chamber through the flow switchboard to pressurize the chamber after evacuation for the high-pressure tests.

The falling-film heat exchanger designed in Section 3.3 is installed in the vacuum chamber, as shown in Figure 4.6. Pressurized water acts as the coupling fluid, entering the heat exchanger through the insulated tubing on the lower left of the photo and exiting through the insulated tubing on the upper left. LiBr solution flows into the distributor through the needle valve at the top of the photo. A close-up view of the distributor is shown in Figure 4.7. The solution then drips onto the horizontal tubes and flows down until it reaches the lower header. The solution exits the lower header through the tubing at the lower right of the photo.

A second heat exchanger is installed in the vacuum chamber, as shown in Figure 4.8, to act as a condenser when the falling-film heat exchanger is operating as a desorber, and an evaporator when the falling-film heat exchanger is operating as an absorber. This heat exchanger is a three-pass heat exchanger with 1.6-mm outer diameter tubes. The bucket surrounding the heat exchanger acts as a reservoir to contain the condensate when

Figure 4.7: Falling-film heat exchanger distributor

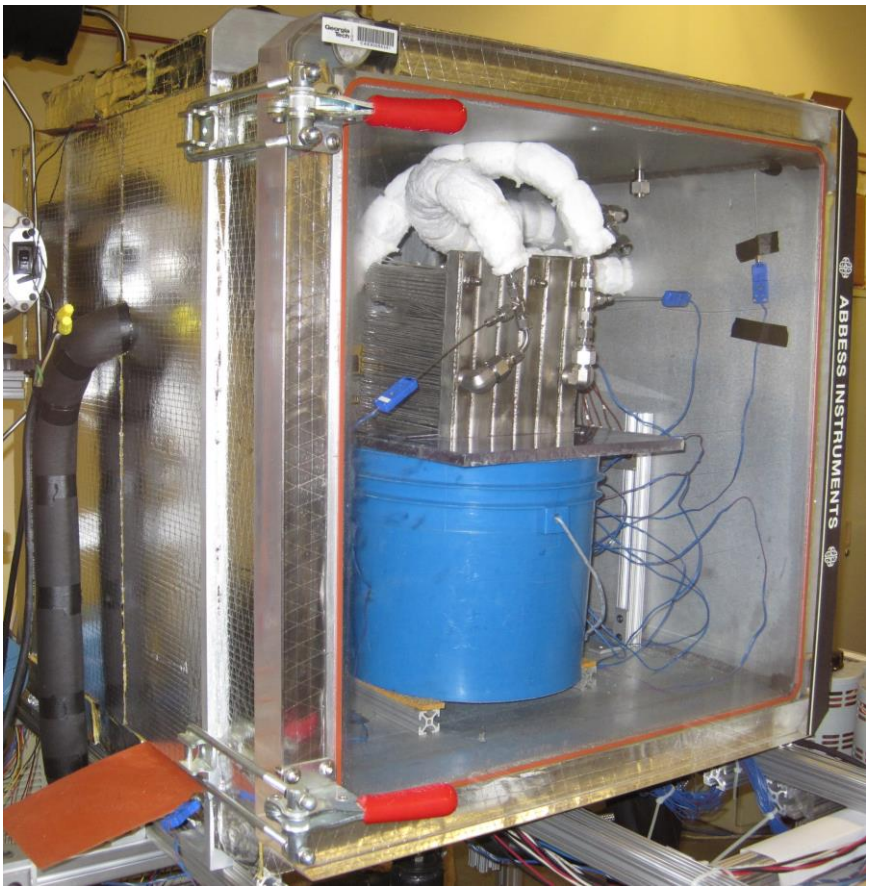

Figure 4.8: Condenser or evaporator installed in vacuum chamber

this heat exchanger acts as a condenser. When this heat exchanger acts as an evaporator, the bucket is filled with the feed to be purified and covered to prevent droplets from being ejected by bubbles bursting at the surface.

The vacuum chamber, heat exchangers, and fluid lines are instrumented with calibrated, type-T thermocouples (Uncertainty: ±0.25°C) that are used to monitor the temperature of the vacuum chamber, the LiBr solution upstream of the chamber inlet and in the headers of the falling-film heat exchanger, the heat transfer fluid in the falling-film heat exchanger at the inlet, outlet, and the internal headers, the heat transfer fluid in the secondary heat exchanger, and the heat transfer fluid in the flow conditioning section of

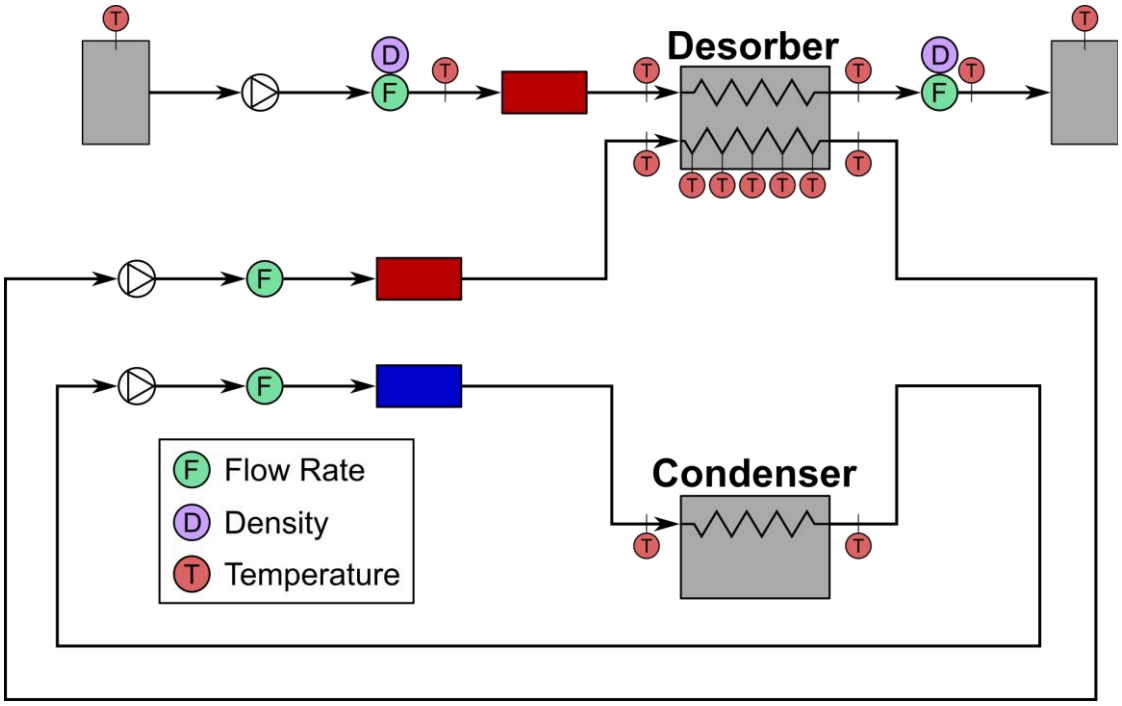

Figure 4.9: Flow paths and measurements during high-pressure test

both loops. Figure 4.9 shows a schematic of the fluid loops on the test stand when the falling-film heat exchanger is acting as a desorber with the measurements shown at the relevant locations. All instruments used for data collection are connected to a data acquisition system (NI cDAQ-9174), which transmits the data to a computer system running LabVIEW software.

The solution used in the experiments was prepared as a 61.7 wt% LiBr solution using distilled water from the lab distiller (Running Waters, Inc. A15) and anhydrous LiBr (Sigma Aldrich, ≥99%). 6.0 kg of LiBr were used in the solution, resulting in an initial solution mass of 9.7 kg. Anhydrous LiOH (Sigma Aldrich, ≥98%) was added to the resulting solution to a concentration of 0.1 M as a corrosion inhibitor (Guiñon et al., 1994).

4.1.1 Lithium Bromide Solution Concentration Calculation

The concentration of the LiBr solution used in the test can be determined from the density measurements taken by the Coriolis flow meters and the nearby temperature measurements. The density of a LiBr solution as a function of concentration and pressure can be calculated using the Gibbs free energy potential of aqueous LiBr determined by Yuan and Herold (2005).

$$\frac{1}{\rho} = V_0 + V_1 w + V_2 w^2 + V_3 T + V_4 wT + V_5 w^2 T + V_6 T^2 + V_7 wT^2 \qquad (4.1)$$

Here, the concentration is in wt% LiBr, while the temperature is in K. Values of the constants V_i can be found in the aforementioned paper. Rearranging Equation 4. yields a quadratic equation in concentration

$$0 = \left(V_0 + V_3 T + V_6 T^2 - \frac{1}{\rho}\right) + (V_1 + V_4 T + V_7 T^2) w + (V_2 + V_5 T) w^2 \qquad (4.2)$$

which can be solved by taking the negative root provided by the quadratic formula.

4.2 Vacuum Test Procedure

To ensure that the results of the component tests reflect the behavior of the components in an actual system, it is important that rate of pressure rise of the vacuum chamber test stand due to air ingress is less than 5 μmHg min^{-1} (40 Pa h^{-1}). This restricts the pressure rise in the chamber during a typical 90-minute test to less than 60 Pa. To quantify the leak rate of the test stand, a vacuum test can be conducted as follows.

With all valves open between the solution tanks and the vacuum chamber and the vapor generator and the vacuum chamber, the vacuum pump is used to decrease the pressure in the chamber until it reaches a pressure substantially below atmospheric pressure

but above the saturation pressure of any volatile species contained in the test stand. In the vacuum tests run for this set of experiments, a pressure of 12.1 kPa or 6.9 kPa was typically used. A pressure of 12.1 kPa was used for the standalone vacuum tests conducted prior to the start of the experimental studies, while a pressure of 6.9 kPa was used as part of the degassing procedure during the low-pressure experiments as discussed below. Once the target pressure is reached, the vacuum pump is deactivated, and the valve between the vacuum pump and the chamber is closed. LabVIEW software is used to monitor the pressure of the chamber as a function of time for 16 hours or more. This allows for the solution tanks and vacuum chamber to reach mechanical equilibrium and for air dissolved in any liquids in the test stand to equilibrate with the gas phase.

Figure 4.10 shows the pressure profiles for the test stand during a successful test (Figure 4.10a) and during a test with a leak in the test stand (Figure 4.10b). The rapid pressure rise at the beginning of the successful test is due to pressure equalizing between the tanks and the chamber, followed by degassing of liquids contained in the test stand. After ~10 hours, degassing has concluded, and the pressure begins to rise more slowly. In the test shown in Figure 4.10a, the leak rate is 2.7 μmHg min^{-1}. In contrast to this pattern

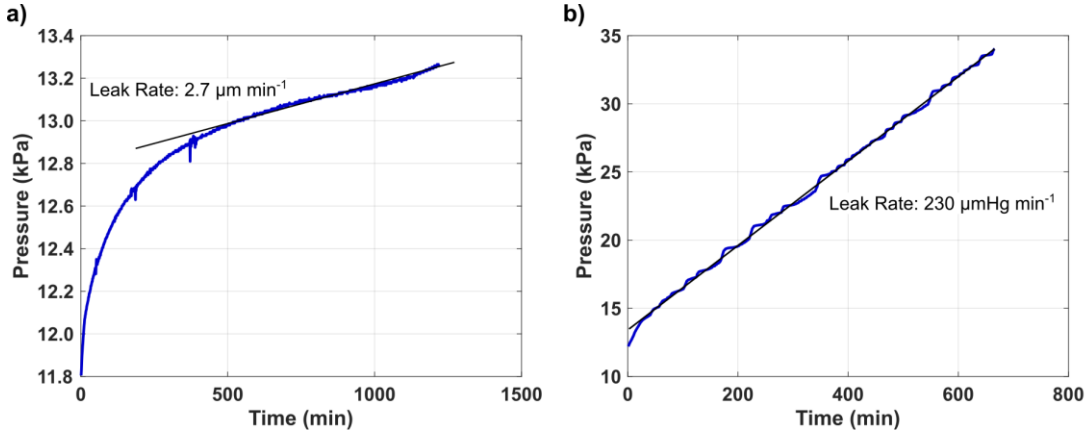

Figure 4.10: Pressure profiles for (a) successful and (b) failed vacuum tests. Error bars have been omitted to improve readability

of a rapid rise followed by a slow, linear increase, the failed test shows a rapid linear increase to the limit of the pressure transducer and a leak rate that exceeds the acceptable leak rate by two orders of magnitude.

4.3 Experimental Procedures

The test stand used for demonstration of the water-purifying absorption heat pump operates in a batchwise manner; therefore, test procedures differ slightly for high-pressure operation (desorber and condenser) and low-pressure operation (evaporator and absorber).

4.3.1 Low-Pressure Test

Demonstration of water purification and cooling using absorption heat pump components begins by operating the falling-film heat exchanger as an absorber and the other heat exchanger as an evaporator. For this test, the heated water loop is connected to

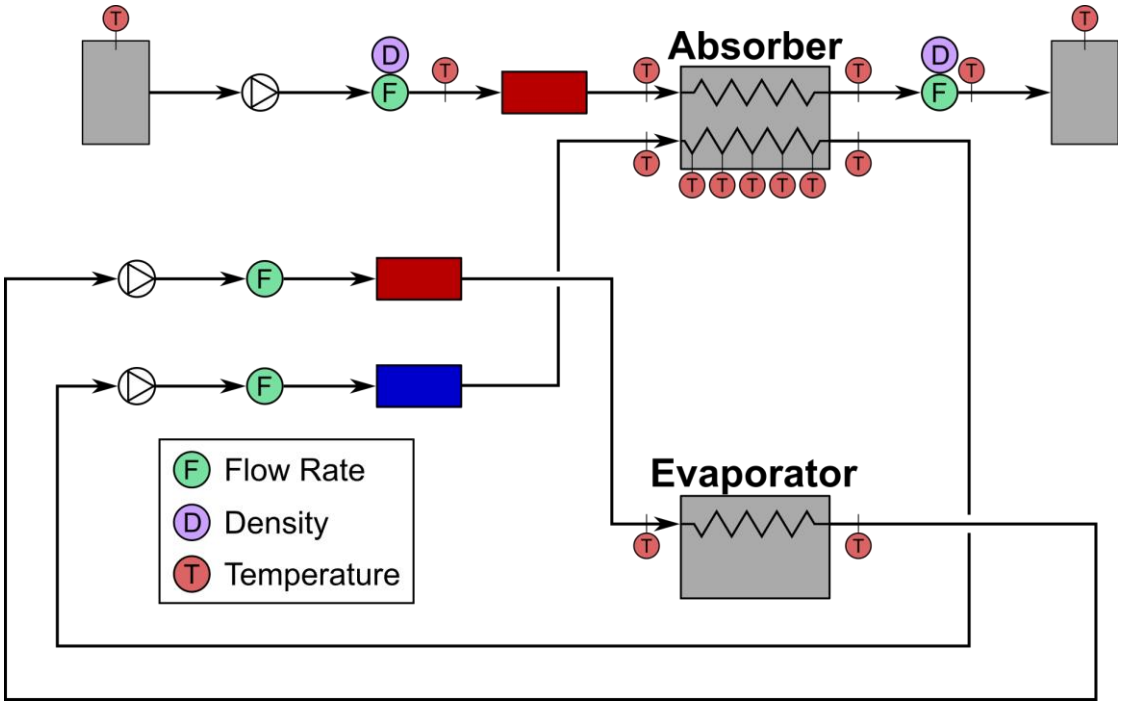

Figure 4.11: Flow paths and measurements during low-pressure test

the evaporator through the flow switchboard, and the cooled water loop is connected to the absorber as shown in Figure 4.11. The bucket surrounding the evaporator is filled with the feed solution to be purified and covered to prevent ejection of droplets during pool boiling. In some of the experiments, the feed solution was chilled to a temperature of ~1°C prior to the start of air removal to allow for a more rapid evacuation.

To begin the test, air is removed from the chamber. In a subset of the tests, the chamber is depressurized to an absolute pressure of 6.9 kPa, and that pressure is maintained for 36 hours to degas the feedwater and LiBr solution in the test stand. After degassing, or initially for experiments without the 36-hour hold at vacuum conditions, the cold trap is initialized by turning on the chiller connected to it. The set point of the chiller is -12°C. Once the chiller temperature reaches -10°C, 10 minutes are allowed to pass, which precools the cold trap. Following this, the vacuum pump is turned on, and the valve between the vacuum pump and the chamber is opened. The vacuum pump is run until the pressure in the chamber reaches 1.24 kPa.

Once evacuation has been completed, the low-pressure performance of the water-purifying absorption heat pump can be studied. Flow of LiBr solution is started, along with the flow of the heat transfer fluid in the falling-film heat exchanger. The solution flowing over the absorber absorbs water from the vapor phase, which results in the chamber pressure dropping. As the pressure in the chamber continues to decrease, flow of the coupling fluid through the evaporator is started, along with the heater in that loop. The power level of the heater for the evaporator coupling fluid is modulated until steady state is reached at the target operating conditions. Typically, steady state was reached 30-40 minutes after the start of the test. During steady-state operation, 25 samples are captured

from each of the sensors connected to the data acquisition device at a rate of 100 Hz and written to file at 10-second intervals.

4.3.2 High-Pressure Test

Following completion of a low-pressure test, the solution is returned from the receiving tank to the supply tank. Additionally, the coupling fluid loops are reconfigured through the flow switchboard as shown in Figure 4.9 such that the heated water is routed to the falling-film heat exchanger, acting as a desorber, and the cooled water is routed to the other heat exchanger, which acts as a condenser. Because the saturation temperature of the vapor in the chamber during the high-pressure test exceeds the ambient temperature, the sheet heaters on the chamber are turned on and the temperature of the chamber walls is raised until they exceed the saturation temperature at the target chamber pressure. The heating process is conducted overnight prior to evacuating the chamber. Once pressurization begins, as discussed below, the walls of the chamber are heated at a rate of up to 5°C h^{-1} until the target temperature is reached.

A similar procedure for evacuating the chamber is used for the high-pressure tests. However, the performance of the desorber is insensitive to the presence of noncondensable gases in the system. Therefore, the pressure of the chamber is maintained at 6.9 kPa for only 12 hours prior to full evacuation. Furthermore, the lack of water in the chamber at the start of the desorber test allows the chamber to be depressurized to a pressure 1 kPa or less. Following evacuation, the chamber pressure must be increased to the target operating pressure. Thus, the vapor generator connected to the chamber is used to pressurize the chamber with water vapor. Simultaneously, the temperatures of the solution supply and

receiving tanks are raised to reduce their potential to absorb water vapor from the chamber. Additionally, the coupling fluid flowing through the desorber is preheated to an inlet temperature near 80°C and the temperature of the chiller used to control the temperature of the condenser coupling fluid is raised to its set point.

Once these preparations have been completed, the flow of solution is started, and the temperature of the desorber coupling fluid is increased to its target value. The pressure of the chamber is controlled by varying the flow rate of the condenser heat transfer fluid. Data collection is started once steady state is reached. As with the low-pressure tests, achievement of steady state takes between 30 and 40 minutes.

4.3.3 Water Quality Measurements

The quality of the feedwater and the distillate produced by the water purification process is assessed using two metrics: electrical conductivity and total organic carbon (TOC). The electrical conductivity indicates the quantity of dissolved ions in the water and is measured using an OMEGA CDE-45P conductivity meter (Range: 0-2 S cm^{-1}; Uncertainty: ±0.3% span). Electrical conductivity is commonly used as a water quality metric (Hourlier et al., 2010) and has been used in the literature to determine the concentration of ionic species in a sample (Prieto et al., 2001; McCleskey et al., 2012) The measurement is conducted by immersing the electrode of the conductivity meter in a beaker containing the liquid to be measured. Five samples are taken, and the average of the samples is reported. After each test, the conductivity meter and the beaker containing the liquid are rinsed with DI water 3-4 times and air dried.

TOC is a measure of organic compounds in the sample and is particularly suited to greywater quality testing. TOC is measured using a Shimadzu TOC-L Analyzer. Prior to taking the measurements, calibration curves were generated using standard TOC and inorganic carbon (IC) solutions from Aqua Solutions. The TOC calibration curve was generated according to EPA 415.3 (Potter and Wimsatt, 2009), while the IC calibration curve was generated using the same concentrations as the TOC calibration curve.

4.4 Test Conditions

Three feedwater compositions were used in the experiments. Deionized water (DI water) was used to provide a baseline for heat transfer performance and to determine if there was any contamination of the distillate by the absorbent solution. Two impure feeds were also tested to determine the water purification performance of the system. Synthetic graywater, which is representative of the graywater discharged from a bathroom, was formulated following the composition of Hourlier et al. (2010). In these experiments, fecal coliforms were omitted from the graywater composition. The water quality of the graywater and the resulting distillate was measured using electrical conductivity and TOC. The second impure feed used was a 3.5 wt% NaCl solution, which is representative of the main component in seawater. No carbon was expected in this feed; thus, only electrical conductivity was used to analyze the water quality of the feed and the distillate.

The baseline conditions of the tests are based on the selected model operating conditions. As discussed in Section 3.4, an absorber outlet temperature of 37.5°C was selected. The target operating conditions for the low-pressure and high-pressure tests are shown in Table 4.1. Due to the batchwise nature of the tests and the interaction of LiBr

Table 4.1: Target system operating conditions

Parameter	Low-Pressure Test	High-Pressure Test
System Pressure	0.87 kPa (T_{sat} = 5°C)	12.3 kPa (T_{sat} = 50°C)
Solution Flow Rate	88.9 g min^{-1}	96.1 g min^{-1}
Solution Inlet Temperature	47.0°C	83.7°C
Solution Inlet Concentration	57.0 wt% LiBr	61.7 wt% LiBr
HTF Flow Rate	270 g min^{-1}	279 g min^{-1}
HTF Inlet Temperature	14.4°C	110.7°C

solution with the moisture in the air between tests, the target operating conditions could not be achieved simultaneously in all tests. Therefore, for the low-pressure tests, the solution and absorber heat transfer fluid flow rates and the set point on the absorber heat transfer fluid chiller were controlled in all tests. Furthermore, the solution inlet temperature was controlled to be close to the saturation temperature regardless of concentration. The evaporator heat transfer fluid flow rate and heater were varied to maintain the chamber at the target pressure. For the high-pressure tests, the solution and desorber coupling fluid flow rates were set to the target flow rates in all tests. A solution inlet temperature 3 K lower than the saturation temperature was targeted. A concentration change equal to that in the target operating conditions was assumed, and the desorber coupling fluid inlet temperature was set 10 K hotter than the saturation temperature of the solution leaving at the target pressure and with the target concentration change. The flow rate of the condenser heat transfer fluid was varied to maintain the chamber pressure.

Because the system pressure could be well-controlled, it was varied to explore the effects of operating conditions on system performance. Pressures above and below the

Table 4.2: Low-pressure and high-pressure operating conditions

	Low-Pressure Test	High-Pressure Test
Low System Pressure	0.76 kPa (T_{sat} = 3°C)	11.2 kPa (T_{sat} = 48°C)
High System Pressure	1.0 kPa (T_{sat} = 7°C)	13.6 kPa (T_{sat} = 52°C)

target operating conditions were considered with synthetic graywater as the feed. These pressures and their corresponding saturation temperatures for pure water are shown in Table 4.2.

4.5 Data Reduction

The water purification capabilities of the cycle can be determined by direct measurement of the water quality after a low-pressure test and a high-pressure test. However, to elucidate the thermal performance of the falling-film heat exchanger that serves as the desorber or absorber in these experiments, the raw data from the experiments must be analyzed.

4.5.1 Heat Transfer Fluid Heat Transfer Rate

The heat transfer rate in the falling-film heat exchanger is calculated in two ways. The first method examines the heat transfer rate from the heat transfer fluid flowing through the falling-film heat exchanger, which is given by

$$\dot{Q}_{f,HTF} = \dot{m}_{f,HTF} c_{p,w} \left(T_{f,HTF,in} - T_{f,HTF,out} \right) \tag{4.3}$$

The specific heat capacity of the water is evaluated at the average of the inlet and outlet temperatures. This heat transfer rate can include heat transferred to the falling film, heat lost to the water vapor in the chamber through convection, and heat transferred to the chamber walls through radiation. In the analyses that follow, a worst-case set of conditions in the high-pressure experiments is assumed. During the low-pressure experiments, temperature differences between the heat transfer fluid and the vapor or the chamber walls is an order of magnitude lower. Additional discussion accompanies the calculations below.

The heat transfer between the heat transfer fluid and the vapor in the chamber can be estimated assuming heat is transferred from the heat transfer fluid in the headers directly to the vapor through natural convection. The thermal resistance of the stainless steel plates can be neglected because the thermal resistance of the plates is much lower than the thermal resistance of natural convection. The heat transfer coefficient for laminar natural convection is taken from the work of Churchill and Chu (1975).

$$Nu = 0.68 + \frac{0.67Ra^{0.25}}{\left(1 + \left(\frac{0.492}{Pr}\right)^{\frac{9}{16}}\right)^{\frac{4}{9}}} \tag{4.4}$$

Assuming that the temperature of the heat transfer fluid is 100°C, the temperature of the chamber is 50°C, and both surfaces of the two solution headers (four faces, each 0.24 m × 0.05 m) are available to transfer heat via natural convection, the heat transfer rate between the coupling fluid and the vapor in the chamber is less than 4 W, which is less than 2% of the typical heat duty seen in the desorber. Furthermore, this analysis neglects the presence of the tubes of the falling film heat exchanger, which disrupt heat transfer on the inner surfaces of the solution header and reduce the area of that face. In addition, the temperature of the heat transfer fluid in the headers is often as low as 85°C in the upper headers, reducing the temperature difference between the heat transfer fluid and the chamber by up to 30% from the assumed value. Finally, the vapor temperature in the chamber during the desorber experiments is often closer to 55°C than 50°C, which reduces the temperature difference by 10%. These factors suggest that 4 W, as calculated above, is an overestimate of the heat loss due to natural convection. Therefore, this mode of heat transfer is neglected in the data analysis.

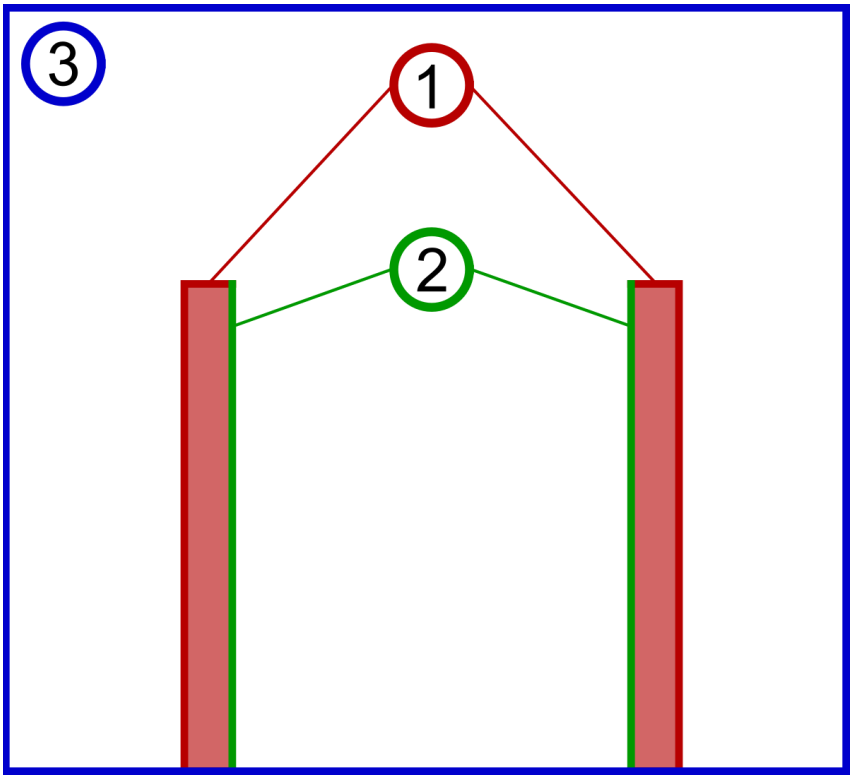

Figure 4.12: Surfaces for calculating radiation heat loss from coupling fluid

A similar analysis is conducted for the radiative heat transfer from the surfaces of the heat exchanger headers to the walls of the chamber. The setup for this analysis is shown in Figure 4.12. The headers are divided into two surfaces for radiation heat transfer. The front, back, top, and outside faces of the headers make up the first surface, which is fully exposed to the walls of the chamber. The inside faces of the headers are the second surface. Because the faces comprising the second surface are parallel and opposed to each other, the shape factor for this surface, $F_{2\rightarrow 2}$, is nonzero. It should be noted here that in this analysis, radiative heat transfer from the second surface to the tubes of the falling-film heat exchanger or to the falling film itself is neglected; therefore, the radiative heat loss to the chamber walls calculated by this method is greater than what will be seen in practice. The heat transfer from surfaces 1 and 2 to surface 3 is given by

$$\dot{Q}_{1,2\to3} = \frac{\sigma(T_1^4 - T_3^4)}{\frac{1-\varepsilon_1}{A_1\varepsilon_1} + \frac{1}{A_1F_{1\to3}} + \frac{1-\varepsilon_3}{A_3\varepsilon_3}} + \frac{\sigma(T_2^4 - T_3^4)}{\frac{1-\varepsilon_2}{A_2\varepsilon_2} + \frac{1}{A_2F_{2\to3}} + \frac{1-\varepsilon_3}{A_3\varepsilon_3}} \quad (4.5)$$

where the emissivity of the rough, unoxidized stainless steel of the heat exchanger headers is 0.36 (Shurtz, 2018), the emissivity of the aluminum of the vacuum chamber is 0.07 (Incropera and DeWitt, 1996), the areas of the surfaces are 0.037 m^2, 0.024 m^2, and 2.23 m^2, and the surfaces are assumed to be diffuse and gray. Assuming the temperature of surfaces 1 and 2 is 100°C and the temperature of surface 3 is 50°C, the heat transfer rate from surfaces 1 and 2 to surface 3 is 10 W, which is less than 3% of the typical heat load in the desorber. However, the walls of the chamber are not at a uniform temperature. Based on the work of Cess and Lian (1976), the emittance of the water vapor in the chamber during the high-pressure test is 0.11. Accordingly, an analysis was conducted that treated the water vapor as a participating medium. The heat transfer rate associated with this analysis was nearly identical to the heat transfer rate associated with the analysis in which the water vapor was treated as transparent.

The sheet heaters are only located in the back 15 cm of the top and the front 15 cm of the bottom of the chamber, but the temperature is measured at the top front of the chamber, which is the point in the chamber with the lowest temperature. Additionally, as discussed in the analysis of convection losses, the heat transfer fluid temperature drops substantially as it flows through the header, and the tubes on the heat exchanger will reduce the shape factor further from the inner surfaces of the headers. Therefore, radiation from the coupling fluid headers is neglected in the data analysis.

4.5.2 Solution Heat Transfer Rate

The heat transfer rate in the falling-film heat exchanger can also be determined by performing an energy balance on the LiBr solution flowing over the horizontal tubes of the heat exchanger. This energy balance yields

$$\dot{Q}_{f,soln} = \dot{m}_{soln,out} h_{soln,out} + \dot{m}_v h_v - \dot{m}_{soln,in} h_{in} \tag{4.6}$$

where the vapor enthalpy, h_v, is calculated at the chamber pressure and the average of the inlet and outlet solution temperatures, and the vapor mass flow rate, $\dot{m}_v$, is given by

$$\dot{m}_v = \dot{m}_{soln,in} - \dot{m}_{soln,out} \tag{4.7}$$

During absorption or desorption, it is expected that a negligible amount of LiBr leaves the heat exchanger, and thus, the following species balance should hold for the experimental data.

$$\dot{m}_{soln,in} w_{in} = \dot{m}_{soln,out} w_{out} \tag{4.8}$$

However, the experimental data showed discrepancies in the species balance as a result of fluctuations in the solution outlet flow rate. Figure 4.13 shows the inlet and outlet flow rates and concentrations during the steady-state portion of a high-pressure test. It can

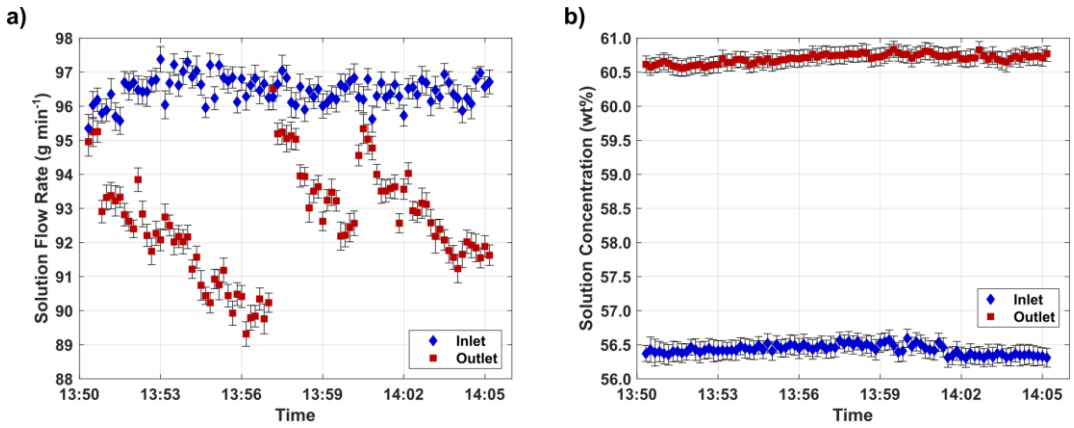

Figure 4.13: Steady-state a) solution flow rates and b) concentrations at desorber inlet and outlet during test conducted on 19 March 2021

clearly be seen that while the solution inlet mass flow rate and concentration and the solution outlet concentration are very stable over the period shown, the solution outlet flow rate experiences substantial fluctuations. This suggests that the measured outlet solution mass flow rate is influenced by the tubing between the outlet of the falling-film heat exchanger and the inlet of the flow meter, and thus, the measured values are not representative of the solution flow rate at the outlet of the falling-film heat exchanger. The outlet tubing consists of a long, horizontal length with vertical portions before and after. It is possible that waves in the horizontal portion of the tube result in the capture of vapor in the flow. This vapor then increases the resistance to flow after passing through the flow meter, requiring a higher gravitational head to drive the flow. Once the additional resistance has been removed, flow increases and the liquid level drops. Accordingly, the solution outlet mass flow rate is calculated using the species balance, and this calculated mass flow rate is used in the energy balance.

4.5.3 Uncertainty Propagation

The uncertainty in the measured data can be divided into two categories. Systematic uncertainty is inherent in the instrument and is provided by the manufacturer. The systematic uncertainties of the instruments used in the experiments are given in Table 4.3.

Table 4.3: Systematic uncertanties of instruments on test stand

Instrument	**Model**	**Systematic Uncertainty**
Mass Flow Meter	MicroMotion CMFS010	±0.1% of reading
Density Meter	MicroMotion CMFS010	±2 kg m^{-3}
Turbine Flow Meter	FTI FTO-1	±0.15% of reading
Pressure Gauge	OMEGA PX-409	±0.08% of reading
Thermocouples	OMEGA TMQSS	±0.25°C
Electrical Conductivity Meter	OMEGA CDE-45P	±0.3% of span

Random uncertainty, on the other hand, is associated with the unpredictability of the measurement process. In this work, a 95% confidence interval is used for the random uncertainty, which can be calculated as

$$U_{rand} = \frac{t(N, 0.95)s}{\sqrt{N}} \tag{4.9}$$

where *s* is the sample standard deviation, *t* is the value of the two-tailed Student's T-distribution with *N* degrees of freedom, and *N* is the number of samples. For each of the instruments listed in Table 4.3, each recorded data point was an average of 25 samples taken at a rate of 100 Hz. The standard deviation of the samples was also recorded, allowing a random uncertainty to be calculated. The total uncertainty in a measurement can be calculated from the systematic and random uncertainty as

$$U_i = \sqrt{U_{sys,i}^2 + U_{rand,i}^2} \tag{4.10}$$

The uncertainty in the measured values can be used to determine the uncertainty in the quantities calculated during data reduction. To propagate uncertainty through the calculation, the uncertainties of each value are weighted by their effect on the calculated value and summed in quadrature as shown in the following formula. An example of this uncertainty propagation is given in Appendix B.

$$U_y = \sqrt{\sum_i \left(\frac{\partial y}{\partial x_i} U_{x_i}\right)^2} \tag{4.11}$$

When averaging the time series data recorded during experiments, Equation 4. does not apply. Instead, the following equation is used to calculate the uncertainty in the average (Pérez Ballesta, 2005).

$$U_{\bar{y}} = \sqrt{\frac{\sum_{i=1}^{N} U_{y_i}^2}{N}} \tag{4.12}$$

4.6 Results and Discussion

4.6.1 Hydrodynamics

In Section 3.2, the minimum heat exchanger area required to avoid entrainment of secondary droplets by flowing vapor was calculated. The falling-film heat exchanger was designed to exceed this area. Observation of the heat exchanger during testing indicated that the vapor velocity was sufficiently low to avoid droplet entrainment. However, when the falling-film heat exchanger was operating as a desorber, bubble formation and bursting was observed in droplets on the last six rows of the heat exchanger. This resulted in the ejection of small droplets of LiBr solution from the falling-film heat exchanger. In early tests, these droplets impacted the floor of the vacuum chamber, the back window of the vacuum chamber, and the outside of the bucket containing the condenser. It is also possible that some droplets were carried onto the condenser by the vapor flow. To mitigate the potential for contamination of the distillate by this mechanism, a thin sheet of polycarbonate was placed between the desorber and the condenser during the high-pressure tests such that it blocked everything below the second row of the desorber. No effect on the desorption rate was observed as a result of this addition.

4.6.2 Water Purification

As discussed above, three feed solutions were used to assess the water purification capabilities of the water-purifying heat pump. DI water was used to determine if LiBr

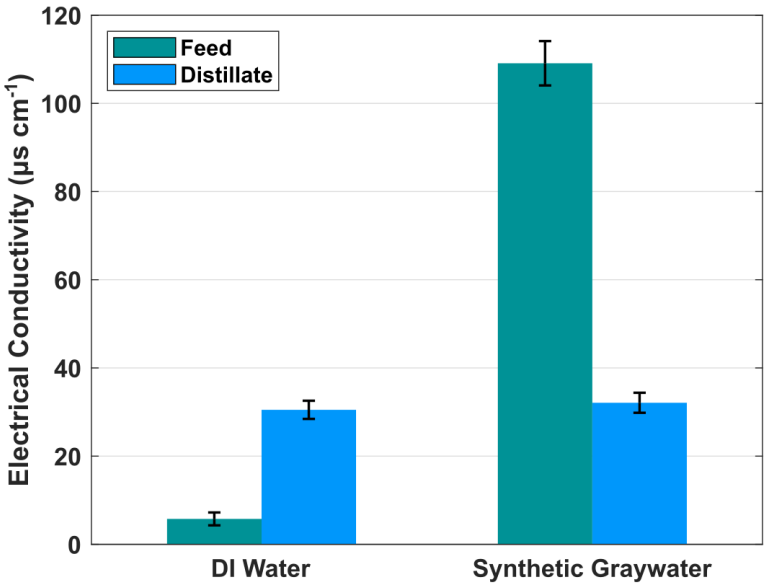

Figure 4.14: Electrical conductivity of DI water and synthetic graywater feed solutions and distillate

solution was transferred to the distillate stream, while synthetic graywater and 3.5 wt% NaCl solution were used as representative feed solutions. Figure 4.14 shows the electrical conductivity of the DI water and synthetic graywater feed solutions and resulting distillates. Five tests were conducted with DI water as the feed, while eight tests were conducted with synthetic graywater. It can be seen from Figure 4.14 that the conductivity of the DI water increases from 6 ± 1 µS cm^{-1} in the feed solution to 30 ± 2 µS cm^{-1} in the distillate. A calibration curve for low-concentration LiBr solutions indicates that the electrical conductivity for LiBr as a function of concentration is

$$\sigma = 1.0468 \times 10^{6} w + 15.4 \tag{4.13}$$

where w is the weight fraction and σ is the electrical conductivity in µS cm^{-1}. The data used to generate this curve are given in Appendix D. From this, it can be seen that the distillate produced by the water-purifying absorption heat pump cycle when DI water is used as the

feed contains 0.002 wt% LiBr. This is likely due to the presence of bubbles on the desorber that ejected droplets into the vapor phase when bursting. While droplets were not seen traveling to the condenser, the amount of LiBr required to enter the condenser to achieve a concentration of 0.002 wt% is quite small. In a typical test, ~300 mL of distillate was produced, which means that only 6 mg of LiBr had to enter the condenser to achieve this. Although this is a tiny amount of LiBr, there are no guidelines for either lithium or bromide in drinking water; therefore, subsequent iterations of the cycle must have modified designs to prevent the possibility of LiBr carryover.

With the baseline water purification capabilities of the cycle established, the water purification capabilities with respect to synthetic graywater can now be discussed. The synthetic graywater feed has a conductivity of 109 ± 5 μS cm^{-1}, which is somewhat lower than the conductivity of 188 ± 13 μS cm^{-1} reported by Hourlier et al. (2010). The reasons for this may be due to variations in the chemicals acquired from different manufacturers or due to the low-precision balance used to prepare the feed solution in these experiments. The distillate produced by the batchwise experiments operating with synthetic graywater had a conductivity of 32 ± 2 μS cm^{-1}, which agrees well with the electrical conductivity of the distillate produced by when DI water was used as the feed. This suggests that the water purification process the synthetic graywater undergoes is sufficient to remove ionic compounds from the feed to the limit imposed by solution carryover in the experimental setup.

The water purification capabilities of the system when operating on synthetic graywater were also evaluated using the TOC as a metric. Figure 4.15 shows the distillate TOC for each of the tests conducted. The average feed TOC was 92 ± 2 mg L^{-1}. The figure

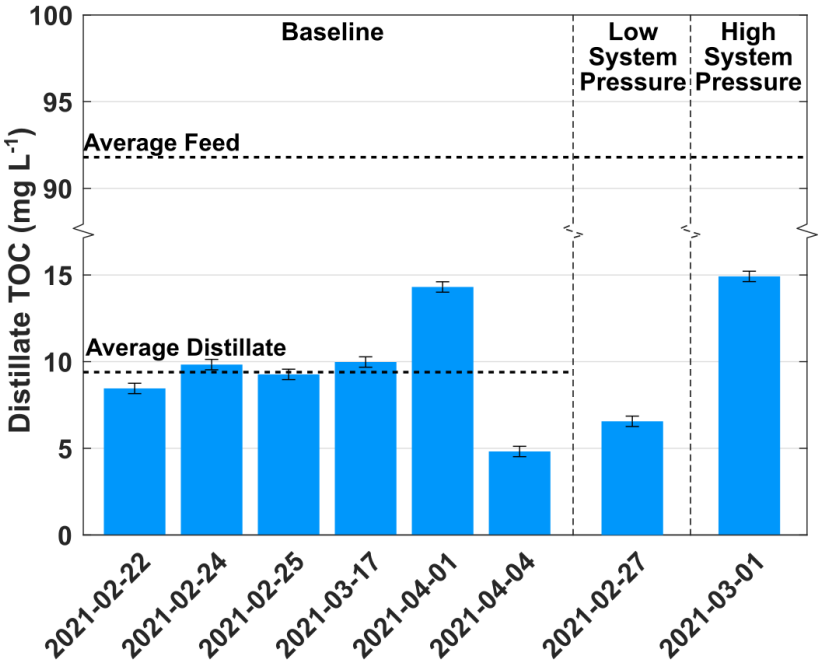

Figure 4.15: Distillate TOC for synthetic graywater tested at baseline, low pressure, and high pressure conditions

shows that the water purification process was able to substantially reduce the TOC, with the distillate at baseline conditions demonstrating an average TOC of 9.4 ± 0.1 mg L^{-1}. This is still substantially above the TOC requirement of a drinking water supply, suggesting that further investigation or additional treatment steps are required to reach this goal. The variation in the baseline distillate TOC shown in the last two tests may be due to contamination of the condenser with synthetic graywater during the low-pressure tests. This phenomenon is discussed further below. The primary reason why the TOC removal is only 90% is because of the presence of volatiles in the synthetic graywater. At the baseline saturation temperature of 5°C, glycerol has a vapor pressure of 1.6 mPa, which while small, is certainly nonzero (Cammenga et al., 1977). Varying the operating pressure as outlined in Table 4.2 demonstrated a change in the distillate TOC. Operation at lower

pressure yielded a distillate TOC of 6.6 ± 0.1 mg L^{-1}, while operation at higher pressure yielded a distillate TOC of 14.9 ± 0.1 mg L^{-1}. These data suggest that the pressure has a significant impact on the TOC; however, distillate TOC data collected at baseline conditions ranged from 4.8 ± 0.1 mg L^{-1} to 14.3 ± 0.1 mg L^{-1}, indicating that further testing at low and high pressure conditions is required to determine the effect of pressure on the purification of graywater.

A feed solution containing 3.5 wt% NaCl was also studied to determine the desalination capabilities of the water-purifying absorption heat pump. Because this feed solution only contained ionic species, the electrical conductivity was used to assess water quality. A calibration curve was developed for low-concentration NaCl and relates the electrical conductivity to the NaCl concentration as follows. The data used to produce this curve are given in Appendix D.

$$\sigma = 1.9656 \times 10^{6} w + 12.7 \tag{4.14}$$

As with the calibration curve for LiBr, w is the weight fraction of the salt and σ is in μS cm^{-1}.

Figure 4.16 shows the distillate concentration of NaCl for each of the tests run using 3.5 wt% NaCl as the feed. The tests were run in two groups, with three tests conducted early March and two tests conducted in early April. The ability of the experiments to purify the feed solution without volatiles is good, with an average salt removal of 99% demonstrated. In each group of tests, the distillate concentration rises over the course of multiple tests. This is likely due to the contamination of the evaporator with crystallized NaCl. Even though distilled water was used to rinse the heat exchanger between the low-pressure and high-pressure tests, crystallized salt was seen on the condenser at the end of

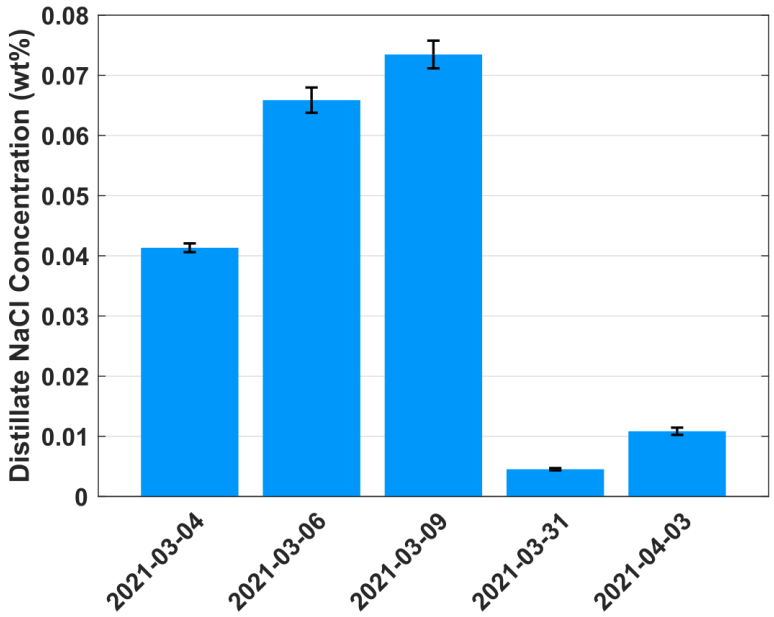

Figure 4.16: Concentration of NaCl in distillate for tests with 3.5 wt% NaCl feed solution

multiple high-pressure tests suggesting that the cleaning methods were unable to remove all the salt on the evaporator tubes at the end of the evaporator test.

There are two possible explanations for the improved water purification behavior demonstrated by the second set of tests. The first is that small changes to the cleaning procedures resulted in better salt removal between the low-pressure test and the high-pressure test. The second is that the solution in the bucket was not well-mixed. During the first set of tests, the conductivity of the feed solution was 42400 ± 500 μS cm^{-1}, while during the second set of tests, the feed solution conductivity was 23000 ± 1000 μS cm^{-1}, even though the initial concentration of the feed solution was the same. The solution was prepared differently in the two sets of tests. In the first set, three 3.78-L jugs were used to prepare the solution, with each jug being shaken to ensure homogeneity. In the second set, the NaCl was added directly to the bucket, and 10.4 L of water were added to it. It is

possible that this preparation method resulted in a concentration gradient in the solution with a lower concentration layer at the top. This could imply that any droplets of NaCl ejected from the pool were at a lower concentration, and thus, the cleaning procedure used was more able to remove residual NaCl from the heat exchanger.

Taking the water purification results presented above in aggregate, it is clear that the components of an absorption heat pump are capable of a high degree of water purification. Although the double-distillation process is unable to completely remove volatile components from a feed solution, it demonstrates a marked reduction in those components, as demonstrated by the TOC measurement. Furthermore, removal of dissolved ions exceeds 97% in all tests conducted, with the best test reaching 99.9% salt removal.

4.6.3 Cooling Demonstration

As discussed in Section 2.2, the water-purifying absorption heat pump can both provide cooling and purify water. The water purification capabilities demonstrated in the batchwise experiments are discussed above. When discussing the cooling capabilities of the cycle, it is important to recognize that there are several factors influencing the evaporator duty in the batchwise tests that would not be present in a full system operating in steady state. The first and most important factor is that the evaporator heat duty is used as a control parameter in the batchwise tests to maintain the chamber at the target pressure during the test. Additionally, in the majority of tests, the feed solution in the bucket containing the evaporator was at ambient temperature prior to the test. As the chamber pressure decreased, the saturation temperature of the feed solution decreased, leading to

cooling of the solution. However, to maintain the chamber pressure, additional heat often had to be added to the feed solution by the evaporator to achieve the vapor generation rate necessary to maintain the chamber pressure. Finally, the vapor volume of the vacuum chamber is connected to the vapor volume in the solution supply and receiving tanks. Depending on the temperature in these tanks, desorption or absorption can occur, affecting the required vapor generation rate in the evaporator.

The combination of the above factors indicates that is it not useful to compare the evaporator duties to a model parameter or even to the duties of other tests. However, what can be said is that in all tests where there was not a leak in the chamber (which is discussed further in Section 4.6.4), the evaporator provided a nonzero amount of cooling to the heat transfer fluid stream flowing through it, indicating that a full cycle that does not face the complicating factors discussed above for the batchwise experiments will be capable of demonstrating cooling as well as water purification.

4.6.4 Absorber Model Validation

One of the major factors affecting the cooling load in the batchwise experiments was the absorber load. As discussed in Section 4.3.1, during the low-pressure tests, the absorber solution flow rate, the absorber heat transfer fluid flow rate, and the absorber heat transfer fluid chiller set point temperature were held constant. The absorbent solution was heated to near saturation conditions, but due to variability in the absorbent solution inlet concentration, which ranged from 53.7 wt% to 58.9 wt% over the course of the tests, this inlet temperature varied between tests.

As discussed in Section 4.5, the heat transfer rate in the absorber can be calculated by performing an energy balance on the coupling fluid or on the solution. Figure 4.17 shows these two heat transfer rates for all tests conducted. There is acceptable agreement between the heat transfer rates calculated for the two streams.

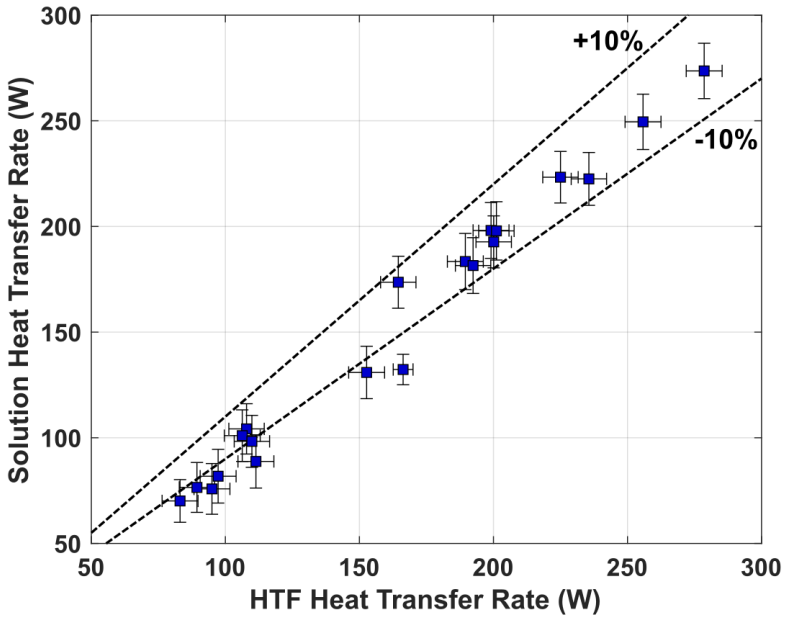

Figure 4.17: Measured solution and HTF heat transfer rates in the absorber

The values agree best for higher heat transfer rates, which are closer to design conditions. At heat transfer rates near 100 W, there is more disagreement between the two measurements, with the solution heat transfer rate being lower than the coupling fluid heat transfer rate. This may be due to uncertainties in the solution outlet concentration for small changes in concentration. The average absolute deviation (AAD) is used as a metric to describe the agreement between the two values and is defined as

$$\text{AAD} = \frac{1}{N}\sum_{i=1}^{N}\frac{\left|x_{i,1} - x_{i,2}\right|}{x_{i,1}} \tag{4.15}$$

where N is the number of measured data points and the subscripts 1 and 2 refer to the compared quantities. For the absorber heat transfer rates, the AAD is 8.5%. In the following discussion, the solution and heat transfer fluid heat transfer rates are averaged to yield a single experimental heat transfer rate.

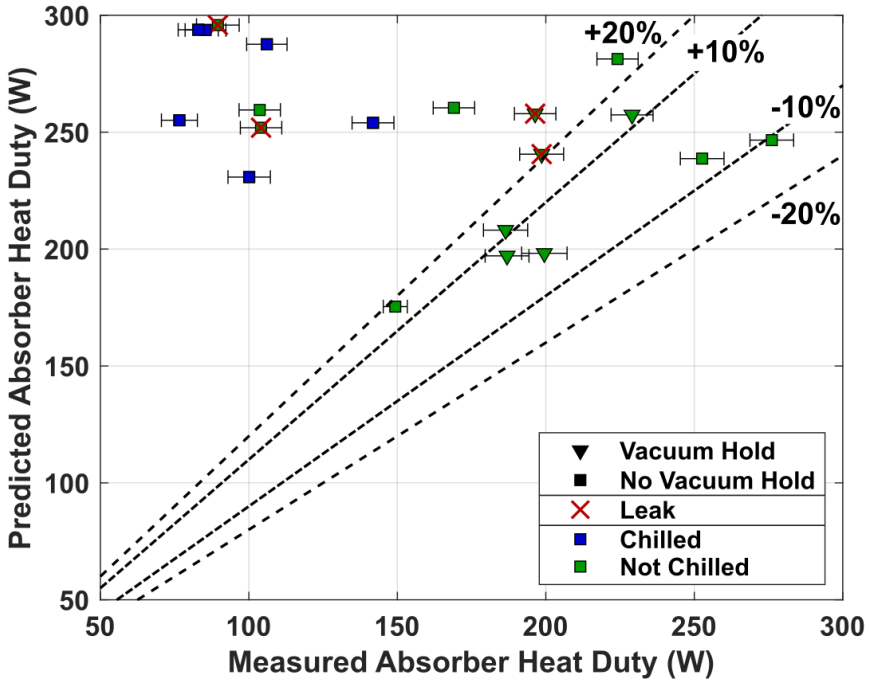

Figure 4.18: Predicted and measured absorber heat duties

The absorber heat transfer rates predicted by the model and measured in the experiments are shown in Figure 4.18. It becomes immediately obvious from the figure that there are a number of factors that influence the agreement between the predicted and measured heat duties. Over the course of the experiments, a leak developed in one of the valves that allowed air to leak into the test stand at a rate of 40 μmHg min^{-1} during the tests. The tests affected by this leak were identified through examination of the condenser heat transfer fluid data due to the reliability of the condenser. In tests unaffected by the leak, the condenser heat transfer fluid outlet temperature was nearly identical to the saturation

temperature in the chamber. In tests affected by the leak, the condenser heat transfer fluid outlet temperature deviated from the chamber saturation temperature by 2 K or more. As expected, when there is a leak in the chamber, the additional mass transfer resistance added by the air, which was not accounted for in the absorber model, results in the model overpredicting the heat transfer rate.

It is interesting when examining data points with a leak how strongly the startup procedure affected the performance of the system. When a 36-hour hold at 6.9 kPa was performed prior to final evacuation and the test (denoted by a triangular data point in Figure 4.18), the deviation between the predicted and measured absorber heat duty was much less, even in the presence of a leak. It should be noted that during this vacuum hold, the leaking valve was closed, and in this state, the valve did not leak. This behavior suggests that despite the leak, another factor is present in the experiments that results in a vacuum hold improving the performance. The data also suggest that this factor occurred over time. The two data points in the upper right of the graph near the -10% line were the first two tests conducted on the absorber with the target solution flow rate. The data point just below the +20% label was for a test conducted two weeks later.

The cluster of data points at the upper left of the graph when the feed solution was chilled immediately prior to the test suggest a possible explanation for the poor performance. There were two main differences that occurred when a test was conducted with a chilled feed. First, the time required to evacuate the chamber was much shorter, indicating that dissolved air may still be present in the feed solution. Second, boiling of the feed solution did not occur during the evacuation procedure, suggesting that the

composition of the vapor phase in the chamber at the end of evacuation was much higher in air that when the feed solution was not chilled.

The amount of dissolved air in the feed solution can be calculated using Henry's law.

$$C = Hp \tag{4.16}$$

where C is the concentration of dissolved gas and H is the Henry's law constant. Temperature-dependent Henry's law constants for nitrogen and oxygen are taken from a compilation by Sander (2015). Using these values and an atmospheric composition of 78% nitrogen and 22% oxygen, it is found that at 1°C, water can accommodate 0.0074 mol of nitrogen and 0.0045 mol of oxygen. This amount of gas, assuming ideal behavior at 15°C in the 0.227-m^3 volume of the vacuum chamber, would have a pressure of 125 Pa. During the low-pressure tests, the nominal chamber pressure is ~870 Pa; thus, if all the dissolved gas in the chilled feed solution is released into the chamber, a mass fraction of air in the vapor of ~20 wt% could be achieved. In the tests with a chilled feed and a more rapid evacuation, it is also probable that the initial composition of the vapor phase in the chamber is less than 100% water vapor, which could contribute further to the air fraction in the chamber. If the vapor phase contained 50 wt% air at the end of evacuation, the addition of the dissolved air could result in 60-70 wt% air in the chamber during the test. To account for this, vapor-side mass transfer effects are added to the absorber model.

4.6.4.1 Vapor-Side Mass Transfer Modeling

To account for the mass transfer resistance associated with phase change in the presence of non-condensable gases, the mass transfer rate at the interface can be calculated by

$$\dot{m}_{lv,i} = \beta_{v,i} A_o C_{v,i} \ln\left(\frac{1 - x_w}{1 - x_{wi,i}}\right) \tag{4.17}$$

where $\beta_{v,i}$ is the vapor-side mass transfer coefficient, $C_{v,i}$ is the molar concentration of the vapor at the row being evaluated, x_w is the bulk concentration of water in the vapor phase, and $x_{wi,i}$ is the interface concentration of water vapor at the row being studied (Hewitt et al., 1994). Two Sherwood numbers are used for the vapor phase to account for the interaction of boundary layers between tubes in the absorber. It has been shown that the gas leaving the lower tubes in an array reduces convective transfer for higher tubes in the array (Marsters, 1972; Corcione, 2005). The Sherwood number correlation used for the lowest tube is (Schütz, 1963)

$$Sh = 0.53 Gr^{0.25} Sc^{0.25} \tag{4.18}$$

while the Sherwood number correlation used for all other tubes in the array is adapted from a heat transfer study by Corcione (2005).

$$Sh_i = Gr^{0.25} Sc^{0.25} \left[0.364 \ln\left(\frac{\left(\frac{(N_r - N_i)s}{d}\right)^{0.4}}{(N_r - N_i + 1)^{0.9}} \right) + 0.508 \right] \tag{4.19}$$

In this correlation, N_r is the number of tube rows, N_i is the tube row for which the Sherwood number is being calculated, numbered starting from the top row, and s is the center-to-center spacing between tube rows. Because the investigation of Corcione (2005) only considered arrays of up to six tubes, a constraint was imposed such that the coefficient

generated by the term in square brackets could be no lower than 0.265, which is half the coefficient for the lowest tube row.

Because the vapor pressure at the interface is depressed, Equation 3.8 is modified to read

$$w_{eq,i} = w(T_{\ell,i}, p_{wi,i}) \tag{4.20}$$

where $p_{wi,i}$ is the partial pressure of water vapor at the interface and is calculated assuming the vapor phase behaves as an ideal gas.

$$p_{wi,i} = x_{wi,i}p \tag{4.21}$$

With this model complete, the air fraction required for the model results to match the measured data can be determined. These results are presented in Figure 4.19 as a function of the measured absorber heat duty. Because the experiments were almost all

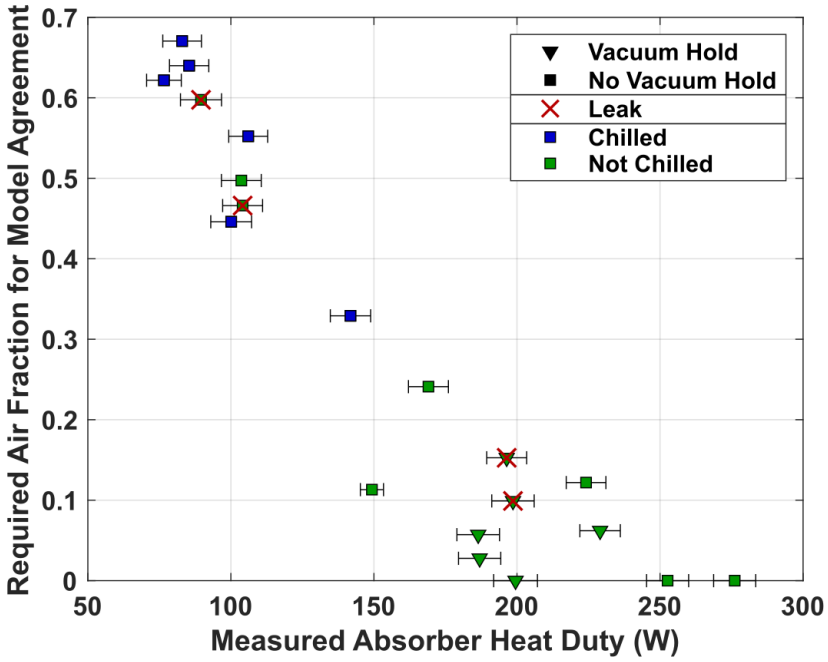

Figure 4.19: Required air mass fraction for predicted and measured absorber heat duty to agree

conducted for similar operating conditions, the trend of decreasing required air fraction with increasing absorber duty is expected. The figure shows that when the feed solution is chilled, an air fraction in excess of 0.3 is required to achieve agreement with the measured values. If the data point with a measured heat duty of ~140 W and a required air fraction of ~0.33 is excluded, it suggests that an air fraction of 0.45-0.68 is required to predict the measured data with a chilled feed. The lower required air fraction for the data point with the chilled feed at ~140 W is likely because during that test, the solution in the supply tank was heated above the saturation temperature. This probably led to boiling in the supply tank, increasing the amount of vapor in the system and reducing the air fraction at the same pressure. Excluding that test suggests that in tests with a chilled feed, the air fraction in the system is ~0.55, which seems reasonable based on the prior discussion of dissolved air in the feed solution and the absence of boiling during the short evacuation period.

For most of the tests that are not chilled, the required air fraction to match the experimental heat duty is ~0.1 or less. Whether or not this is reasonable can be seen by considering how much air would enter the system over the course of a test. Over the last four vacuum tests conducted on the system, the average leak rate was 1.7 μmHg min^{-1}. A typical low-pressure test lasted 90 minutes. Therefore, the air fraction at the end of a typical low-pressure test was 0.04. This aligns reasonably well with the required air fractions for the models to agree with these test results.

The required air fraction for the tests conducted when the chamber was leaking is highly variable. This suggests that the leak rate cannot be predicted well. Consequently, the points during which a leak occurred in the test are excluded from further analysis, as

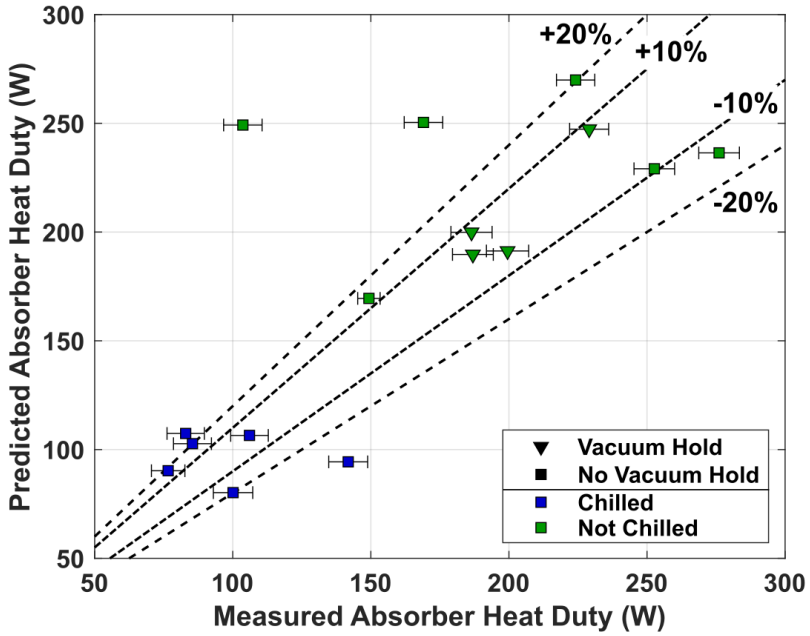

Figure 4.20: Comparison between predicted and measured absorber heat duty with air mass transfer correction applied

this was due to a failure of a component on the test stand rather than through any phenomenon in the experiments.

Figure 4.20 shows the predicted and measured heat duties for the absorber with an air fraction of 0.55 applied to tests with a chilled feed and an air fraction of 0.02 applied to tests without a chilled feed. With this correction applied, the agreement between the model and the experiments is better, although only 62% of the data points fall within the ±20% range. Of the six data points that fall outside of the range, three of them are from experiments conducted with a chilled feed. The corrections for a chilled feed solution have been discussed above.

Of the other three data points that fall outside the ±20% range, two are worth noting. The first is the data point with a measured duty of ~100 W and a predicted duty of ~250 W.

The experiment associated with this data point was the last one conducted prior to a leak beginning in the chamber. Comparing this point to the other data points for experiments with leaks in Figure 4.19 suggests that there may have been a leak in the chamber during this experiment that did not appear during the subsequent high-pressure test. The second data point that falls substantially outside the ±20% range is the one with a measured heat duty of ~165 W and a predicted heat duty of ~250 W. This test was conducted shortly after a test with a chilled feed, and the temperature of the feed solution had not yet reached ambient temperature when the test was started. This suggests that there was more air in the system than was present during tests conducted with the feed starting from ambient temperature but still less than when the feed was chilled prior to evacuation.

Figure 4.20 also shows that the model predictions for tests conducted with a vacuum hold all fall within ±10% of the measured data, indicating that when dissolved air is removed from the feed solution, the model is able to predict the experimental performance reasonably well.

4.6.5 Desorber Model Validation

In contrast to the absorber, the desorber experienced much less variation in the operating conditions. The heat transfer rates for the desorber as calculated using the solution and the heat transfer fluid are shown in Figure 4.21. All of the data fall within a 100-W range when measured using the heat transfer fluid. 90% of the data agree within 10%, and only one data point shows severe deviation. The data point showing severe deviation is from an early test where the valve on the line leaving the chamber was set so that vapor was able to enter the Coriolis flow meter. This led to an erroneous density

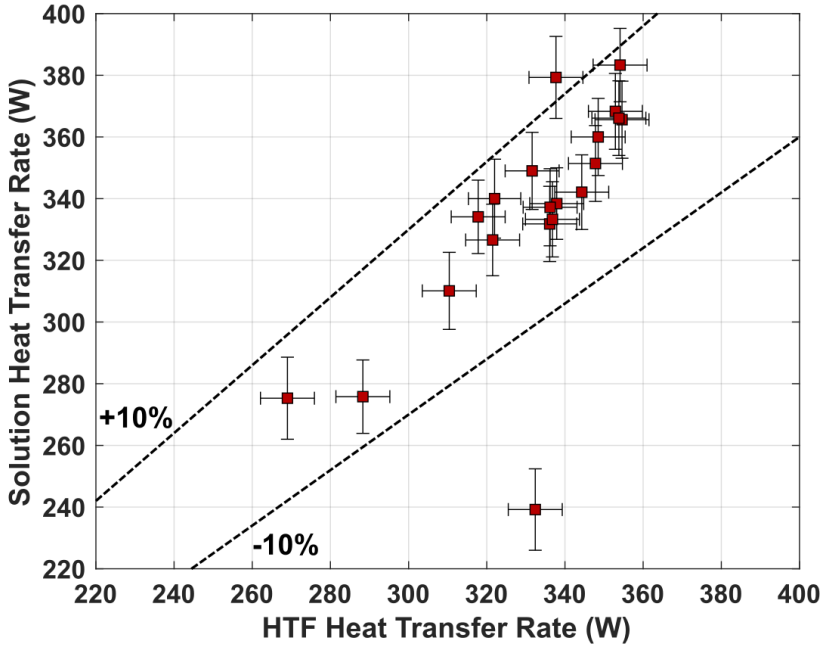

Figure 4.21: Measured solution and HTF heat transfer rates in the desorber

reading, which resulted in an incorrect solution outlet concentration. As such, it is excluded from this analysis as an outlier, and in further analyses on the desorber, the heat transfer fluid heat transfer rate is used rather than the average for this data point. When this outlier is excluded, the AAD of the two heat methods of calculating heat transfer is 3.3%.

Figure 4.22 shows the predicted and measured heat transfer for the desorber for all three feed solutions used. It can be seen that all the data points lie very close to the +10% line, and there is no pattern with respect to the feed, suggesting that the desorber performance is not influenced by the feed solution used in the evaporator. Similarly, the desorber performance is not influenced by the presence of the leak in the chamber. These points are included in the plot, but they cannot be distinguished from points collected when there was no leak in the chamber, suggesting that air-side mass transfer is not a concern in

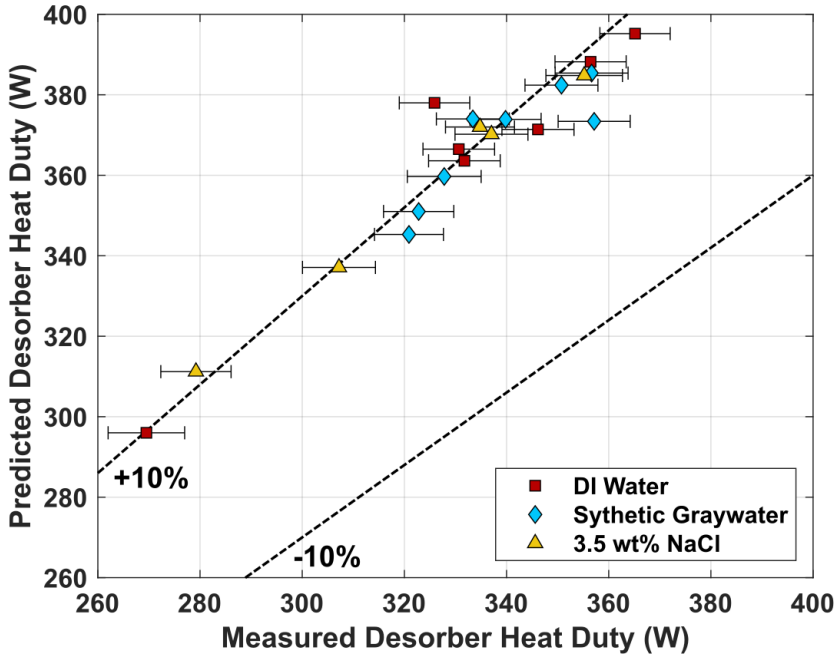

Figure 4.22: Predicted and measured desorber heat duties

the desorber. The AAD between the predicted and experimental heat duties for the desorber is 8.6%.

The tight grouping of the heat duties around the +10% line indicate that there is some phenomenon occurring in the experiments that is not being accounted for by the model. During desorber model development, mass transfer was neglected after exploring the model of Jani (2012). While no other mass transfer models could be found for mass transfer during desorption of water vapor from LiBr falling films on horizontal tubes, two other mass transfer coefficients were considered. The first was the correlation of Babadi and Farhanieh (2005), which was used in the absorber mass transfer model and was developed for falling-film absorption into a LiBr solution on a horizontal tube. The second was the correlation of Yih and Chen (1982), which was developed for absorption of oxygen and carbon dioxide into a falling film of water on a vertical tube. Figure 4.23 shows the

predicted and measured heat duties of the desorber when modeled without mass transfer and with the two mass transfer coefficients discussed above. It is clear that neither of these mass transfer coefficients is suitable for use with this desorber geometry and flow conditions, with both underpredicting the experimental data by 20% or more (AADs of 60.2% and 25.0% for the correlations of Babadi and Farhanieh (2005) and Yih and Chen (1982), respectively). The poor performance of the correlation of Babadi and Farhanieh (2005) can be explained by the dependence on the Schmidt number. In most mass transfer correlations, the Schmidt number is raised to an exponent less than unity, indicating that as the diffusivity of the solution increases, the mass transfer also increases. In contrast, in this correlation, the exponent on the Schmidt number is greater than unity, suggesting that the mass transfer coefficient decreases as the diffusivity increases. While this does not matter for the absorber because the Schmidt number is unlikely to vary much from the

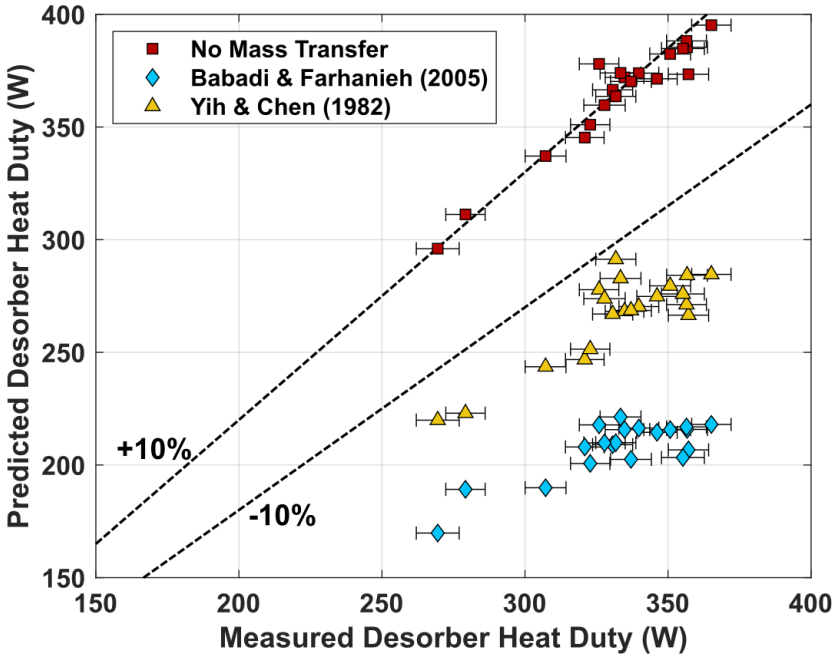

Figure 4.23: Predicted and measured desorber heat duties using different mass transfer correlations

conditions under which the model was developed, it is much more significant for the desorber, in which the diffusivity can be higher by a factor of 2.

While it is possible that there is a mass transfer limitation in the desorber performance, it is also possible that the desorber does not operate in a mass transfer-limited regime, but instead, the heat transfer is overpredicted by the correlation of Hu and Jacobi (1996b). They used tubes with diameters between 15.88 and 22.22 mm, while the tubes on the desorber in this study were 3.175 mm in diameter. Modeling of heat transfer in falling films on horizontal tubes has typically divided the tube into three regimes for heat transfer, the first of which is treated as a jet impinging on a horizontal surface (Chyu and Bergles, 1987; Liu et al., 2021). This results in a higher heat transfer coefficient for the first 30° of the tube. Although this model describes the flow well for large tubes, such as those used by Hu and Jacobi (1996b), the model of a jet impinging on a horizontal surface does not apply when the diameter of the jet is approximately the same as the diameter of the tube. In the experiments conducted in this study, it was observed that the diameter of the droplets was very similar to the diameter of the tube. Based on this, it is expected that the heat transfer rate in the impingement zone at the top of the tube will be lower than suggested by the models available in the literature. Although a full analysis of this flow morphology and the resulting heat transfer lies outside of the scope of this work, a brief analysis of the work of Liu et al. (2021) suggests that ~20% of the heat transfer on a horizontal tube occurs in the first 30°. If this heat transfer is reduced by half, the overall heat transfer would be reduced by 10%, which would account for the discrepancy between the model and the experiments seen here.

4.7 Conclusions

In lieu of operation of a complete cycle, batchwise experiments are conducted using the components found in a water-purifying absorption heat pump to demonstrate the capability of the cycle to execute simultaneous water purification and cooling. The experiments consist of two processes: low-pressure evaporation and absorption, and high-pressure desorption and condensation. By operating the processes sequentially, water purification has been demonstrated using only the components in an absorption heat pump.

Water purification is demonstrated using DI water, synthetic graywater, and 3.5 wt% NaCl as the feed solutions. A rise in conductivity of the DI water following the test indicates that LiBr may be contaminating the distillate at concentrations up to 0.002 wt%. Conductivity tests following the synthetic graywater tests show a reduction to the same level achieved in the DI water tests. TOC analysis of the distillate produced by the synthetic graywater tests shows ~90% removal of TOC, which suggests that some volatile components are being transferred to the distillate. Testing with 3.5 wt% NaCl as the feed shows >98% salt removal. In all experiments, cooling was demonstrated in the evaporator during the low-pressure test.

The heat transfer performance of the absorber and desorber was measured and compared with the model predictions. In several tests, the absorber performance suffered from a high air content in the chamber; thus, the model was modified to include the vapor-side mass transfer phenomena. This correction led to all points without a leak and with a hold at vacuum prior to chamber evacuation falling within 10% of the model predictions, while 63% of the overall tests were within 20% of the model predictions. The desorber performed similarly for all tests, with an AAD of 8.6% between the measured values and

the model predictions. Mass transfer modeling on the liquid side was attempted; however, the available mass transfer models severely underpredicted desorber performance. It is hypothesized that the small tubes in the desorber relative to the size of the droplets generated led to depression of heat transfer in the impingement region, which could account in part for the model overprediction.

CHAPTER 5. CONCLUSIONS AND RECOMMENDATIONS

5.1 Conclusions

The following are the key contributions of this work:

- Creation of a novel thermodynamic cycle based on an absorption heat pump capable of simultaneous space conditioning and water purification
- Experimental demonstration of reduction in the pollutants in a prepared feedwater using the components in an absorption heat pump cycle under conditions that would allow for space cooling

The activities conducted in the pursuit of these accomplishments are summarized below.

A novel water-purifying absorption heat pump was designed, and a thermodynamic model was developed to analyze the cycle performance. A figure of merit, the energy ratio (ER), was defined to allow the calculation of the total cycle utility relative to the energy required to drive the cycle. The incorporation of water purification doubled the ER of the cycle. Cycle performance was assessed for 14 different absorbents, and LiBr and NaOH were selected for further study based on their high ER, low complexity, and suitability from prior work.

Further thermodynamic studies were conducted to increase the water purification capabilities of the cycle above 35.2 kg day^{-1} kW-$cooling^{-1}$. Forward osmosis (FO), membrane distillation (MD), and humidification-dehumidification (HDH) were explored as methods for providing the additional water purification. The results of these studies

showed that the performance of the cycle with HDH exceeded the performance of the other two methods, largely because the increase in the evaporator load when using HDH increases water produced through the base water-purifying absorption heat pump, reducing the amount of water that has to be produced through the secondary system.

A heat exchanger capable of acting as an absorber or desorber in a small-scale (300 W cooling) version of the cycle was designed. An overall analysis of the heat exchanger using the UA-LMTD method was performed to determine if either LiBr or NaOH was substantially better than the other. This showed that due to the low flow rate and high viscosity of NaOH at baseline conditions, an absorber using it as the solution would have to be prohibitively large. Therefore, LiBr was selected as the absorbent for the proof-of-concept demonstration.

A horizontal-tube, falling-film heat exchanger was designed to serve as the absorber or desorber in the proof-of-concept experiments. The heat exchanger had 36 rows of 3.175-mm OD tubes arranged in two columns. Coupling fluid flowed from the bottom of the heat exchanger to the top in six passes, with six rows in each pass. A design model was formulated for the heat exchanger that accounted for both heat transfer and mass transfer effects in the falling liquid film during desorption and absorption. After evaluating the model with and without mass transfer effects, it was concluded that mass transfer had a small but important effect in absorption, while the only available mass transfer coefficient available in the literature for falling-film, horizontal-tube desorption from LiBr solutions severely overpredicted the effects of mass transfer. Therefore, mass transfer in the desorber model was neglected. The models were simulated for tube lengths ranging from 0.12 to 0.30 m and for the solution flow rates and concentrations associated with absorber

equilibrium solution outlet temperatures ranging from 35 to 45°C. Heat transfer fluid flow rates were held fixed at the baseline levels defined in Chapter 2. Based on the results of these simulations, a tube length of 0.24 m and an absorber equilibrium solution outlet temperature of 37.5°C were selected for the proof-of-concept experiments.

A test stand incorporating a vacuum chamber with an interior volume of 0.227 m^3 was constructed to demonstrate the water purification and cooling capabilities of the cycle. The experiments were conducted in a batchwise manner, with the low-pressure processes (evaporation and absorption) being performed first, followed by the high-pressure processes (desorption and condensation). Although these processes are conducted in a batchwise, rather than a cyclic manner, these experiments are still sufficient to demonstrate the potential for a cycle of this type to perform simultaneous cooling and water purification because all the processes are suitably demonstrated.

Experiments were conducted at baseline conditions. To account for the variability and transient nature inherent in batchwise experiments, the evaporator and condenser were used to control the pressure in the cycle. Three feed solutions were tested: DI water, synthetic graywater, and 3.5 wt% NaCl. Electrical conductivity and total organic carbon (TOC) were used to assess water quality. Electrical conductivity measurements of the distillate produced by DI water feed solutions revealed an increase from 6 ± 1 $\mu S\ cm^{-1}$ to 30 ± 2 $\mu S\ cm^{-1}$, indicating that in the test stand, some LiBr is being carried into the distillate, resulting in a LiBr concentration of 0.002 wt%.

Electrical conductivity measurements of the synthetic graywater showed a decrease in electrical conductivity from 109 ± 5 $\mu S\ cm^{-1}$ to 32 ± 2 $\mu S\ cm^{-1}$, suggesting that the processes in the water-purifying heat pump reduce dissolved ions in synthetic graywater to

the same level achievable in DI water. TOC measurements showed a reduction in TOC from 92 ± 2 mg L^{-1} to 9.4 ± 0.1 mg L^{-1}. This indicates that volatile compounds in the graywater migrate from the feed solution to the distillate through the two distillation processes. Preliminary test data at higher and lower pressures suggest that operating pressure may affect this purity, with lower operating temperatures and pressures leading to higher purity.

Concentration measurements (converted from electrical conductivity measurements) on the 3.5 wt% NaCl solution indicate a drop in concentration from 3.5 wt% to 0.04 ± 0.02 wt%, which is nearly a 99% decrease in salt concentration. In a full cycle, the salt removal is projected to be higher, as salt contamination occurred on the tubes of the heat exchanger used as the evaporator and condenser in the batchwise experiments, adding contamination that would not be there if separate heat exchangers were used.

The heat transfer results on the absorber and desorber were used to validate the design models. For both components, the measured heat transfer on the heat transfer fluid side and the solution side agreed well (AAD of 8.5% for the absorber, AAD of 4.9% for the desorber). Comparison with the model results of the absorber indicated that there was a significant mass transfer resistance in the vapor phase due to the presence of non-condensable gases. A mass transfer model for the vapor phase was developed for the absorber, which when combined with the existing model, reduced the AAD between the predicted and measured absorber heat transfer rates from 34.5% to 18.6%. A further reduction could be achieved through the use of the initialization procedures developed late in the test program; the AAD between the predicted and measured absorber heat transfer rates for these data points was 5.0%.

The desorber demonstrated better agreement than the absorber between predicted and measured heat duties, with an AAD of 8.6%. However, the data are tightly clustered with the model overpredicting the measured values in all cases. This suggested that there may have been a factor not considered by the model. Two additional mass transfer correlations in the liquid film were explored; however, both resulted in substantial underprediction of the data (AADs of 60.2% and 25.0% for the correlations of Babadi and Farhanieh (2005) and Yih and Chen (1982), respectively). It is possible that the discrepancy between the predicted and measured heat duties is due to changes in the flow morphology when the droplet diameter approaches the tube diameter resulting in the elimination of enhanced heat transfer on the top 30° of the tube in a falling film due to the assumption of a jet impinging on a horizontal surface no longer being suitable.

With these experiments, it has been shown that water purification and cooling can be achieved through evaporation of vapor from an impure feed and absorption of the vapor into a LiBr solution at low pressure, followed by desorption of the vapor and condensation at high pressure. This is sufficient to prove that the water-purifying absorption heat pump designed in this work is feasible for its intended purpose.

5.2 Recommendations for Future Work

Although the feasibility of using a modified absorption heat pump to achieve water purification and cooling has been demonstrated in this work, there is ample space for further investigations in this area and in tangentially related areas, which have been uncovered over the course of these investigations. The first and most obvious area for future work is the full demonstration of the complete cycle. The experiments conducted

here were able to show water purification and cooling could be achieved, but their batchwise nature prevented evaluation of the cycle performance using standard figures of merit. A demonstration of the complete cycle at both on-design and off-design conditions will allow the assessment of the ER, along with the COP.

Although the thermodynamic analysis conducted here was sufficient to demonstrate reasonable performance of a water-purifying absorption heat pump, several other factors must be considered before a real-world implementation is possible. These include rigorous thermoeconomic analysis, sustainability analysis investigating the carbon equivalent emissions associated with the fabrication, operation, and decommissioning of the cycle, and the energy return on investment and water return on investment of the cycle.

In this work, it was shown that the cycle is highly suitable for the removal of dissolved solids, but its ability to purify feed solutions containing volatiles is lower. This finding suggests two future directions of research. The first is the exploration of different feed solutions, including feed solutions containing organic matter or suspended solids, which may be found in real graywater streams. Purification of these streams may require development of evaporator designs that are robust in the presence of suspended solids or the incorporation of filtration methods that can remove particulates before the feed solution is sent to the evaporator. The second area of research is methods to address feed solutions containing volatile compounds. This may include cycle operation at a lower evaporator pressure or the use of other water purification processes to remove the volatile components from the distillate after the use of the water-purifying absorption heat pump.

Additionally, the tests conducted with DI water as the feed showed the presence of a low concentration of LiBr in the condensate. To address this, alternative designs for the

desorber that prevent the transition from the film boiling mode to the nucleate boiling mode, which will suppress droplet formation, can be explored. Alternatively, the incorporation of a demister or other droplet removal device could be considered to determine its impact on the cycle performance.

In the batchwise experiments conducted here, and even in a closed cycle demonstration, it is possible to remove most of the dissolved gases from the feed solution prior to system operation, providing a low air fraction in the vapor phase. In a practical system, new feed solution will be continually added to the system, carrying dissolved air along with it. As the feed solution is depressurized to the evaporator conditions, the dissolved air will enter the vapor phase and reduce absorber performance, as seen in some of the tests conducted in this work. Therefore, future exploration into mitigating the effects of dissolved air is necessary. These studies may take the form of system designs that induce concentration gradients in the vapor phase to reduce air buildup at the interface, absorber and condenser designs that can operate at high air fractions, or mechanisms for removing air in the vapor phase from the system without removing a large amount of water vapor.

Finally, the results of the desorber experiments indicate that the heat transfer is overpredicted by the existing model. This may be due to a change in the flow morphology. As the size of the tubes used in the falling-film heat exchanger approaches the size of the droplets generated in the heat exchanger, the commonly used assumption of an impinging jet on the upper sixth of the tube may begin to break down. Detailed analytical, computational, and experimental studies should be conducted to understand falling-film heat transfer for small-diameter tubes, as these effects have not yet been well-studied in the

literature. The results of these studies can be used to guide falling-film heat exchanger design both within and outside of the area of absorption heat pumps.

APPENDIX A. PROPERTY REFERENCES FOR WORKING PAIRS

The references from which the thermodynamic properties for the absorbents investigated in Chapter 2 are taken are shown in Table A.1. Absorbents for which thermophysical properties are available for the solution are listed as a single reference; absorbents for which solution properties were calculated by combination of component properties have references listed for each component.

Table A.1: Thermodynamic property references for investigated working pairs

Refrigerant	**Absorbent**	**VLE**	**Enthalpy**	**Density**
H_2O	[bmim][BF_4]	(Kim et al., 2004)	h_r: (Klein, 2015) h_{abs}: (Sanmamed et al., 2010) h_e: (Rebelo et al., 2004)	ρ_r: (Klein, 2015) ρ_{abs}: (Zhou et al., 2006)
H_2O	[bmpyr][DCA]	(Królikowska et al., 2014)	h_r: (Klein, 2015) h_{abs}: (González et al., 2013) h_e: (Królikowska et al., 2014)	ρ_r: (Klein, 2015) ρ_{abs}: (Królikowska et al., 2014)
H_2O	[emim][Ac]	(Guo et al., 2012)	h_r: (Klein, 2015) h_{abs}: (Römich et al., 2012) h_e: -	(Quijada-Maldonado et al., 2012)
H_2O	[emim][DEP]	(Zhao et al., 2006)	h_r: (Klein, 2015) h_{abs}: (Ficke et al., 2010) h_e: (Ficke et al., 2010)	ρ_r: (Klein, 2015) ρ_{abs}: (Ficke et al., 2010)
H_2O	[emim][DMP]	(Ren et al., 2011)	h_{sol}: (Ren et al., 2011) h_e: (Ren et al., 2011)	(Gong et al., 2012)
H_2O	[emim][BF_4]	(Seiler et al., 2004)	h_r: (Klein, 2015) h_{abs}: (Sanmamed et al., 2010) h_e: (Yokozeki and Shiflett, 2010)	ρ_r: (Klein, 2015) ρ_{abs}: (Zhang et al., 2004)

Table A.1 continued

Refrigerant	**Absorbent**	**VLE**	**Enthalpy**	**Density**
H_2O	LiBr	(Klein, 2015)	(Klein, 2015)	(Klein, 2015)
H_2O	LiBr+$ZnBr_2$+LiCl (33:59:8)	(Iyoki and Uemura, 1990)	h_{sol}: (Iyoki and Uemura, 1990) h_e: (Iyoki and Uemura, 1990)	(Iyoki and Uemura, 1990)
H_2O	[mmim][DMP]	(Dong et al., 2012)	h_{sol}: (Dong et al., 2012) h_e: (He et al., 2010)	(He et al., 2010)
H_2O	NaOH	(Ruiter, 1990)	h_{sol}: (Ruiter, 1990) h_e: (Ruiter, 1990)	-
H_2O	NaOH+KOH+CsOH (10:9:6)	(Herold et al., 1991)	(Herold et al., 1991)	-

APPENDIX B. SAMPLE CALCULATIONS

In this appendix, the details of the calculations conducted on the data collected in the proof-of-concept demonstration are detailed for a single data point. The data point chosen is one logged at 2:38:26 PM on 26 March 2021 during the steady-state portion of a high-pressure test. During the low-pressure portion of this test, synthetic graywater was used as the feed.

B.1 Coupling Fluid Heat Transfer Calculations

The heat transfer rate for the coupling fluid in the desorber is

$$\dot{Q}_{f,cf} = \dot{m}_{f,cf} c_{p,w} \left(T_{f,cf,in} - T_{f,cf,out}\right) \tag{B.1}$$

The raw data associated with the temperature and mass flow rate are as follows

Table B.1: Measured values for coupling fluid heat transfer calculations

Quantity	Measured Value	Standard Deviation
$\dot{m}_{f,cf}$	279.7 g min^{-1}	0.8 g min^{-1}
$T_{f,cf,in}$	105.9°C	0°C
$T_{f,cf,out}$	89.0°C	0°C

Using these data, the specific heat capacity can be calculated at the average of the inlet and outlet temperatures.

$$c_{p,w} = c_p \left(\frac{T_{f,cf,in} + T_{f,cf,out}}{2}, x = 0\right) = 4.213 \text{ J g}^{-1}\text{K}^{-1} \tag{B.2}$$

Substituting this value and the values from Table B.1 into Equation B.1 yields the coupling fluid heat transfer rate.

$$\dot{Q}_{f,cf} = \frac{279.7 \text{ g min}^{-1}}{60 \text{ s min}^{-1}} \times 4.213 \text{ J g}^{-1}\text{K}^{-1} \times (105.9℃ - 89.0℃) \tag{B.3}$$

$$= 331.4 \text{ W}$$

The uncertainties associated with the measured values can be calculated by combining the systematic and random uncertainties. The random uncertainty for the mass flow rate is

$$\begin{aligned} U_{rand,\dot{m}_{f,cf}} &= \frac{t(0.95,25)s}{\sqrt{N}} \\ &= 2.06 \times \frac{0.8 \text{ g min}^{-1}}{\sqrt{25}} \\ &= 0.28 \text{ g min}^{-1} \end{aligned} \tag{B.4}$$

The random uncertainty can be combined with the systematic uncertainty to determine the total uncertainty as follows for the mass flow rate

$$\begin{aligned} U_{\dot{m}_{f,cf}} &= \sqrt{U_{rand,\dot{m}_{f,cf}}^2 + U_{sys,\dot{m}_{f,cf}}^2} \\ &= \sqrt{(0.28 \text{ g mi}^{-1})^2 + (0.0015 \times 279.7 \text{ g min}^{-1})^2} \\ &= 0.50 \text{ g min}^{-1} \end{aligned} \tag{B.5}$$

The systematic and total uncertainties for each of the measurements in Table B.1 are given in Table B.2.

Table B.2: Systematic, random, and total uncertainties of measured quantities for coupling fluid heat transfer calculations

Quantity	Systematic Uncertainty	Random Uncertainty	Total Uncertainty
$\dot{m}_{f,cf}$	±0.42 g min^{-1}	±0.28 g min^{-1}	±0.50 g min^{-1}
$T_{f,cf,in}$	±0.25°C	±0°C	±0.25°C
$T_{f,cf,out}$	±0.25°C	±0°C	±0.25°C

The uncertainty in the heat transfer rate is calculated as follows. The uncertainty of the specific heat capacity when calculated using the uncertainties in the temperatures and

the error propagation function in Engineering Equation Solver is less than 0.005% of the value; therefore, this term is neglected.

$$U_{\dot{Q}_{f,cf}} = \left[\left(c_{p,w}\left(T_{f,cf,in} - T_{f,cf,out}\right)U_{\dot{m}_{f,cf}}\right)^2 + \left(\dot{m}_{f,cf}c_{p,w}U_{T_{f,cf,in}}\right)^2 + \left(\dot{m}_{f,cf}c_{p,w}U_{T_{f,cf,out}}\right)^2\right]^{\frac{1}{2}} \quad \text{(B.6)}$$

$$= 6.9 \text{ W}$$

B.2 Solution Heat Transfer Calculations

The heat transfer in the LiBr solution flowing over the tubes of the desorber can be calculated by

$$\dot{Q}_{f,soln} = \dot{m}_{soln,out}h_{soln,out} + \left(\dot{m}_{soln,in} - \dot{m}_{soln,out}\right)h_v - \dot{m}_{soln,in}h_{in} \quad \text{(B.7)}$$

where

$$h = h(T, w) \quad \text{(B.8)}$$

and

$$\dot{m}_{soln,out} = \frac{\dot{m}_{soln,in}w_{in}}{w_{out}} \quad \text{(B.9)}$$

The solution concentration is calculated from the measured density and temperature by solving for the negative root of

$$0 = \left(V_0 + V_3T + V_6T^2 - \frac{1}{\rho}\right) + (V_1 + V_4T + V_7T^2)w + (V_2 + V_5T)w^2 \quad \text{(B.10)}$$

where the coefficients, V_i, are taken from the work of Yuan and Herold (2005).

The measured values used to calculate the heat transfer coefficient are shown in Table B.3, along with their uncertainties, which are calculated following the method

Table B.3: Measured values and uncertainties for solution heat transfer calculation

Quantity	Value	Systematic Uncertainty	Random Uncertainty	Total Uncertainty
$\dot{m}_{soln,in}$	96.6 g min^{-1}	±0.097 g min^{-1}	±0.32 g min^{-1}	±0.34 g min^{-1}
$T_{w,in}$	66.1°C	±0.25°C	±0°C	±0.25°C
ρ_{in}	1593.9 kg m^{-3}	±2 kg m^{-3}	±1.7 kg m^{-3}	±2.6 kg m^{-3}
$T_{soln,in}$	81.9°C	±0.25°C	±0°C	±0.25°C
$T_{w,out}$	70.0°C	±0.25°C	±0°C	±0.25°C
ρ_{in}	1668.6 kg m^{-3}	±2 kg m^{-3}	±1.3 kg m^{-3}	±2.4 kg m^{-3}
$T_{soln,in}$	93.5°C	±0.25°C	±0°C	±0.25°C
p	1.78 psia	±0.001 psia	±0.01 psia	±0.01 psia

outlined above. $T_{w,in}$ and $T_{w,out}$ are the temperatures measured at the outlet of the Coriolis flow meters and are used in the concentration calculations as shown below.

The inlet concentration is calculated as follows. Equation B.10 can be rewritten as

$$0 = A_{in} w_{in}^2 + B_{in} w_{in} + C_{in} \tag{B.11}$$

where

$$A_{in} = [-1.70 \times 10^{-8} + (5.82 \times 10^{-11}\ \mathrm{K^{-1}}) \times 339.25\ \mathrm{K}]\ \mathrm{wt\%^{-2}}$$

$$= 2.77 \times 10^{-9}\ \mathrm{wt\%^{-2}}$$

$$B_{in} = [-1.00 \times 10^{-5} + (2.54 \times 10^{-8}\ \mathrm{K^{-1}}) \times 339.25\ \mathrm{K} - (5.13 \times 10^{-11}\mathrm{K^{-2}}) \times (339.25\ \mathrm{K})^2]\ \mathrm{wt\%^{-1}}$$

$$= -7.32 \times 10^{-6}\ \mathrm{wt\%^{-1}}$$

$$C_{in} = \left[1.18 \times 10^{-3} - (1.50 \times 10^{-6}\ \mathrm{K^{-1}}) \times 339.25\ \mathrm{K} + (3.06 \times 10^{-9}\mathrm{K^{-2}}) \times (339.25\ \mathrm{K})^2 + \frac{\mathrm{kg\ m^{-3}}}{1593.9\ \mathrm{kg\ m^{-3}}}\right]$$

$$= 3.93 \times 10^{-4}$$

The quadratic equation can be solved by

$$w_{in} = \frac{-B_{in} - \sqrt{B_{in}^2 - 4A_{in}C_{in}}}{2A_{in}}$$

$$= \frac{7.32 \times 10^{-6} - \sqrt{(7.32 \times 10^{-6})^2 - 4(2.77 \times 10^{-9})(3.93 \times 10^{-4})}}{2(2.77 \times 10^{-9})} \quad \text{(B.12)}$$

$$= 54.89 \text{ wt\%}$$

Uncertainties in the concentration were calculated using

$$U_w = \sqrt{\left(\frac{\partial w}{\partial \rho} U_\rho\right)^2 + \left(\frac{\partial w}{\partial T} U_T\right)^2} \quad \text{(B.13)}$$

with the partial derivatives estimated numerically as follows.

$$\frac{\partial w}{\partial \rho} = 0.05 \text{ wt\% m}^3 \text{ kg}^{-1}$$

$$\frac{\partial w}{\partial T} = 0.03 \text{ wt\% K}^{-1}$$

With these, the uncertainty in the inlet concentration can be calculated as

$$U_{w_{in}} = \{[(0.05 \text{ wt\% m}^3 \text{ kg}^{-1})(2.6 \text{ kg m}^{-3})]^2 + [(0.03 \text{ wt\% K}^{-1})(0.25 \text{ K})]^2\}^{\frac{1}{2}} \quad \text{(B.14)}$$

$$= 0.13 \text{ wt\%}$$

Using the same process, the outlet concentration can be calculated as 59.03 ± 0.12 wt%.

With these concentrations calculated, the outlet solution flow rate can be calculated.

$$\dot{m}_{soln,out} = \frac{(96.6 \text{ g min}^{-1})(54.89 \text{ wt\%})}{59.03 \text{ wt\%}} = 89.8 \text{ g min}^{-1} \quad \text{(B.15)}$$

The uncertainty of the solution outlet flow rate is

$$U_{\dot{m}_{soln,out}} = \left[\left(\frac{w_{in}}{w_{out}} U_{\dot{m}_{soln,in}}\right)^2 + \left(\frac{\dot{m}_{soln,in}}{w_{out}} U_{w_{in}}\right)^2 + \left(-\frac{\dot{m}_{soln,in} w_{in}}{w_{out}^2} U_{w_{out}}\right)^2\right]^{\frac{1}{2}}$$

$$= \left[\left(\frac{54.89\ \text{wt\%}}{59.03\ \text{wt\%}}(0.34\ \text{g min}^{-1})\right)^2 + \left(\frac{0.34\ \text{g min}^{-1}}{59.03\ \text{wt\%}}(0.13\ \text{wt\%})\right)^2 + \left(-\frac{(0.34\ \text{g min}^{-1})(54.89\ \text{wt\%})}{(59.03\ \text{wt\%})^2}(0.12\ \text{wt\%})\right)^2\right]^{\frac{1}{2}} \quad \text{(B.16)}$$

$$= 0.42\ \text{g min}^{-1}$$

The enthalpies and their respective uncertainties are calculated using Engineering Equation Solver. The vapor enthalpy is calculated at the average of the solution inlet and outlet temperatures. The results of the calculation are shown in Table B.4.

Table B.4: Enthalpies and uncertainties for solution heat transfer calculations

Quantity	Value	Uncertainty
$h_{soln,in}$	79.27 J g^{-1}	±0.59 J g^{-1}
$h_{soln,out}$	114.1 J g^{-1}	±0.64 J g^{-1}
h_v	2664 J g^{-1}	±0.34 J g^{-1}

The relative uncertainty on the vapor enthalpy is less than 0.01%; therefore, it is neglected when calculating the uncertainty in the solution heat transfer rate. The solution heat transfer rate is

$$\dot{Q}_{f,soln} = \dot{m}_{soln,out} h_{soln,out} + (\dot{m}_{soln,in} - \dot{m}_{soln,out}) h_v - \dot{m}_{soln,in} h_{in} \quad \text{(B.17)}$$

$$= \frac{89.8\ \text{g min}^{-1}}{60\ \text{s min}^{-1}}(114.1\ \text{J g}^{-1})$$

$$+ \frac{96.6\ \text{g mi}^{-1} - 89.8\ \text{g mi}^{-1}}{60\ \text{s mi}^{-1}}(2664\ \text{J g}^{-1})$$

$$- (96.6\ \text{g min}^{-1})(79.27\ \text{J g}^{-1})$$

$$= 345\ \text{W}$$

To calculate the uncertainty in the solution heat transfer rate, first, the expression for the outlet mass flow rate is substituted into the expression for the heat transfer rate.

$$\dot{Q}_{f,soln} = \frac{\dot{m}_{soln,in} w_{in}}{w_{out}} h_{soln,out} + \dot{m}_{soln,in}\left(1 - \frac{w_{in}}{w_{out}}\right) h_v - \dot{m}_{soln,in} h_{soln,in} \tag{B.18}$$

The uncertainty can then be calculated as follows.

$$U_{\dot{Q}_{f,soln}} = \left\{ \left[\left(\frac{w_{in}}{w_{out}} h_{soln,out} + \left(1 - \frac{w_{in}}{w_{out}}\right) h_v - h_{soln,in} \right) U_{\dot{m}_{soln,in}} \right]^2 + \left[\left(\frac{\dot{m}_{soln,in}}{w_{out}} h_{soln,out} - \frac{\dot{m}_{soln,in}}{w_{out}} h_v \right) U_{w_{in}} \right]^2 + \left[\left(-\frac{\dot{m}_{soln,in} w_{in}}{w_{out}^2} h_{soln,out} + \frac{\dot{m}_{soln,in} w_{in}}{w_{out}^2} h_v \right) U_{w_{out}} \right]^2 + \left[\frac{\dot{m}_{soln,in} w_{in}}{w_{out}} U_{h_{soln,out}} \right]^2 + \left[-\dot{m}_{soln,in} U_{h_{soln,in}} \right]^2 \right\}^{\frac{1}{2}} \tag{B.19}$$

$$= 12.8\ \text{W}$$

APPENDIX C. TURBINE FLOW METER TEMPERATURE CORRECTION

The frequency of rotation of the turbines in the turbine flow meters used in the heat transfer-fluid loops is affected by the temperature of the water flowing through them. Therefore, a Roshko-Strouhal correction is applied to the turbine flow meters as suggested by Mattingly (1992).

The Roshko number is

$$Ro = \frac{fd^2}{\nu} \tag{C.1}$$

where f is the frequency of the turbine, d is the diameter of the flow meter corrected for temperature, and ν is the kinematic viscosity of the fluid. The Strouhal number is a dimensionless number that relates flow velocity to frequency in oscillatory flows and is given by

$$St = \frac{fd}{u} \tag{C.2}$$

where u is the velocity of the fluid.

The frequency of the turbine is determined using the K-factor on the turbine meter, which is defined by the manufacturer as

$$K = \frac{f}{\dot{V}} \tag{C.3}$$

where $\dot{V}$ is the volumetric flow rate in gallons per second.

The K-factor is correlated to the volumetric flow rate in gallons *per minute* logarithmically. The constants for this equation are provided by the manufacturer.

Table C.1: Temperature correction parameters for turbine flow meters

Loop	Meter S/N	a_K	b_K	a_{St}	b_{St}	R^2	AAD
1	150609M44325	127408	1295556	44.42	-153.94	0.994	0.44%
2	150609M44327	123207	1283662	42.76	-124.93	0.988	0.41%
3	150609M44328	128210	1299057	46.31	-165.97	0.994	0.61%
4	150609M44326	120745	1278996	44.08	-145.68	0.992	0.35%

$$K = a_K \ln(\dot{V}) + b_K \tag{C.4}$$

The effect of temperature on the apparent flow rate for water in the turbine flow meters was determined by flowing water at a specified temperature and flow rate through the turbine flow meter and through a Coriolis flow meter (MicroMotion CMFS010M). For the heated loops, temperatures between 25 and 50°C were used. For the cooled loops, temperatures between 4.5 and 25°C were used. The Roshko and Strouhal numbers were calculated, and a correlation of the form

$$St = a_{St} \ln(Ro) + b_{St} \tag{C.5}$$

was fit to the resulting data. Table C.1 shows the constants for the K-factor and Strouhal number equations, along with two goodness-of-fit parameters: the coefficient of determination (R^2) of the Roshko-Strouhal number correlation and the average absolute deviation (AAD) between the measured flow rates and those predicted by the correlation. The flow meters on loops 3 and 4 are used in the experiments discussed in this work.

APPENDIX D. LOW-CONCENTRATION SALT SOLUTION CONDUCTIVITY CURVES

Electrical conductivity curves were generated for low-concentration solutions of LiBr and NaCl to determine the concentration of these salts in the distillate after the water purification experiments.

Table D.1: Conductivity data for NaCl

Mass Fraction NaCl	**Conductivity (μS cm^{-1})**
5×10^{-6}	11
5×10^{-6}	12
1×10^{-5}	24
1×10^{-5}	25
2×10^{-5}	45
2×10^{-5}	46
5×10^{-5}	101
5×10^{-5}	104
0.0001	191
0.0001	194
0.0002	382
0.0002	393
0.0005	962
0.0005	981
0.001	1872
0.001	1926
0.002	3860
0.002	3970
0.005	9700
0.005	10030
0.01	19640
0.01	20400
0.02	38900
0.02	39400

D.1 NaCl Concentration Curve

The NaCl concentration curve was generated using anhydrous NaCl (Sigma Aldrich, ≥99%) dissolved in distilled water produced by the lab distiller (Running Waters, Inc., Model A15). The data points used to generate the curve are as given in Table D.1.

Fitting a linear curve to the data yields

$$\sigma = 1.9656 \times 10^6 w + 12.7 \tag{D.1}$$

with an R^2 of 0.9997.

D.2 LiBr Concentration Curve

The LiBr concentration curve was generated using anhydrous NaCl (Sigma Aldrich, ≥99%) dissolved in distilled water produced by the lab distiller (Running Waters, Inc., Model A15). The data points used to generate the curve are as given in Table D.2.

Fitting a linear curve to the data yields

$$\sigma = 1.0468 \times 10^6 w + 15.4 \tag{D.2}$$

with an R^2 of 0.9996.

Table D.2: Conductivity data for LiBr

Mass Fraction LiBr	**Conductivity (μS cm^{-1})**
2×10^{-5}	29.5
2×10^{-5}	30.7
5×10^{-5}	62.3
5×10^{-5}	64.8
0.0001	110.7
0.0001	113.0
0.0002	221.8
0.0002	230.0
0.0002	230.1
0.0005	553.9
0.0005	571.4
0.001	1095
0.001	1047
0.002	2048
0.002	2117
0.003	3098
0.003	3196
0.004	4169
0.004	4256

REFERENCES

Abdelmoez, W., M. S. Mahmoud and T. E. Farrag (2014), "Water Desalination Using Humidification/Dehumidification (HDH) Technique Powered by Solar Energy: A Detailed Review," *Desalination and Water Treatment*. Vol. 52(25-27), pp. 4622-4640 DOI: 10.1080/19443994.2013.804457.

Abdulrahim, H. K. and M. A. Darwish (2015), "Thermal Desalination and Air Conditioning Using Absorption Cycle," *Desalination and Water Treatment*. Vol. 55(12), pp. 3310-3329 DOI: 10.1080/19443994.2014.939492.

Achilli, A., T. Y. Cath and A. E. Childress (2010), "Selection of Inorganic-Based Draw Solutions for Forward Osmosis Applications," *Journal of Membrane Science*. Vol. 364(1-2), pp. 233-241 DOI: 10.1016/j.memsci.2010.08.010.

Achilli, A., T. Y. Cath, E. A. Marchand and A. E. Childress (2009), "The Forward Osmosis Membrane Bioreactor: A Low Fouling Alternative to MBR Processes," *Desalination*. Vol. 239(1-3), pp. 10-21 DOI: 10.1016/j.desal.2008.02.022.

AHRI (2017). *2017 Standard for Performance Rating of Unitary Air-Conditioning and Air-Source Heat Pump Equipment*.

Alkhudhiri, A., N. Darwish and N. Hilal (2012), "Membrane Distillation: A Comprehensive Review," *Desalination*. Vol. 287, pp. 2-18 DOI: 10.1016/j.desal.2011.08.027.

Alsaman, A. S., A. A. Askalany, K. Harby and M. S. Ahmed (2017), "Performance Evaluation of a Solar-Driven Adsorption Desalination-Cooling System," *Energy*. Vol. 128, pp. 196-207 DOI: 10.1016/j.energy.2017.04.010.

Aprea, P., B. de Gennaro, N. Gargiulo, A. Peluso, B. Liguori, F. Iucolano and D. Caputo (2016), "Sr-, Zn- and Cd-Exchanged Zeolitic Materials as Water Vapor Adsorbents for Thermal Energy Storage Applications," *Applied Thermal Engineering*. Vol. 106, pp. 1217-1224 DOI: 10.1016/j.applthermaleng.2016.06.066.

Babadi, F. and B. Farhanieh (2005), "Characteristics of Heat and Mass Transfer in Vapor Absorption of Falling Film Flow on a Horizontal Tube," *International Communications in Heat and Mass Transfer*. Vol. 32(9), pp. 1253-1265 DOI: 10.1016/j.icheatmasstransfer.2005.05.011.

Belghazi, M., A. Bontemps, J. C. Signe and C. Marvillet (2001), "Condensation Heat Transfer of a Pure Fluid and Binary Mixture Outside a Bundle of Smooth

Horizontal Tubes. Comparison of Experimental Results and a Classical Model," *International Journal of Refrigeration*. Vol. 24(8), pp. 841-855 DOI: 10.1016/S0140-7007(00)00037-2.

Beysens, D. and I. Milimouk (2001), "Alternative Freshwater Resources," *Sécheresse*. Vol. 11(4), pp. 281-288.

Bock, B. D., J. P. Meyer and J. R. Thome (2019), "Falling Film Boiling and Pool Boiling on Plain Circular Tubes: Influence of Surface Roughness, Surface Material and Saturation Temperature on Heat Transfer and Dryout," *Experimental Thermal and Fluid Science*. Vol. 109, p. 109870 DOI: 10.1016/j.expthermflusci.2019.109870.

Boman, D. B., D. C. Hoysall, M. A. Staedter, A. Goyal, M. J. Ponkala and S. Garimella (2017), "A Method for Comparison of Absorption Heat Pump Working Pairs," *International Journal of Refrigeration*. Vol. 77, pp. 149-175 DOI: 10.1016/j.ijrefrig.2017.02.023.

Bonneau, C., C. Josset, V. Melot and B. Auvity (2019), "Comprehensive Review of Pure Vapour Condensation Outside of Horizontal Smooth Tubes," *Nuclear Engineering and Design*. Vol. 349, pp. 92-108 DOI: 10.1016/j.nucengdes.2019.04.005.

Browne, M. W. and P. K. Bansal (1999), "An Overview of Condensation Heat Transfer on Horizontal Tube Bundles," *Applied Thermal Engineering*. Vol. 19(6), pp. 565-594 DOI: 10.1016/S1359-4311(98)00055-6.

Bustamante, J. G. and S. Garimella (2014), "Dominant Flow Mechanisms in Falling-Film and Droplet-Mode Evaporation over Horizontal Rectangular Tube Banks," *International Journal of Refrigeration*. Vol. 43, pp. 80-89 DOI: 10.1016/j.ijrefrig.2014.03.010.

Bustamante, J. G. and S. Garimella (2019), "Experimental Assessment of Flow Distributors for Falling-Films over Horizontal Tube Banks," *International Journal of Refrigeration*. Vol. 101, pp. 24-33 DOI: 10.1016/j.ijrefrig.2019.02.025.

Bustamante, J. G., S. Garimella and M. Hughes (2020), "Falling-Film Evaporation over Horizontal Rectangular Tubes: Part I—Experimental Results," *International Journal of Refrigeration*. Vol. 119, pp. 37-47.

Cai, Y. and X. M. Hu (2016), "A Critical Review on Draw Solutes Development for Forward Osmosis," *Desalination*. Vol. 391, pp. 16-29 DOI: 10.1016/j.desal.2016.03.021.

Cammenga, H. K., F. W. Schulze and W. Theuerl (1977), "Vapor Pressure and Evaporation Coefficient of Glycerol," *Journal of Chemical & Engineering Data*. Vol. 22(2), pp. 131-134 DOI: 10.1021/je60073a004.

Cath, T. Y., D. Adams and A. E. Childress (2005), "Membrane Contactor Processes for Wastewater Reclamation in Space," *Journal of Membrane Science*. Vol. 257(1-2), pp. 111-119 DOI: 10.1016/j.memsci.2004.07.039.

Cath, T. Y., A. E. Childress and M. Elimelech (2006), "Forward Osmosis: Principles, Applications, and Recent Developments," *Journal of Membrane Science*. Vol. 281(1-2), pp. 70-87 DOI: 10.1016/j.memsci.2006.05.048.

Cess, R. and M. Lian (1976), "A Simple Parameterization for the Water Vapor Emissivity."

Chiranjeevi, C. and T. Srinivas (2014), "Combined Two Stage Desalination and Cooling Plant," *Desalination*. Vol. 345, pp. 56-63 DOI: 10.1016/j.desal.2014.04.023.

Chiranjeevi, C. and T. Srinivas (2016), "Experimental Analysis of Augmented Desalination by Cooling Integration," *Energy Procedia*. Vol. 90, pp. 283-291 DOI: 10.1016/j.egypro.2016.11.196.

Chiranjeevi, C. and T. Srinivas (2017), "Augmented Desalination with Cooling Integration," *International Journal of Refrigeration*. Vol. 80, pp. 106-119 DOI: 10.1016/j.ijrefrig.2017.05.007.

Churchill, S. W. and H. H. S. Chu (1975), "Correlating Equations for Laminar and Turbulent Free Convection from a Horizontal Cylinder," *International Journal of Heat and Mass Transfer*. Vol. 18(9), pp. 1049-1053 DOI: 10.1016/0017-9310(75)90222-7.

Chyu, M.-C. and A. E. Bergles (1987), "An Analytical and Experimental Study of Falling-Film Evaporation on a Horizontal Tube," *Journal of Heat Transfer*. Vol. 109(4), pp. 983-990 DOI: 10.1115/1.3248214.

Corcione, M. (2005), "Correlating Equations for Free Convection Heat Transfer from Horizontal Isothermal Cylinders Set in a Vertical Array," *International Journal of Heat and Mass Transfer*. Vol. 48(17), pp. 3660-3673 DOI: 10.1016/j.ijheatmasstransfer.2005.01.010.

de Lange, M. F., K. J. F. M. Verouden, T. J. H. Vlugt, J. Gascon and F. Kapteijn (2015), "Adsorption-Driven Heat Pumps: The Potential of Metal–Organic Frameworks," *Chemical Reviews*. Vol. 115(22), pp. 12205-12250 DOI: 10.1021/acs.chemrev.5b00059.

DeOreo, W. B., P. Mayer, B. Dziegielewski and J. Kiefer (2016). "Residential End Uses of Water, Version 2: Executive Report," Water Research Foundation, Denver, CO, Report, 4309A.

Determan, M. D. (2005). *Experimental and Analytical Investigation of Ammonia-Water Desorption in Microchannel Geometries*. Georgia Institute of Technology, Atlanta, GA.

Dong, L., D. Zheng, N. Nie and Y. Li (2012), "Performance Prediction of Absorption Refrigeration Cycle Based on the Measurements of Vapor Pressure and Heat Capacity of H_2O+[DMIM]DMP System," *Applied Energy*. Vol. 98, pp. 326-332 DOI: 10.1016/j.apenergy.2012.03.044.

Drioli, E., A. Ali and F. Macedonio (2015), "Membrane Distillation: Recent Developments and Perspectives," *Desalination*. Vol. 356, pp. 56-84 DOI: 10.1016/j.desal.2014.10.028.

El-Dessouky, H. T., H. M. Ettouney and Y. Al-Roumi (1999), "Multi-Stage Flash Desalination: Present and Future Outlook," *Chemical Engineering Journal*. Vol. 73(2), pp. 173-190 DOI: 10.1016/S1385-8947(99)00035-2.

Elattar, H. F., A. Fouda and S. A. Nada (2016), "Performance Investigation of a Novel Solar Hybrid Air Conditioning and Humidification–Dehumidification Water Desalination System," *Desalination*. Vol. 382, pp. 28-42 DOI: 10.1016/j.desal.2015.12.023.

Elshamarka, S. (1991), "Absorption Heat Pump for a Potable Water Supply in a Solar House," *Applied Energy*. Vol. 40(1), pp. 31-40 DOI: 10.1016/0306-2619(91)90048-3.

Ettouney, H. (2005), "Brine Entrainment in Multistage Flash Desalination," *Desalination*. Vol. 182(1-3), pp. 87-97 DOI: 10.1016/j.desal.2005.04.011.

FAO (2016). "Aquastat Core Database," Food and Agriculture Organization of the United Nations, 2019-04-20 http://www.fao.org/aquastat/en/databases/maindatabase/.

Fathalah, K. and S. E. Aly (1991), "Theoretical Study of a Solar Powered Absorption/MED Combined System," *Energy Conversion and Management*. Vol. 31(6), pp. 529-544 DOI: 10.1016/0196-8904(91)90088-Z.

Fernández-Seara, J. and Á. Á. Pardiñas (2014), "Refrigerant Falling Film Evaporation Review: Description, Fluid Dynamics and Heat Transfer," *Applied Thermal Engineering*. Vol. 64(1-2), pp. 155-171 DOI: 10.1016/j.applthermaleng.2013.11.023.

Ficke, L. E., R. R. Novak and J. F. Brennecke (2010), "Thermodynamic and Thermophysical Properties of Ionic Liquid + Water Systems," *Journal of Chemical & Engineering Data*. Vol. 55(11), pp. 4946-4950 DOI: 10.1021/je100522z.

Fouda, A., S. A. Nada and H. F. Elattar (2016), "An Integrated A/C and HDH Water Desalination System Assisted by Solar Energy: Transient Analysis and Economical Study," *Applied Thermal Engineering*. Vol. 108, pp. 1320-1335 DOI: 10.1016/j.applthermaleng.2016.08.026.

Fujita, T. (1993), "Falling Liquid Films in Absorption Machines," *International Journal of Refrigeration*. Vol. 16(4), pp. 282-294 DOI: 10.1016/0140-7007(93)90081-I.

Fujita, Y. and M. Tsutsui (1998), "Experimental Investigation of Falling Film Evaporation on Horizontal Tubes," *Heat Transfer - Japanese Research*. Vol. 27(8), pp. 609-618 DOI: 10.1002/(sici)1520-6556(1998)27:8<609::aid-htj5>3.0.co;2-n.

Ghaffour, N., T. M. Missimer and G. L. Amy (2013), "Technical Review and Evaluation of the Economics of Water Desalination: Current and Future Challenges for Better Water Supply Sustainability," *Desalination*. Vol. 309, pp. 197-207 DOI: 10.1016/j.desal.2012.10.015.

Ghalavand, Y., M. S. Hatamipour and A. Rahimi (2015), "A Review on Energy Consumption of Desalination Processes," *Desalination and Water Treatment*. pp. 1-16 DOI: 10.1080/19443994.2014.892837.

Gleick, P. H. (1996), "Basic Requirements for Human Activities: Meeting Basic Needs," *Water International*. Vol. 21(2), pp. 83-92.

Gleick, P. H. (2003), "Global Freshwater Resources: Soft-Path Solutions for the 21st Century," *Science*. Vol. 302(5650), pp. 1524-1528 DOI: 10.1126/science.1089967.

Goel, N. and D. Y. Goswami (2007), "Experimental Verification of a New Heat and Mass Transfer Enhancement Concept in a Microchannel Falling Film Absorber," *Journal of Heat Transfer*. Vol. 129(2), pp. 154-161 DOI: 10.1115/1.2402182.

Gogonin, I. I. and A. R. Dorokhov (1976), "Experimental Investigation of Heat Transfer with the Condensation of the Moving Vapor of Freon-21 on Horizontal Cylinders," *Journal of Applied Mechanics and Technical Physics*. Vol. 17(2), pp. 252-257 DOI: 10.1007/BF00858419.

Gong, Y.-H., C. Shen, Y.-Z. Lu, H. Meng and C.-X. Li (2012), "Viscosity and Density Measurements for Six Binary Mixtures of Water (Methanol or Ethanol) with an Ionic Liquid ([BMIM][DMP] or [EMIM][DMP]) at Atmospheric Pressure in the Temperature Range of (293.15 to 333.15) K," *Journal of Chemical & Engineering Data*. Vol. 57(1), pp. 33-39 DOI: 10.1021/je200600p.

González, E. J., B. González and E. A. Macedo (2013), "Thermophysical Properties of the Pure Ionic Liquid 1-Butyl-1-Methylpyrrolidinium Dicyanamide and Its Binary Mixtures with Alcohols," *Journal of Chemical & Engineering Data*. Vol. 58(6), pp. 1440-1448 DOI: 10.1021/je300384g.

Grant, S. B., J.-D. Saphores, D. L. Feldman, A. J. Hamilton, T. D. Fletcher, P. L. M. Cook, M. Stewardson, B. F. Sanders, L. A. Levin, R. F. Ambrose, A. Deletic, R. Brown, S. C. Jiang, D. Rosso, W. J. Cooper and I. Marusic (2012), "Taking the "Waste" out of "Wastewater" for Human Water Security and Ecosystem Sustainability," *Science*. Vol. 337(6095), pp. 681-686 DOI: 10.1126/science.1216852.

Green, D. W. and R. H. Perry (2008). *Perry's Chemical Engineers' Handbook, Eighth Edition*. 8th ed. / Ed. McGraw-Hill Education, New York.

Gude, V. G. and N. Nirmalakhandan (2008), "Combined Desalination and Solar-Assisted Air-Conditioning System," *Energy Conversion and Management*. Vol. 49(11), pp. 3326-3330 DOI: 10.1016/j.enconman.2008.03.030.

Guiñon, J. L., J. Garcia-Anton, V. Pérez-Herranz and G. Lacoste (1994), "Corrosion of Carbon Steels, Stainless Steels, and Titanium in Aqueous Lithium Bromide Solution," *Corrosion*. Vol. 50(3), pp. 240-246 DOI: 10.5006/1.3293516.

Guo, K., Y. Bi, L. Sun, H. Su and L. Hungpu (2012), "Experiment and Correlation of Vapor–Liquid Equilibrium of Aqueous Solutions of Hydrophilic Ionic Liquids: 1-Ethyl-3-Methylimidazolium Acetate and 1-Hexyl-3-Methylimidazolium Chloride," *Journal of Chemical & Engineering Data*. Vol. 57(8), pp. 2243-2251 DOI: 10.1021/je3001987.

He, Y., Q. Bi, J. Zhang and H. Hou (2011), "Experimental Study on the Heat Transfer Characteristics of an Evaporating Falling Film on a Horizontal Plain Tube," *Heat Transfer Engineering*. Vol. 32(11-12), pp. 936-942 DOI: 10.1080/01457632.2011.556354.

He, Z., Z. Zhao, X. Zhang and H. Feng (2010), "Thermodynamic Properties of New Heat Pump Working Pairs: 1,3-Dimethylimidazolium Dimethylphosphate and Water, Ethanol and Methanol," *Fluid Phase Equilibria*. Vol. 298(1), pp. 83-91 DOI: 10.1016/j.fluid.2010.07.005.

Henninger, S. K., F. Jeremias, H. Kummer and C. Janiak (2012), "Mofs for Use in Adsorption Heat Pump Processes," *European Journal of Inorganic Chemistry*. Vol. 2012(16), pp. 2625-2634 DOI: 10.1002/ejic.201101056.

Herold, K. E., R. Radermacher, L. Howe and D. C. Erickson (1991), "Development of an Absorption Heat Pump Water Heater Using an Aqueous Ternary Hydroxide Working Fluid," *International Journal of Refrigeration*. Vol. 14(3), pp. 156-167 DOI: 10.1016/0140-7007(91)90070-W.

Herold, K. E., R. Radermacher and S. A. Klein (1996). *Absorption Chillers and Heat Pumps*. CRC Press, Boca Raton, FL.

Hewitt, G. F., G. L. Shires and T. R. Bott (1994). *Process Heat Transfer*. CRC Press, Boca Raton, FL.

Honda, H., B. Uchima, S. Nozu, H. Nakata and E. Torigoe (1991), "Film Condensation of R-113 on in-Line Bundles of Horizontal Finned Tubes," *Journal of Heat Transfer*. Vol. 113(2), pp. 479-486 DOI: 10.1115/1.2910586.

Hou, S., H. Li and H. Zhang (2008), "An Open Air–Vapor Compression Refrigeration System for Air-Conditioning and Desalination on Ship," *Desalination*. Vol. 222(1-3), pp. 646-655 DOI: 10.1016/j.desal.2007.01.190.

Hourlier, F., A. Masse, P. Jaouen, A. Lakel, C. Gerente, C. Faur and P. Le Cloirec (2010), "Formulation of Synthetic Greywater as an Evaluation Tool for Wastewater Recycling Technologies," *Environmental Technology*. Vol. 31(2), pp. 215-223 DOI: 10.1080/09593330903431547.

Hu, X. and A. M. Jacobi (1996a), "The Intertube Falling Film: Part 1—Flow Characteristics, Mode Transitions, and Hysteresis," *Journal of Heat Transfer*. Vol. 118(3), p. 616 DOI: 10.1115/1.2822676.

Hu, X. and A. M. Jacobi (1996b), "The Intertube Falling Film: Part 2—Mode Effects on Sensible Heat Transfer to a Falling Liquid Film," *Journal of Heat Transfer*. Vol. 118(3), p. 626 DOI: 10.1115/1.2822678.

Ibrahim, A. G. M. and I. Dincer (2015), "Experimental Performance Evaluation of a Combined Solar System to Produce Cooling and Potable Water," *Solar Energy*. Vol. 122, pp. 1066-1079 DOI: 10.1016/j.solener.2015.10.033.

Incropera, F. P. and D. P. DeWitt (1996). *Introduction to Heat Transfer*. 3rd ed Ed. Wiley, New York.

Isao, K. and I. Mamoru (1984), "Mechanistic Modeling of Pool Entrainment Phenomenon," *International Journal of Heat and Mass Transfer*. Vol. 27(11), pp. 1999-2014 DOI: 10.1016/0017-9310(84)90187-X.

Ishii, M. and M. A. Grolmes (1975), "Inception Criteria for Droplet Entrainment in Two-Phase Concurrent Film Flow," *AIChE Journal*. Vol. 21(2), pp. 308-318 DOI: 10.1002/aic.690210212.

Iyoki, S. and T. Uemura (1990), "Physical and Thermal Properties of the Water-Lithium Bromide-Zinc Bromide-Lithium Chloride System," *Proceedings of ASHRAE Annual Conference*, pp. 323-328.

Janghorban Esfahani, I., Y. T. Kang and C. Yoo (2014), "A High Efficient Combined Multi-Effect Evaporation–Absorption Heat Pump and Vapor-Compression Refrigeration Part 1: Energy and Economic Modeling and Analysis," *Energy*. Vol. 75, pp. 312-326 DOI: 10.1016/j.energy.2014.07.081.

Janghorban Esfahani, I. and C. Yoo (2014), "A Highly Efficient Combined Multi-Effect Evaporation-Absorption Heat Pump and Vapor-Compression Refrigeration Part 2: Thermoeconomic and Flexibility Analysis," *Energy*. Vol. 75, pp. 327-337 DOI: 10.1016/j.energy.2014.07.082.

Jani, S. (2012), "Simulation of Heat and Mass Transfer Process in Falling Film Single Tube Absorption Generator," *International Journal of Science and Engineering Investigation*. Vol. 1(3), pp. 79-84.

Jeong, S. and S. Garimella (2002), "Falling-Film and Droplet Mode Heat and Mass Transfer in a Horizontal Tube LiBr/Water Absorber," *International Journal of Heat and Mass Transfer*. Vol. 45(7), pp. 1445-1458 DOI: 10.1016/S0017-9310(01)00262-9.

Jeong, S. and S. Garimella (2005), "Optimal Design of Compact Horizontal Tube LiBr/Water Absorbers," *HVAC&R Research*. Vol. 11(1), pp. 27-44 DOI: 10.1080/10789669.2005.10391124.

Kalaiselvam, S., M. Udayakumar and S. Jeyasheela (2010), "Performance Analysis of an Integrative Unit for Air Conditioning and Desalination," *Desalination and Water Treatment*. Vol. 21(1-3), pp. 66-72 DOI: 10.5004/dwt.2010.1218.

Khalil, B., J. Adamowski, A. Shabbir, C. Jang, M. Rojas, K. Reilly and B. Ozga-Zielinski (2016), "A Review: Dew Water Collection from Radiative Passive Collectors to Recent Developments of Active Collectors," *Sustainable Water Resources Management*. Vol. 2(1), pp. 71-86 DOI: 10.1007/s40899-015-0038-z.

Khamooshi, M., K. Parham and U. Atikol (2013), "Overview of Ionic Liquids Used as Working Fluids in Absorption Cycles," *Advances in Mechanical Engineering*. Vol. 2013, pp. 1-7 DOI: 10.1155/2013/620592.

Killion, J. D. and S. Garimella (2001), "A Critical Review of Models of Coupled Heat and Mass Transfer in Falling-Film Absorption," *International Journal of Refrigeration*. Vol. 24(8), pp. 755-797 DOI: 10.1016/S0140-7007(00)00086-4.

Killion, J. D. and S. Garimella (2003a), "Gravity-Driven Flow of Liquid Films and Droplets in Horizontal Tube Banks," *International Journal of Refrigeration*. Vol. 26(5), pp. 516-526 DOI: 10.1016/S0140-7007(03)00009-4.

Killion, J. D. and S. Garimella (2003b), "A Review of Experimental Investigations of Absorption of Water Vapor in Liquid Films Falling over Horizontal Tubes," *HVAC&R Research*. Vol. 9(2), pp. 111-136 DOI: 10.1080/10789669.2003.10391060.

Kim, D. and M. H. Kim (1999), "Heat Transfer Enhancement Characteristics for Falling-Film Evaporation on Horizontal Enhanced Tubes with Aqueous LiBr Solution," *Journal of Enhanced Heat Transfer*. Vol. 6(1), pp. 61-69 DOI: 10.1615/JEnhHeatTransf.v6.i1.60.

Kim, H., S. R. Rao, E. A. Kapustin, L. Zhao, S. Yang, O. M. Yaghi and E. N. Wang (2018), "Adsorption-Based Atmospheric Water Harvesting Device for Arid Climates," *Nature Communications*. Vol. 9(1), p. 1191 DOI: 10.1038/s41467-018-03162-7.

Kim, K.-S., S.-Y. Park, S. Choi and H. Lee (2004), "Vapor Pressures of the 1-Butyl-3-Methylimidazolium Bromide + Water, 1-Butyl-3-Methylimidazolium Tetrafluoroborate + Water, and 1-(2-Hydroxyethyl)-3-Methylimidazolium Tetrafluoroborate + Water Systems," *Journal of Chemical & Engineering Data*. Vol. 49(6), pp. 1550-1553 DOI: 10.1021/je034210d.

Klein, S. A. (2015). *EES - Engineering Equation Solver*, Version 9.911. F-Chart Software, Middleton, WI.

Klein, S. A. (2018). *EES - Engineering Equation Solver*, Version 10.475. F-Chart Software, Middleton, WI.

Konikow, L. F. and E. Kendy (2005), "Groundwater Depletion: A Global Problem," *Hydrogeology Journal*. Vol. 13(1), pp. 317-320 DOI: 10.1007/s10040-004-0411-8.

Korkmaz, S. and İ. A. Kariper (2020), "Fog Harvesting against Water Shortage," *Environmental Chemistry Letters*. Vol. 18(2), pp. 361-375 DOI: 10.1007/s10311-019-00950-5.

Królikowska, M., M. Zawadzki and M. Królikowski (2014), "Physicochemical and Thermodynamic Study on Aqueous Solutions of Dicyanamide – Based Ionic Liquids," *The Journal of Chemical Thermodynamics*. Vol. 70, pp. 127-137 DOI: 10.1016/j.jct.2013.10.034.

Kumar, R. S., A. Mani and S. Kumaraswamy (2005), "Analysis of a Jet-Pump-Assisted Vacuum Desalination System Using Power Plant Waste Heat," *Desalination*. Vol. 179(1), pp. 345-354 DOI: 10.1016/j.desal.2004.11.081.

Kurt, C. and J. Bittner (2006). Sodium Hydroxide. *Ullmann's Encyclopedia of Industrial Chemistry*. W.-V. V. G. C. KGaA. Wiley-VCH Verlag GmbH & Co. KGaA, Weinheim, Germany p. a24_345.pub342.

Kusuda, T. and P. R. Achenbach (1965). "Earth Temperature and Thermal Diffusivity at Selected Stations in the United States," National Bureau of Standards, Gaithersburg, MD.

Kyung, I., K. E. Herold and Y. T. Kang (2007), "Experimental Verification of H_2O/LiBr Absorber Bundle Performance with Smooth Horizontal Tubes," *International Journal of Refrigeration*. Vol. 30(4), pp. 582-590 DOI: 10.1016/j.ijrefrig.2006.11.005.

Lachner, B. F., G. F. Nellis and D. T. Reindl (2007), "The Commercial Feasibility of the Use of Water Vapor as a Refrigerant," *International Journal of Refrigeration*. Vol. 30(4), pp. 699-708 DOI: 10.1016/j.ijrefrig.2006.09.009.

Lee, S., C. Boo, M. Elimelech and S. Hong (2010), "Comparison of Fouling Behavior in Forward Osmosis (FO) and Reverse Osmosis (RO)," *Journal of Membrane Science*. Vol. 365(1-2), pp. 34-39 DOI: 10.1016/j.memsci.2010.08.036.

Lin, S., N. Y. Yip and M. Elimelech (2014), "Direct Contact Membrane Distillation with Heat Recovery: Thermodynamic Insights from Module Scale Modeling," *Journal of Membrane Science*. Vol. 453, pp. 498-515 DOI: 10.1016/j.memsci.2013.11.016.

Liu, S., X. Mu, S. Shen, C. Li and B. Wang (2021), "Experimental Study on the Distribution of Local Heat Transfer Coefficient of Falling Film Heat Transfer Outside Horizontal Tube," *International Journal of Heat and Mass Transfer*. Vol. 170, p. 121031 DOI: 10.1016/j.ijheatmasstransfer.2021.121031.

Liu, S., S. Shen, X. Mu, Y. Guo and D. Yuan (2019), "Experimental Study on Droplet Flow of Falling Film between Horizontal Tubes," *International Journal of Multiphase Flow*. p. S0301932219301314 DOI: 10.1016/j.ijmultiphaseflow.2019.05.008.

Lorenz, J. J. and D. Yung (1982), "Film Breakdown and Bundle-Depth Effects in Horizontal-Tube, Falling-Film Evaporators," *Journal of Heat Transfer*. Vol. 104(3), pp. 569-571 DOI: 10.1115/1.3245135.

Malaeb, L. and G. M. Ayoub (2011), "Reverse Osmosis Technology for Water Treatment: State of the Art Review," *Desalination*. Vol. 267(1), pp. 1-8 DOI: 10.1016/j.desal.2010.09.001.

Mandani, F., H. Ettouney and H. El-Dessouky (2000), "LiBr-H_2O Absorption Heat Pump for Single-Effect Evaporation Desalination Process," *Desalination*. Vol. 128(2), pp. 161-176 DOI: 10.1016/S0011-9164(00)00031-X.

Marsters, G. F. (1972), "Arrays of Heated Horizontal Cylinders in Natural Convection," *International Journal of Heat and Mass Transfer*. Vol. 15(5), pp. 921-933 DOI: 10.1016/0017-9310(72)90231-1.

Mattingly, G. E. (1992), "The Characterization of a Piston Displacement-Type Flowmeter Calibration Facility and the Calibration and Use of Pulsed Output Type Flowmeters," *Journal of Research of the National Institute of Standards and Technology*. Vol. 97(5), p. 509 DOI: 10.6028/jres.097.023.

Maupin, M. A., J. F. Kenny, S. S. Hutson, J. K. Lovelace, N. L. Barber and K. S. Linsey (2014). "Estimated Use of Water in the United States in 2010," U.S. Geological Survey, Reston, VA, Circular, 1405.

McCleskey, R. B., D. K. Nordstrom, J. N. Ryan and J. W. Ball (2012), "A New Method of Calculating Electrical Conductivity with Applications to Natural Waters," *Geochimica et Cosmochimica Acta*. Vol. 77, pp. 369-382 DOI: 10.1016/j.gca.2011.10.031.

McCutcheon, J. R., R. L. McGinnis and M. Elimelech (2005), "A Novel Ammonia—Carbon Dioxide Forward (Direct) Osmosis Desalination Process," *Desalination*. Vol. 174(1), pp. 1-11 DOI: 10.1016/j.desal.2004.11.002.

McGovern, R. K. and J. H. Lienhard V (2014), "On the Potential of Forward Osmosis to Energetically Outperform Reverse Osmosis Desalination," *Journal of Membrane Science*. Vol. 469, pp. 245-250 DOI: 10.1016/j.memsci.2014.05.061.

Meacham, J. M. and S. Garimella (2004), "Ammonia-Water Absorption Heat and Mass Transfer in Microchannel Absorbers with Visual Confirmation," *ASHRAE Transactions*. Vol. 110(1).

Miller, W. A. (1998). *The Experimental Analysis of Aqueous Lithium Bromide Vertical Film Absorption*. PhD Thesis, University of Tennessee - Knoxville, Knoxville, TN.

Mitra, S., P. Kumar, K. Srinivasan and P. Dutta (2015), "Performance Evaluation of a Two-Stage Silica Gel + Water Adsorption Based Cooling-Cum-Desalination System," *International Journal of Refrigeration*. Vol. 58, pp. 186-198 DOI: 10.1016/j.ijrefrig.2015.06.018.

Mitra, S., P. Kumar, K. Srinivasan and P. Dutta (2016), "Development and Performance Studies of an Air Cooled Two-Stage Multi-Bed Silica Gel + Water Adsorption System," *International Journal of Refrigeration*. DOI: 10.1016/j.ijrefrig.2015.10.028.

Mitra, S., K. Srinivasan, P. Kumar, S. S. Murthy and P. Dutta (2014), "Solar Driven Adsorption Desalination System," *Energy Procedia*. Vol. 49, pp. 2261-2269 DOI: 10.1016/j.egypro.2014.03.239.

Mitrovic, J. (2005), "Flow Structures of a Liquid Film Falling on Horizontal Tubes," *Chemical Engineering & Technology*. Vol. 28(6), pp. 684-694 DOI: 10.1002/ceat.200500064.

Mohammadi, K. and J. G. McGowan (2018), "An Efficient Integrated Trigeneration System for the Production of Dual Temperature Cooling and Fresh Water: Thermoeconomic Analysis and Optimization," *Applied Thermal Engineering*. Vol. 145, pp. 652-666 DOI: 10.1016/j.applthermaleng.2018.09.059.

Nada, S. A., H. F. Elattar and A. Fouda (2015a), "Experimental Study for Hybrid Humidification–Dehumidification Water Desalination and Air Conditioning System," *Desalination*. Vol. 363, pp. 112-125 DOI: 10.1016/j.desal.2015.01.032.

Nada, S. A., H. F. Elattar and A. Fouda (2015b), "Performance Analysis of Proposed Hybrid Air Conditioning and Humidification–Dehumidification Systems for Energy Saving and Water Production in Hot and Dry Climatic Regions," *Energy Conversion and Management*. Vol. 96, pp. 208-227 DOI: 10.1016/j.enconman.2015.02.082.

Nagavarapu, A. K. and S. Garimella (2019a), "Experimentally Validated Models for Falling-Film Absorption around Microchannel Tube Banks: Heat and Mass Transfer," *International Journal of Heat and Mass Transfer*. Vol. 139, pp. 303-316 DOI: 10.1016/j.ijheatmasstransfer.2019.05.024.

Nagavarapu, A. K. and S. Garimella (2019b), "Experimentally Validated Models for Falling-Film Absorption around Microchannel Tube Banks: Hydrodynamics," *International Journal of Heat and Mass Transfer*. Vol. 134, pp. 815-827 DOI: 10.1016/j.ijheatmasstransfer.2018.12.127.

Narayan, G. P., M. H. Sharqawy, E. K. Summers, J. H. Lienhard, S. M. Zubair and M. A. Antar (2010), "The Potential of Solar-Driven Humidification–Dehumidification Desalination for Small-Scale Decentralized Water Production," *Renewable and Sustainable Energy Reviews*. Vol. 14(4), pp. 1187-1201 DOI: 10.1016/j.rser.2009.11.014.

Narváez-Romo, B., M. Chhay, E. W. Zavaleta-Aguilar and J. R. Simões-Moreira (2017), "A Critical Review of Heat and Mass Transfer Correlations for LiBr-H_2O and NH_3-H_2O Absorption Refrigeration Machines Using Falling Liquid Film Technology," *Applied Thermal Engineering*. Vol. 123, pp. 1079-1095 DOI: 10.1016/j.applthermaleng.2017.05.092.

Ng, K. C., K. Thu, A. Chakraborty, B. B. Saha and W. G. Chun (2009), "Solar-Assisted Dual-Effect Adsorption Cycle for the Production of Cooling Effect and Potable Water," *International Journal of Low-Carbon Technologies*. Vol. 4(2), pp. 61-67 DOI: 10.1093/ijlct/ctp008.

Ng, K. C., K. Thu, Y. Kim, A. Chakraborty and G. Amy (2013), "Adsorption Desalination: An Emerging Low-Cost Thermal Desalination Method," *Desalination*. Vol. 308, pp. 161-179 DOI: 10.1016/j.desal.2012.07.030.

Ng, K. C., K. Thu, B. B. Saha and A. Chakraborty (2012), "Study on a Waste Heat-Driven Adsorption Cooling Cum Desalination Cycle," *International Journal of Refrigeration*. Vol. 35(3), pp. 685-693 DOI: 10.1016/j.ijrefrig.2011.01.008.

Nicol, A. A., Z. L. Aidoun, R. J. Gribben and G. Wilks (1988), "Heat Transfer in the Presence of Condensate Drainage," *International Journal of Multiphase Flow*. Vol. 14(3), pp. 349-359 DOI: 10.1016/0301-9322(88)90049-3.

Nusselt, W. (1916), "The Surface Condensation of Water Vapour," *VDI Z*. Vol. 60, pp. 541-546.

Oki, T. and S. Kanae (2006), "Global Hydrological Cycles and World Water Resources," *Science*. Vol. 313(5790), pp. 1068-1072 DOI: 10.1126/science.1128845.

Oki, T. and R. E. Quiocho (2020), "Economically Challenged and Water Scarce: Identification of Global Populations Most Vulnerable to Water Crises," *International Journal of Water Resources Development*. Vol. 36(2-3), pp. 416-428 DOI: 10.1080/07900627.2019.1698413.

Olbricht, M. and A. Luke (2018), "Falling Film Evaporation of Aqueous Lithium Bromide Solution at Low Pressure," *Heat and Mass Transfer*. Vol. 54(8), pp. 2507-2520 DOI: 10.1007/s00231-018-2409-0.

Olbricht, M. and A. Luke (2019), "Experimental Investigation of the Heat and Mass Transfer in a Tube Bundle Absorber of an Absorption Chiller," *Heat and Mass Transfer*. Vol. 55(1), pp. 81-93 DOI: 10.1007/s00231-018-2363-x.

Palenzuela, P., A. S. Hassan, G. Zaragoza and D.-C. Alarcón-Padilla (2014), "Steady State Model for Multi-Effect Distillation Case Study: Plataforma Solar De Almería MED Pilot Plant," *Desalination*. Vol. 337, pp. 31-42 DOI: 10.1016/j.desal.2013.12.029.

Park, C. W., S. S. Kim, H. C. Cho and Y. T. Kang (2003), "Experimental Correlation of Falling Film Absorption Heat Transfer on Micro-Scale Hatched Tubes," *International Journal of Refrigeration*. Vol. 26(7), pp. 758-763 DOI: 10.1016/S0140-7007(03)00069-0.

Parken, W. H., L. S. Fletcher, V. Sernas and J. C. Han (1990), "Heat Transfer through Falling Film Evaporation and Boiling on Horizontal Tubes," *Journal of Heat Transfer*. Vol. 112(3), pp. 744-750 DOI: 10.1115/1.2910449.

Pérez Ballesta, P. (2005), "The Uncertainty of Averaging a Time Series of Measurements and Its Use in Environmental Legislation," *Atmospheric Environment*. Vol. 39(11), pp. 2003-2009 DOI: 10.1016/j.atmosenv.2004.12.009.

Pinheiro, J. M., A. A. Valente, S. Salústio, N. Ferreira, J. Rocha and C. M. Silva (2015), "Application of the Novel Ets-10/Water Pair in Cyclic Adsorption Heating Processes: Measurement of Equilibrium and Kinetics Properties and Simulation Studies," *Applied Thermal Engineering*. Vol. 87, pp. 412-423 DOI: 10.1016/j.applthermaleng.2015.05.011.

Potter, B. B. and J. Wimsatt (2009). "Method 415.3, Rev. 1.2: Determination of Total Organic Carbon and Specific Uv Absorbance at 254 Nm in Source Water and Drinking Water," U.S. Environmental Protection Agency, Washington, D.C., 415.3.

Prieto, F., E. Barrado, M. Vega and L. Deban (2001), "Measurement of Electrical Conductivity of Wastewater for Fast Determination of Metal Ion Concentration," *Russian Journal of Applied Chemistry*. Vol. 74(8), pp. 1321-1324 DOI: 10.1023/A:1013710413982.

Quijada-Maldonado, E., S. van der Boogaart, J. H. Lijbers, G. W. Meindersma and A. B. de Haan (2012), "Experimental Densities, Dynamic Viscosities and Surface

Tensions of the Ionic Liquids Series 1-Ethyl-3-Methylimidazolium Acetate and Dicyanamide and Their Binary and Ternary Mixtures with Water and Ethanol at T=(298.15 to 343.15k)," *The Journal of Chemical Thermodynamics*. Vol. 51, pp. 51-58 DOI: 10.1016/j.jct.2012.02.027.

Ratlamwala, T. A. H., I. Dincer and M. A. Gadalla (2013), "Energy and Exergy Analyses of an Integrated Solar-Based Desalination Quadruple Effect Absorption System for Freshwater and Cooling Production: Exergy Analysis of an Integrated Solar, Desalination-Absorption System," *International Journal of Energy Research*. Vol. 37(13), pp. 1569-1579 DOI: 10.1002/er.2961.

Rebelo, L. P. N., V. Najdanovic-Visak, Z. P. Visak, M. Nunes da Ponte, J. Szydlowski, C. A. Cerdeiriña, J. Troncoso, L. Romaní, J. M. S. S. Esperança, H. J. R. Guedes and H. C. de Sousa (2004), "A Detailed Thermodynamic Analysis of $[C_4mim][BF_4]$ + Water as a Case Study to Model Ionic Liquid Aqueous Solutions," *Green Chemistry*. Vol. 6(8), p. 369 DOI: 10.1039/b400374h.

Ren, J., Z. Zhao and X. Zhang (2011), "Vapor Pressures, Excess Enthalpies, and Specific Heat Capacities of the Binary Working Pairs Containing the Ionic Liquid 1-Ethyl-3-Methylimidazolium Dimethylphosphate," *The Journal of Chemical Thermodynamics*. Vol. 43(4), pp. 576-583 DOI: 10.1016/j.jct.2010.11.014.

Rezaei, M., D. M. Warsinger, J. H. Lienhard V, M. C. Duke, T. Matsuura and W. M. Samhaber (2018), "Wetting Phenomena in Membrane Distillation: Mechanisms, Reversal, and Prevention," *Water Research*. Vol. 139, pp. 329-352 DOI: 10.1016/j.watres.2018.03.058.

Ribatski, G. and A. M. Jacobi (2005), "Falling-Film Evaporation on Horizontal Tubes—a Critical Review," *International Journal of Refrigeration*. Vol. 28(5), pp. 635-653 DOI: 10.1016/j.ijrefrig.2004.12.002.

Ribatski, G. and J. R. Thome (2007), "Experimental Study on the Onset of Local Dryout in an Evaporating Falling Film on Horizontal Plain Tubes," *Experimental Thermal and Fluid Science*. Vol. 31(6), pp. 483-493 DOI: 10.1016/j.expthermflusci.2006.05.010.

Römich, C., N. C. Merkel, A. Valbonesi, K. Schaber, S. Sauer and T. J. S. Schubert (2012), "Thermodynamic Properties of Binary Mixtures of Water and Room-Temperature Ionic Liquids: Vapor Pressures, Heat Capacities, Densities, and Viscosities of Water + 1-Ethyl-3-Methylimidazolium Acetate and Water + Diethylmethylammonium Methane Sulfonate," *Journal of Chemical & Engineering Data*. Vol. 57(8), pp. 2258-2264 DOI: 10.1021/je300132e.

Roques, J.-F. and J. R. Thome (2007), "Falling Films on Arrays of Horizontal Tubes with R-134a, Part Ii: Flow Visualization, Onset of Dryout, and Heat Transfer

Predictions," *Heat Transfer Engineering*. Vol. 28(5), pp. 415-434 DOI: 10.1080/01457630601163736.

Ruiter, J. P. (1990), "Simplified Thermodynamic Description of Mixtures and Solutions," *International Journal of Refrigeration*. Vol. 13(4), pp. 223-236 DOI: 10.1016/0140-7007(90)90034-T.

Saha, B. B., I. I. El-Sharkawy, M. W. Shahzad, K. Thu, L. Ang and K. C. Ng (2016), "Fundamental and Application Aspects of Adsorption Cooling and Desalination," *Applied Thermal Engineering*. Vol. 97, pp. 68-76 DOI: 10.1016/j.applthermaleng.2015.09.113.

Sander, R. (2015), "Compilation of Henry's Law Constants (Version 4.0) for Water as Solvent," *Atmospheric Chemistry and Physics*. Vol. 15(8), pp. 4399-4981 DOI: 10.5194/acp-15-4399-2015.

Sanmamed, Y. A., P. Navia, D. González-Salgado, J. Troncoso and L. Romaní (2010), "Pressure and Temperature Dependence of Isobaric Heat Capacity for [Emim][BF_4], [Bmim][BF_4], [Hmim][BF_4], and [Omim][BF_4]," *Journal of Chemical & Engineering Data*. Vol. 55(2), pp. 600-604 DOI: 10.1021/je9004992.

Schütz, G. (1963), "Natural Convection Mass-Transfer Measurements on Spheres and Horizontal Cylinders by an Electrochemical Method," *International Journal of Heat and Mass Transfer*. Vol. 6(10), pp. 873-879 DOI: 10.1016/0017-9310(63)90078-4.

Seiler, M., C. Jork, A. Kavarnou, W. Arlt and R. Hirsch (2004), "Separation of Azeotropic Mixtures Using Hyperbranched Polymers or Ionic Liquids," *AIChE Journal*. Vol. 50(10), pp. 2439-2454 DOI: 10.1002/aic.10249.

Shahzad, M. W., K. C. Ng, K. Thu, B. B. Saha and W. G. Chun (2014), "Multi Effect Desalination and Adsorption Desalination (MEDAD): A Hybrid Desalination Method," *Applied Thermal Engineering*. Vol. 72(2), pp. 289-297 DOI: 10.1016/j.applthermaleng.2014.03.064.

Shurtz, R. (2018). "Total Hemispherical Emissivity of Metals Applicable to Radiant Heat Testing,"; Sandia National Lab. (SNL-NM), Albuquerque, NM (United States), SAND2018-13271; Other: 670259 United States 10.2172/1483461 Other: 670259 SNL English.

Sivakumar, V. and E. Ganapathy Sundaram (2013), "Improvement Techniques of Solar Still Efficiency: A Review," *Renewable and Sustainable Energy Reviews*. Vol. 28, pp. 246-264 DOI: 10.1016/j.rser.2013.07.037.

Srikhirin, P., S. Aphornratana and S. Chungpaibulpatana (2001), "A Review of Absorption Refrigeration Technologies," *Renewable and Sustainable Energy Reviews*. Vol. 5(4), pp. 343-372 DOI: 10.1016/S1364-0321(01)00003-X.

Steiner, D. and J. Taborek (1992), "Flow Boiling Heat Transfer in Vertical Tubes Correlated by an Asymptotic Model," *Heat Transfer Engineering*. Vol. 13(2), pp. 43-69 DOI: 10.1080/01457639208939774.

Su, B., W. Han and H. Jin (2017), "An Innovative Solar-Powered Absorption Refrigeration System Combined with Liquid Desiccant Dehumidification for Cooling and Water," *Energy Conversion and Management*. Vol. 153, pp. 515-525 DOI: 10.1016/j.enconman.2017.10.028.

Subramaniam, V. and S. Garimella (2014), "Numerical Study of Heat and Mass Transfer in Lithium Bromide-Water Falling Films and Droplets," *International Journal of Refrigeration*. Vol. 40, pp. 211-226 DOI: 10.1016/j.ijrefrig.2013.07.025.

Thomas, A., J. J. Lorenz, D. L. Hillis, D. T. Yung and N. P. Sather (1979), "Performance Tests of the 1mwt Shell-and-Tube Heat Exchangers for OTEC," *Proceedings of 6th Ocean Thermal Energy Conversion Conference*, pp. 1-10.

Thome, J. R. (1999), "Falling Film Evaporation: State-of-the-Art Review of Recent Work," *Journal of Enhanced Heat Transfer*. Vol. 6(2-4), pp. 263-277 DOI: 10.1615/JEnhHeatTransf.v6.i2-4.140.

Thu, K., B. B. Saha, K. J. Chua and K. C. Ng (2016), "Performance Investigation of a Waste Heat-Driven 3-Bed 2-Evaporator Adsorption Cycle for Cooling and Desalination," *International Journal of Heat and Mass Transfer*. Vol. 101, pp. 1111-1122 DOI: 10.1016/j.ijheatmasstransfer.2016.05.127.

Thu, K., B. B. Saha, S. Mitra and K. J. Chua (2017), "Modeling and Simulation of Mass Recovery Process in Adsorption System for Cooling and Desalination," *Energy Procedia*. Vol. 105, pp. 2004-2009 DOI: 10.1016/j.egypro.2017.03.574.

Tu, Y., R. Wang, Y. Zhang and J. Wang (2018), "Progress and Expectation of Atmospheric Water Harvesting," *Joule*. Vol. 2(8), pp. 1452-1475 DOI: 10.1016/j.joule.2018.07.015.

Ueda, T., M. Inoue and S. Nagatome (1981), "Critical Heat Flux and Droplet Entrainment Rate in Boiling of Falling Liquid Films," *International Journal of Heat and Mass Transfer*. Vol. 24(7), pp. 1257-1266 DOI: 10.1016/0017-9310(81)90175-7.

Wade, N. U., R. Heaton and D. G. Boulter (1985), "Desalination and Water Reuse Comparison of MSF and RO in Dual Purpose Power and Water Plants," *Desalination*. Vol. 55, pp. 373-386 DOI: 10.1016/0011-9164(85)80085-0.

Wang, X. and A. M. Jacobi (2014), "A Thermodynamic Basis for Predicting Falling-Film Mode Transitions," *International Journal of Refrigeration*. Vol. 43, pp. 123-132 DOI: 10.1016/j.ijrefrig.2014.04.002.

Wang, X. and K. C. Ng (2005), "Experimental Investigation of an Adsorption Desalination Plant Using Low-Temperature Waste Heat," *Applied Thermal Engineering*. Vol. 25(17-18), pp. 2780-2789 DOI: 10.1016/j.applthermaleng.2005.02.011.

Wang, Y. and N. Lior (2008), "Combined Desalination and Refrigeration Systems Driven by Low-Grade Heat," *Proceedings of IMECE*, pp. 163-173.

Wang, Y. and N. Lior (2011a), "Proposal and Analysis of a High-Efficiency Combined Desalination and Refrigeration System Based on the LiBr–H_2O Absorption Cycle—Part 1: System Configuration and Mathematical Model," *Energy Conversion and Management*. Vol. 52(1), pp. 220-227 DOI: 10.1016/j.enconman.2010.06.071.

Wang, Y. and N. Lior (2011b), "Proposal and Analysis of a High-Efficiency Combined Desalination and Refrigeration System Based on the LiBr–H2O Absorption Cycle—Part 2: Thermal Performance Analysis and Discussions," *Energy Conversion and Management*. Vol. 52(1), pp. 228-235 DOI: 10.1016/j.enconman.2010.06.064.

Xie, Z., D. Ng, M. Hoang, J. Zhang and S. Gray (2018), "Study of Hybrid PVA/MA/TEOS Pervaporation Membrane and Evaluation of Energy Requirement for Desalination by Pervaporation," *International Journal of Environmental Research and Public Health*. Vol. 15(9), p. 1913 DOI: 10.3390/ijerph15091913.

Xiong, R. H., S. C. Wang, L. X. Xie, Z. Wang and P. L. Li (2005), "Experimental Investigation of a Baffled Shell and Tube Desalination Column Using the Humidification-Dehumidification Process," *Desalination*. Vol. 180(1-3), pp. 253-261 DOI: 10.1016/j.desal.2005.01.007.

Yao, W., H. Bjurstroem and F. Setterwall (1991), "Surface Tension of Lithium Bromide Solutions with Heat-Transfer Additives," *Journal of Chemical & Engineering Data*. Vol. 36(1), pp. 96-98 DOI: 10.1021/je00001a029.

Yih, S.-M. and K.-Y. Chen (1982), "Gas Absorption into Wavy and Turbulent Falling Liquid Films in a Wetted-Wall Column," *Chemical Engineering Communications*. Vol. 17(1-6), pp. 123-136 DOI: 10.1080/00986448208911620.

Yokozeki, A. and M. B. Shiflett (2010), "Water Solubility in Ionic Liquids and Application to Absorption Cycles," *Industrial & Engineering Chemistry Research*. Vol. 49(19), pp. 9496-9503 DOI: 10.1021/ie1011432.

Youssef, P. G., R. K. Al-Dadah, S. M. Mahmoud, H. J. Dakkama and A. Elsayed (2015a), "Effect of Evaporator and Condenser Temperatures on the Performance of Adsorption Desalination Cooling Cycle," *Energy Procedia*. Vol. 75, pp. 1464-1469 DOI: 10.1016/j.egypro.2015.07.263.

Youssef, P. G., S. M. Mahmoud and R. K. Al-Dadah (2015b), "Performance Analysis of Four Bed Adsorption Water Desalination/Refrigeration System, Comparison of Aqsoa-Z02 to Silica-Gel," *Desalination*. Vol. 375, pp. 100-107 DOI: 10.1016/j.desal.2015.08.002.

Youssef, P. G., S. M. Mahmoud and R. K. AL-Dadah (2016), "Numerical Simulation of Combined Adsorption Desalination and Cooling Cycles with Integrated Evaporator/Condenser," *Desalination*. Vol. 392, pp. 14-24 DOI: 10.1016/j.desal.2016.04.011.

Yuan, G., L. Zhang and H. Zhang (2005), "Experimental Research of an Integrative Unit for Air-Conditioning and Desalination," *Desalination*. Vol. 182(1-3), pp. 511-516 DOI: 10.1016/j.desal.2005.02.040.

Yuan, Z. and K. E. Herold (2005), "Thermodynamic Properties of Aqueous Lithium Bromide Using a Multiproperty Free Energy Correlation," *HVAC&R Research*. Vol. 11(3), pp. 377-393 DOI: 10.1080/10789669.2005.10391144.

Yung, D., J. J. Lorenz and E. N. Ganić (1980), "Vapor/Liquid Interaction and Entrainment in Falling Film Evaporators," *Journal of Heat Transfer*. Vol. 102(1), p. 20 DOI: 10.1115/1.3244242.

Zhang, S., X. Li, H. Chen, J. Wang, J. Zhang and M. Zhang (2004), "Determination of Physical Properties for the Binary System of 1-Ethyl-3-Methylimidazolium Tetrafluoroborate + H_2O," *Journal of Chemical & Engineering Data*. Vol. 49(4), pp. 760-764 DOI: 10.1021/je030191w.

Zhao, J., X.-C. Jiang, C.-X. Li and Z.-H. Wang (2006), "Vapor Pressure Measurement for Binary and Ternary Systems Containing a Phosphoric Ionic Liquid," *Fluid Phase Equilibria*. Vol. 247(1-2), pp. 190-198 DOI: 10.1016/j.fluid.2006.07.007.

Zhao, S., L. Zou, C. Y. Tang and D. Mulcahy (2012), "Recent Developments in Forward Osmosis: Opportunities and Challenges," *Journal of Membrane Science*. Vol. 396, pp. 1-21 DOI: 10.1016/j.memsci.2011.12.023.

Zheng, Y., X. Ma, Y. Li, R. Jiang, K. Wang, Z. Lan and Q. Liang (2017), "Experimental Study of Falling Film Evaporation Heat Transfer on Superhydrophilic Horizontal-Tubes at Low Spray Density," *Applied Thermal Engineering*. Vol. 111, pp. 1548-1556 DOI: 10.1016/j.applthermaleng.2016.07.177.

Zhong, Y., X. Feng, W. Chen, X. Wang, K.-W. Huang, Y. Gnanou and Z. Lai (2016), "Using Ucst Ionic Liquid as a Draw Solute in Forward Osmosis to Treat High-Salinity Water," *Environmental Science & Technology*. Vol. 50(2), pp. 1039-1045 DOI: 10.1021/acs.est.5b03747.

Zhou, Q., L.-S. Wang and H.-P. Chen (2006), "Densities and Viscosities of 1-Butyl-3-Methylimidazolium Tetrafluoroborate + H_2O Binary Mixtures from (303.15 to 353.15) K," *Journal of Chemical & Engineering Data*. Vol. 51(3), pp. 905-908 DOI: 10.1021/je050387r.